

Towards improved property prediction of two-dimensional (2D) materials using many-body Quantum Monte Carlo methods

Daniel Wines,^{1, a)} Jeonghwan Ahn,² Anouar Benali,³ Paul R. C. Kent,⁴ Jaron T. Krogel,² Yongkyung Kwon,⁵ Lubos Mitas,⁶ Fernando A. Reboredo,² Brenda Rubenstein,^{7, 8} Kayahan Saritas,² Hyeondeok Shin,³ Ivan Štich,⁹ and Can Ataca^{10, b)}

¹⁾*Materials Science and Engineering Division, National Institute of Standards and Technology (NIST), Gaithersburg, MD 20899*

²⁾*Material Science and Technology Division, Oak Ridge National Laboratory, Oak Ridge, TN 37831*

³⁾*Computational Science Division, Argonne National Laboratory, Argonne, IL 60439, USA*

⁴⁾*Computational Sciences and Engineering Division, Oak Ridge National Laboratory, Oak Ridge, TN 37831, USA*

⁵⁾*Department of Physics, Konkuk University, Seoul 05029, Korea*

⁶⁾*Department of Physics, North Carolina State University, Raleigh, NC 27695-8202, USA*

⁷⁾*Department of Chemistry, Brown University, Providence, RI 02912, USA*

⁸⁾*Department of Physics, Brown University, Providence, RI 02912, USA*

⁹⁾*Institute of Informatics, Slovak Academy of Sciences, 845 07 Bratislava, Slovakia*

¹⁰⁾*Department of Physics, University of Maryland Baltimore County, Baltimore MD 21250*

(Dated: 6 June 2024)

The field of two-dimensional (2D) materials has grown dramatically in the last two decades. 2D materials can be utilized for a variety of next-generation optoelectronic, spintronic, clean energy, and quantum computation applications. These 2D structures, which are often exfoliated from layered van der Waals (vdW) materials, possess highly inhomogeneous electron densities and can possess short- and long-range electron correlations. The complexities of 2D materials make them challenging to study with standard mean-field electronic structure methods such as density functional theory (DFT), which relies on approximations for the unknown exchange-correlation functional. In order to overcome the limitations of DFT, highly accurate many-body electronic structure approaches such as Diffusion Monte Carlo (DMC) can be utilized. In the past decade, DMC has been used to calculate accurate magnetic, electronic, excitonic, and topological properties in addition to accurately capturing interlayer interactions and cohesion and adsorption energetics of 2D materials. This approach has been applied to 2D systems of wide interest including graphene, phosphorene, MoS₂, CrI₃, VSe₂, GaSe, GeSe, borophene, and several others. In this review article, we highlight some successful recent applications of DMC to 2D systems for improved property predictions beyond standard DFT.

I. INTRODUCTION

Since the synthesis of graphene in 2004 by Geim and Novoselov that led to the 2010 Nobel Prize¹⁻³, there has been an overwhelming interest in the field of two-dimensional (2D) materials. 2D materials are single-layer crystalline structures that have a large lateral dimension compared to their thickness. Oftentimes, these monolayers are exfoliated from layered materials that are held together by weak van der Waals (vdW) bonds. Due to their lack

of surface groups or dangling bonds and large surface-to-volume ratio, 2D materials can possess interesting properties that are substantially different from those of their bulk counterparts¹⁻⁸. In addition, 2D materials can possess enhanced quantum confinement and significantly reduced dielectric screening⁷⁻⁹. These materials also present interesting phenomena such as enhanced carrier mobility¹⁻³, reduction of charge carrier scattering^{1-6,9}, superior mechanical properties¹⁰, direct-to-indirect band gap transitions⁴, non-trivial topological states¹¹⁻¹³, and superconductivity^{14,15} and magnetism in 2D¹⁶. These physical phenomena can be exploited for future applications in optoelectronics, spintronics, quantum computing, and clean energy^{17,18}.

In addition to graphene, there exist several other synthesized mono-elemental 2D materials such as germanene^{19,20}, borophene²¹⁻²⁴, silicene^{25,26}, antimonene²⁷⁻²⁹, phosphorene³⁰⁻³², and tellurene^{33,34}. A popular class of 2D materials for optoelectronic and magnetic applications are transition metal dichalcogenides (TMDs)^{4-6,35} such as monolayer MoS₂⁴⁻⁶, MoSe₂^{36,37}, WSe₂³⁷⁻³⁹ and WTe₂^{13,40}. Similarly to TMDs, there exist post-transition metal chalcogenides (PTMCs)^{41,42} such as 2D GaSe^{41,43-50}, GeSe^{51,52}

¹ Notice: This manuscript has been authored by UT-Battelle, LLC, under contract DE-AC05-00OR22725 with the US Department of Energy (DOE). The US government retains and the publisher, by accepting the article for publication, acknowledges that the US government retains a nonexclusive, paid-up, irrevocable, worldwide license to publish or reproduce the published form of this manuscript, or allow others to do so, for US government purposes. DOE will provide public access to these results of federally sponsored research in accordance with the DOE Public Access Plan (<https://www.energy.gov/doe-public-access-plan>).

^{a)}Electronic mail: daniel.wines@nist.gov

^{b)}Electronic mail: ataca@umbc.edu

and InSe^{53,54} that have also shown promise for optoelectronic applications. Another class of 2D materials with applications in energy storage are MXenes^{55–57}, which are monolayer structures of transition metal carbides, nitrides, or carbonitrides. Monolayer halide-based materials such as CrI₃¹⁶, CrBr₃⁵⁸, and NiI₂⁵⁹ have also been synthesized as 2D magnets and RuCl₃ has been shown to have topological properties¹¹.

The electronic density in 2D materials is highly inhomogeneous. 2D materials may possess a combination of short-range, strong correlations (if d orbitals are involved) with long-range, weak correlations. These complicated electronic properties of 2D materials make them difficult to model using methods such as Density Functional Theory (DFT)^{60,61}. DFT calculations are, in principle, exact, but rely on approximations for the unknown exchange-correlation (XC) functional that models the many-body quantum interactions^{60,61}. Although modern approximations for density functionals have advanced throughout the last few decades, progressing from local (local density approximation, LDA^{62,63}), to semilocal (generalized gradient approximation, GGA^{64,65} and meta-GGA^{66–70}), to hybrid functionals (i.e., HSE, PBE0 and B3LYP^{71–77}), certain shortcomings remain. The most obvious limitation of DFT is that its results can strongly depend on the XC functional and there is no *a priori* way to know the significance of the approximations in the chosen functional. In addition, many DFT functionals require explicit corrections to handle vdW interactions^{78–85}. vdW interactions are crucial for low-dimensional layered materials, whose properties are significantly impacted by which vdW correction or functional is used in DFT^{86,87}.

Modeling strongly correlated electronic systems poses a challenge within DFT frameworks due to the tendency of standard exchange-correlation functionals (like LDA and GGA) to overly delocalize valence electrons⁸⁸. This issue predominantly stems from the self-interaction error,⁶² rendering DFT inadequate for accurately describing strongly localized systems, such as those found in transition metal-based materials containing d and f electrons. To correct this delocalization error, the Hubbard (U) correction⁸⁹, which is an additional onsite Coulomb interaction, can be applied to correlated electronic states. Although self-consistent approaches for obtaining U have been developed^{90,91}, the choice of U value can be arbitrary and is often either fit to experiments or selected from previous literature values⁹². The vast majority of interesting 2D materials are electronic, magnetic, and topological materials that contain transition metals with correlated d and f electrons and DFT+U has been previously applied to handle such correlations^{93,94}. Hybrid/exact-exchange functionals and some meta-GGAs also reduce the degree of self-interaction error, but a consistent high-accuracy treatment remains elusive. The problem of self-interaction error was the main topic of the original LDA DFT paper⁶², and it is interesting to note that the problem persists more than 40 years later.

Another major shortcoming of DFT is its underestimation of the band gap for semiconductors and insulators, which results in significant disagreements with experiments. This underestimation is clearly apparent for local and semilocal

functionals such as LDA and GGA, with noted improvements for meta-GGA functionals^{95–97}. Significant improvements to the accuracy of DFT electronic structure predictions can be achieved through the use of hybrid functionals, but there are fundamental theoretical issues that can limit DFT's accuracy^{95–97}. DFT is a ground state theory that maps the electronic structure problem to a fictitious Kohn-Sham system of single electrons occupying energy bands. Therefore, the band gap computed with DFT can be understood as the Kohn-Sham energy gap. For an infinite solid calculated with the exact DFT functional, the DFT gap would be the exact quasiparticle gap⁹⁸. In real materials, electrons feel the effects of surrounding electrons and holes, a phenomenon that is not captured at the quasiparticle level. In order to accurately predict optical excitations (the promotion gap, excitonic effects), these quasi-electron and quasi-hole interactions must be taken into account⁹⁹. These interactions can be obtained using post-DFT methods such as many-body perturbation theory (i.e., the GW approximation)^{99–101} and the Bethe-Salpeter equation (BSE)^{99,102} for electron-hole interactions or by exciting the system within a many-body stochastic theory such as Diffusion Monte Carlo (DMC)¹⁰³. The quasiparticle picture and excitonic effects are extremely important for understanding 2D materials^{7,9}. The reduced dielectric screening in low-dimensional systems can result in strong excitonic effects (exciton binding energies in the 10 - 100 meV range)^{7–9}.

In addition to reduced screening, spin-orbit coupling (SOC) can play an important role in understanding the electronic structure of 2D materials^{12,104–107}. Several TMDs have SOC-induced band splitting in the valence and conduction bands, which can be exploited for spintronic and valleytronic applications. In addition, SOC can induce band inversions and other topological properties in 2D materials^{12,104–107}. Modeling spin-orbit in 2D materials can be challenging with standard DFT methods. There have been several computational studies that have shown the considerable impact of SOC on the electronic structure and have demonstrated that results can significantly vary depending on the choice of methodology^{12,108–113}.

2D materials are promising and complicated structures that have significant vdW interactions, correlated electronic and magnetic properties, and unique excitonic and topological properties that make them the perfect test bed for more accurate computational methodologies. The strong dependence of the results on the density functional and Hubbard correction can severely limit the reliability of DFT for these 2D systems. In addition, methods that can correct bands gaps and other DFT predictions such as GW and BSE still significantly rely on the Kohn-Sham eigenvalues obtained from a particular DFT functional. For this reason, Diffusion Monte Carlo (DMC)¹⁰³ is an ideal method to accurately describe the properties of 2D materials. Although DMC is orders of magnitude more computationally intensive than DFT, it is extremely scalable on modern computers and scales as N^{3-4} , where N is the number of electrons in the simulation¹⁰³. In addition, the stochastic many-body nature of DMC and its controllable approximations allow for results that have a much weaker dependence on the starting wavefunction and density functional¹⁰³.

In this review article, we will give an overview of how the

DMC method has recently been applied to a variety of low-dimensional systems. Section II will give a brief overview of the theory, Section III A will give a description of how DMC has been applied to correlated 2D magnetic systems, Section III B will detail how DMC has been used for improved predictions of electronic properties (including excitonic, spin-orbit, and topological effects), Section III C will focus on how DMC has been used to improve the prediction of interlayer interactions, Section III D will describe how DMC has been used for the cohesion and adsorption energetics of low-dimensional materials, and Section IV will give concluding remarks and offer future perspectives.

II. THEORY

In this review article, we survey the application of the DMC¹⁰³ method, a real-space quantum Monte Carlo (QMC) method, to low-dimensional systems. Although the exact specifications of the calculations may vary among the works presented in this manuscript, we will provide a broad overview of the theory and approximations used throughout these calculations.

DMC is a projector-based method that can be used to obtain the ground state energy of a many-body system. In this method, the time-dependent Schrödinger equation is recast into the imaginary-time (τ) Schrödinger equation:

$$-\frac{\partial_{\tau}\Psi(\mathbf{R},\tau)}{\partial\tau}=(\hat{H}-E)\Psi(\mathbf{R},\tau), \quad (1)$$

where \hat{H} is the Hamiltonian operator which consists of kinetic and potential energy contributions, τ measures the progress in imaginary time, $\Psi(\mathbf{R},\tau)$ is the wavefunction at imaginary time τ , and E is the offset of the ground state energy. As $\tau \rightarrow \infty$, the weight of the DMC configurations with higher energy are damped exponentially. Therefore, the ground state wavefunction is projected out once a steady state has been reached.

The fluctuations in the reweighing process have been shown to be reduced significantly by using a trial (guiding) wavefunction ($\Psi_T(\mathbf{R})$) which transforms the wavefunction in Equation 1 into $f(\mathbf{R},t)=\Psi_T(\mathbf{R})\Psi(\mathbf{R},\tau)$. The quality of the trial wavefunction can be improved by a set of Jastrow factors¹¹⁴:

$$\Psi_T(\mathbf{R})=e^{J(\mathbf{R})}D^{\uparrow}(\mathbf{R})D^{\downarrow}(\mathbf{R}), \quad (2)$$

where $J(\mathbf{R})$ represents the Jastrow factors and D^{\uparrow} and D^{\downarrow} represent Slater determinants of up and down spins. The Slater determinant in the trial wavefunction usually comes from a DFT or Hartree Fock (HF) calculation. More general representations constructed from multi-determinant expansions are also possible. In fact, the application of millions of determinants to solids is now possible.^{115,116} The Jastrow factor explicitly includes electron correlations such as parameterized electron-ion, electron-electron, and electron-electron-ion terms. These terms are found through optimization of the wavefunction and the ground state energy and/or

variance^{117,118}. The increased accuracy of the trial wavefunctions – being closer to an exact eigenstate – also serves to reduce the number of statistical samples needed to reach a specific error bar, usually reducing computational costs.

DMC formally treats the many-body electron-electron interaction exactly, however it utilizes several approximations to reduce the cost of performing the calculations in the presence of core electrons and the fermion sign problem. Fixed-node DMC produces the ground state energy with the constraint $\Psi_T(\mathbf{R})=0 \implies \Psi_0(\mathbf{R})=0$, such that the DMC wavefunction shares the same nodes or phase as the trial wavefunction^{63,103,119,120}. This fixed-node approximation is enforced to maintain the antisymmetry of the wavefunction. Given the exact nodal surface of a system from an exact trial wavefunction, the fixed-node DMC method will yield the exact energy. For approximate nodal surfaces, the error introduced is variational (positive) in the energy. Fortunately for approximate trial wavefunctions, this error is typically small, and because the error is variational, different choices of input wavefunction can be tested and the most accurate selected. Practical methods to minimize or test the fixed-node error involve changing the trial wavefunction by adjusting the Hubbard parameter in DFT+U or tuning the amount of exact exchange in hybrid DFT and finding the minimum DMC energy variationally^{121–125}. In addition, there exist more sophisticated techniques to improve the accuracy of the trial wavefunction, such as using multideterminants^{115,116,126} or backflow transformations¹²⁷. In principle, the accuracy can be systematically improved by using these forms, as well as by optimizing the orbitals entirely within the QMC calculation. This has yet to be done systematically in 2D materials, but several applications in bulk exist^{128,129} and indicate that the approach should be practical.

Another essential aspect of DMC calculations are pseudopotentials. Pseudopotentials are required in DMC to avoid the large cost of performing all-electron calculations. High-quality pseudopotentials are essential for ensuring the accuracy of DMC simulations while simultaneously removing chemically inert core electrons. Luckily, in the past decade, there has been a strong effort to develop DMC-specific norm-conserving pseudopotentials with suitable accuracy^{130–139}. Although the original method for evaluating pseudopotentials in DMC, the locality approximation¹⁴⁰, was non-variational, newer methods such as the T-moves approach¹⁴¹ restore the variational properties of the overall method.

Although various real-space DMC codes have been developed over the last few decades and applied to 2D materials (e.g., CASINO¹⁴², PyQMC¹⁴³, QWalk¹⁴⁴), most of the work in this review article utilizes the QMCPACK code^{145,146}. The QMCPACK code has been routinely updated and maintained to track the latest algorithmic and hardware developments and utilize computational resources more efficiently (<https://github.com/QMCPACK/qmcpack>). The QMCPACK code is equipped with the Nexus¹⁴⁷ workflow automation software, which helps create and monitor DFT/DMC workflows that cansignificantly reduce the user time by tracking computational dependencies. More detailed information about these theoretical frameworks and codes can be found in

Refs. 63, 103, 119, 120, 142–146, and 148. For this review article, it is important to note that the error bars in each figure and the uncertainty noted in \pm in concise notation (*i.e.*, 5.3 ± 0.1 can be expressed as $5.3(1)$) refer to the standard error about the mean for each observable quantity calculated with QMC (*i.e.*, energy, band gap, magnetic moment, lattice constant).

III. DMC PROPERTIES OF 2D MATERIALS

A. Magnetic Properties

After the experimental synthesis of monolayer CrI_3 , which was measured to have a Curie temperature (T_c) of 45 K¹⁶, significant interest in identifying and physically understanding similar magnetic 2D materials has increased. It has been experimentally reported that monolayer VSe_2 is ferromagnetic on a vdW substrate¹⁴⁹ and that ferromagnetic order exists in the bilayer limit for $\text{Cr}_2\text{Ge}_2\text{Te}_6$ ¹⁵⁰. Some other examples of low-dimensional magnetic systems include FePS_3 ¹⁵¹, NiPS_3 ¹⁵², MnPS_3 ¹⁵³, and Fe_3GeTe_2 ¹⁵⁴. Several computational works have also predicted magnetism in a variety of 2D systems^{155–158}.

The Mermin-Wagner theorem¹⁵⁹ states that magnetic order in a 2D material cannot persist unless magnetic anisotropy (MA) is present. Moreover, it requires anisotropy that breaks continuous symmetries. Whether the anisotropy is perpendicular to the plane (easy-axis) or parallel to the plane (easy plane) determines the type of transition temperature. For easy-axis anisotropy, the system can be described by the Heisenberg model with a finite Curie temperature T_c . For easy-plane anisotropy, there is no explicit transition between the ordered and unordered states, but instead a Kosterlitz-Thouless transition at finite temperature T_{KT} , where the system has quasi-long-range magnetic order below T_{KT} . To obtain accurate estimates for observables such as T_c and T_{KT} , an accurate computation of the magnetic exchange and magnetic anisotropy energies is essential. Oftentimes, these results are extremely sensitive to the choice of density functional and Hubbard U parameter, resulting in inconclusive results with DFT. Additionally, these 2D magnetic materials can have a strong interdependence between structural parameters and magnetic properties, making it even more difficult to make accurate predictions. Due to this, using a method such as DMC to understand the electron correlation effects that drive magnetic ordering in 2D is necessary. These accurately computed ab initio magnetic parameters can then be used in conjunction with either classical Monte Carlo methods or other analytical models¹⁶⁰ to estimate observable quantities such as transition temperatures. Next, we will discuss few of our works on modeling magnetic 2D structures.

1. Monolayer CrI_3

One of the first monolayer magnets discovered,¹⁶ monolayer CrI_3 is a Mott insulator¹⁶¹ that consists of chromium

atoms octahedrally coordinated by six iodine atoms (see Figures 1 and 2). Because of the negative exchange interactions among them, the spins on the Cr atoms arrange themselves perpendicular to the plane of the material,^{162,163} resulting in a monolayer ferromagnet with a critical temperature of 45 K.^{16,164} Upon stacking, CrI_3 heterostructures oscillate between exhibiting ferromagnetism for odd numbers of layers and antiferromagnetism for even numbers of layers.¹⁶⁵ Moreover, upon the application of pressure that decreases the inter-layer distance, bilayer CrI_3 transitions from an antiferromagnet to a ferromagnet.^{166,167}

These phenomena suggest that electron-electron and electron-phonon interactions play a key role in determining CrI_3 's magnetic and structural properties. Yet, while significant research has gone into characterizing and modifying the macroscopic properties of this material, far less research has focused on the atomistic determinants of those properties in a manner that accurately accounts for many-body interactions. As a result, only approximate explanations for the source of this material's magnetism had been put forth before the DMC research described below was conducted. In particular, based on a rudimentary analysis of oxidation states, it was originally believed that each iodine atom in CrI_3 would have an oxidation state of -1 and therefore that the chromium should have an oxidation state of +3. Given that neutral Cr has a $[\text{Ar}]4s^13d^5$ electron configuration, this suggests that Cr^{3+} should have three valence electrons remaining, giving rise to a magnetic moment of $3 \mu_B$. More accurate, yet still single reference DFT calculations corroborated this picture – on average – but often differed significantly from one another in detail.^{162,168–171} Previous PBE+U ($U = 2$ eV) and HSE calculations, for example, predicted Cr's magnetic moment to be as large as $3.3 \mu_B$,^{169,171} while PBE¹⁷¹ and LDA+U¹⁶² calculations predicted moments as small as $3.1 \mu_B$ and $3 \mu_B$, respectively – a 10 % difference among moments overall. Even larger differences could be observed among DFT predictions of the in-plane lattice parameter: PBE calculations predicted a CrI_3 lattice parameter of 7.008 \AA ,¹⁷¹ while LDA+U calculations predicted a lattice parameter of 6.686 \AA ,¹⁶² a 5 % difference. These significant DFT discrepancies were further corroborated by our own DFT calculations, which not only demonstrated that the magnetic moments and lattice parameters predicted monotonically increased with the U employed in PBE+U calculations (suggesting that it would be difficult to determine a meaningful U value from DFT calculations alone), but also that the U that most closely matched experiments for one property significantly differed from those needed to match experimental predictions of other properties.¹⁰⁹ Thus, while these predictions provide general insights into CrI_3 's magnetism, they lack the accuracy – and precision – needed to make definitive statements.

To bring clarity to this picture, we thus performed DMC simulations on monolayer CrI_3 , one of the first performed on a magnetic monolayer material.¹⁰⁹ Given the known sensitivity of the electronic structure of 2D materials to strain^{172,173} and the lack of experimental results for the monolayer geometry, however, we first set out to determine a high-accuracy, *many-body* monolayer geometry (see Fig. 1). To do so, we leveraged

a cutting-edge, many-body geometry optimization method termed the surrogate Hessian line-search method.^{174–176} In this approach, a Hessian generated using DFT is used to determine conjugate directions along which to locate the minimum-energy structure. Differing from standard DFT-based conjugate gradient minimization, the surrogate Hessian line-search method then computes DMC energies in parallel along each of the conjugate directions and subsequently refines the conjugate directions until the search converges to the DMC energy minimum.^{174–176} This method is particularly advantageous because it makes the most efficient use of both DFT and DMC data: instead of relying on more expensive DMC energy gradients, it uses relatively cheap DFT gradients and then employs DMC energy calculations to refine the search, thus providing a substantially more efficient way of determining fully many-body geometries. Applying this approach to CrI₃, we obtained a ground state geometry with a lattice parameter of $a_0 = 6.87 \text{ \AA}$ and a Cr-I bond distance of $d_{\text{Cr-I}} = 2.73 \text{ \AA}$.¹⁰⁹ Interestingly, while we were conducting this research, some of the first STM-based measurements of the monolayer geometry were performed yielding a lattice constant of $a_0 = 6.84 \text{ \AA}$.¹⁶⁸ Such strong agreement ($\leq 0.5 \%$ error) highlights the accuracy of our structure and the value of the surrogate Hessian line-search approach, despite CrI₃'s (and many monolayer materials') shallow potential energy surface around its minimum.

With this high-accuracy structure in hand, we then performed DMC calculations on the monolayer. To generate a high-quality trial wavefunction from which to construct our DMC nodal surface, we first performed PBE+U calculations. Unlike previous works, we were sure to determine our U in a variational fashion, by determining the U in our PBE+U trial wavefunctions that minimized our resultant DMC energies (see Fig. 1). This resulted in an optimized U value of 2 eV.¹⁰⁹ Employing this U in our Slater-Jastrow trial wavefunctions with one- and two-body Jastrow terms, we obtained high-accuracy DMC charge and spin densities. We finally obtained DMC estimates of the Cr magnetic moment by integrating the spin density from the center of the Cr atom to the distance from the nucleus at which the spin density changed sign (the zero-recrossing radius of the sign of the spin density). This yielded a DMC magnetic moment of $3.62 \mu_B$, a moment substantially larger than that previously predicted using single reference techniques. Importantly, PBE+U=2 eV calculations performed on the same optimized geometries yielded a similarly large Cr moment of $3.57 \mu_B$, demonstrating the strong coupling between the moment and the geometry,^{172,173} as also observed in previous DFT simulations and our subsequent spin-phonon and spin-lattice coupling calculations.¹⁰⁹ Although these moments seem unexpectedly large, they are counterbalanced by negative moments of $-0.145 \mu_B$ on the iodine atoms, leading to the anticipated *averaged* moment of $3 \mu_B$ over the entire unit cell. These simulations have therefore shed a clarifying light on the atomic-scale origin of CrI₃'s magnetism and produced a valuable workflow that can be readily extended to a wide range of other 2D materials.¹⁷⁷ Additional details of this work can be found in Ref. 109.

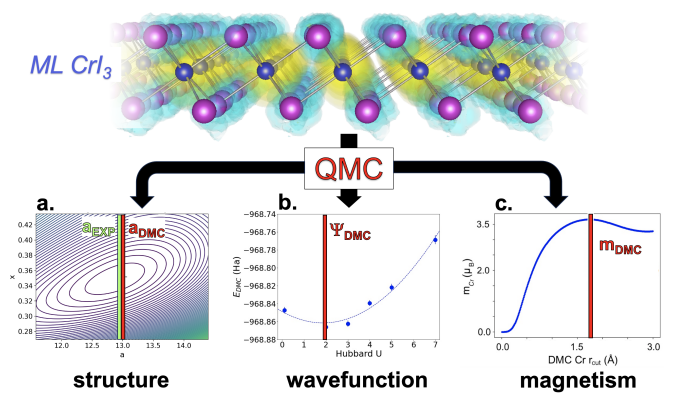


FIG. 1. To resolve the origin of monolayer CrI₃'s magnetism, we modeled this material in three key steps: We (a) first employed the surrogate Hessian line-search method to determine its high-accuracy geometry; (b) then, determined an optimal U at $U = 2$ to employ in our PBE+U trial wavefunctions; and (c) finally, integrated the resulting DMC spin density to obtain estimates of CrI₃'s magnetic moment of $3.62 \mu_B$. Adapted from Ref. 109.

2. Monolayer CrX₃

To expand upon this seminal work, we created a workflow that combines DFT+U and DMC methods to calculate magnetic properties of 2D CrX₃ ($X = \text{I, Br, Cl, F}$) with improved accuracy¹¹⁰. These structures were chosen as a case study since they have been extensively investigated with DFT¹⁷⁸, have been experimentally synthesized, and have a finite transition temperature^{16,178}. We can map our ab initio quantities to a 2D model spin Hamiltonian to obtain properties such as T_c ^{160,162}. The model Hamiltonian contains easy axis single ion anisotropy (D), Heisenberg isotropic exchange (J), and anisotropic exchange (λ),

$$\mathcal{H} = - \left(\sum_i D(S_i^z)^2 + \frac{J}{2} \sum_{i,i'} \vec{S}_i \cdot \vec{S}_{i'} + \frac{\lambda}{2} \sum_{i,i'} S_i^z S_{i'}^z \right). \quad (3)$$

The sum over i runs over the lattice of Cr atoms (magnetic atoms) and i' runs over i 's nearest-neighbor Cr atoms; only nearest-neighbors are needed because the magnetic moments are strongly localized on the Cr atoms. $D > 0$ prefers off-plane easy axis, $J > 0$ prefers FM interactions, and $\lambda = 0$ results in fully isotropic exchange. This model Hamiltonian can additionally contain terms for Dzyaloshinskii-Moriya interactions and Kitaev interactions, but for this work, we limit our Hamiltonian to containing J , λ , and D terms. Note that in the following sections J refers to the Heisenberg exchange and not the J in the DFT+U+J formalism¹⁷⁹. Two magnetic orientations can be constructed from the CrX₃ unit cell (shown in Fig. 2b): the ferromagnetic (FM) (two spin up Cr atoms) and antiferromagnetic (AFM) (one spin up and one spin down Cr atoms) orientations. J , λ , and D can be extracted from non-collinear (spin-orbit) DFT calculations. Specifically, computing the energy differences between configurations that have

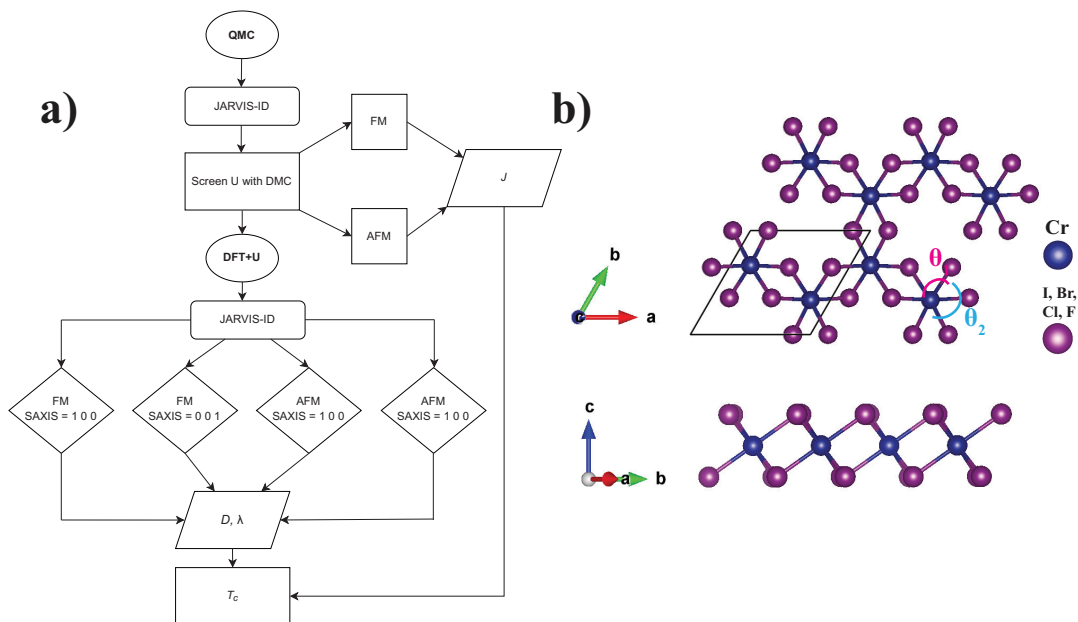


FIG. 2. (a) The workflow used to extract the accurate magnetic properties of a 2D magnetic system using a combined DFT+U and QMC approach and b) top and side view of the structure of 2D CrX₃ (X = I, Br, Cl, F). Adapted from Ref. 110.

an easy axis rotation of 90° and non-rotated configurations for FM and AFM magnetic orientations.

These results can be systematically improved with DMC and a full schematic of this workflow is shown in Fig. 2(a). Firstly, the nodal surface of the trial wavefunction can be optimized by changing the U value (variationally determining which U value yields the lowest energy). Secondly, by performing DMC for the FM and AFM configurations, J can be estimated. In our case, these DMC energies are collinear (without spin-orbit coupling). Although SOC has been implemented in DMC, the energy differences needed to compute magnetic anisotropy parameters are smaller in magnitude than the DMC uncertainty. For this reason, we used the optimal U value determined from the nodal surface optimization (in our case, it was $U = 2$ eV for CrI₃ and CrBr₃, similar to Ref. 109) to perform DFT+U calculations to obtain D and λ . The starting geometry for our DMC calculations was obtained from the vdW-DF-optB88⁷⁹ functional (vdW-DF-optB88 produces a geometry for CrI₃ in near-perfect agreement with experiment¹⁶⁸ and Ref. 109). After extracting our parameters from our combined DMC/DFT+U approach, we can plug those parameters into analytical models such as the one developed by Torelli and Olsen¹⁶⁰ to estimate the Curie temperature. We determined a maximum T_c of 43.56 K for CrI₃ and 20.78 K for CrBr₃, which is in excellent agreement with the measured values of 45 K¹⁶ and 27 K,^{180,181} respectively. More details of this work can be found in Ref. 110.

3. Monolayer MnO₂

The workflow from Section III A 2 is general and can be extended beyond CrX₃ materials. In this work, we applied the same workflow to monolayer MnO₂¹⁸². Single layer MnO₂ is a commercially available transition metal oxide semiconductor that has been synthesized and studied with DFT^{35,183–189}. Kan *et al.*¹⁸⁹ predicted the FM ordering to be more favorable than the AFM ordering with PBE+U (using a U correction of 3.9 eV obtained from previous literature¹⁹⁰). J was extracted from these calculations and a magnetic coupling Hamiltonian based on the Ising model was used to perform classical Monte Carlo simulations to obtain a Curie temperature of 140 K¹⁸⁹. Although these PBE+U results are promising, there are aspects that can be revisited with more accurate methods such as DMC.

First, previous results and our own DFT+U benchmarking results show that the energy difference between the FM and AFM orientations is heavily dependent on the functional and U value^{182,189}. In fact, our DFT benchmarking shows an FM-AFM energy difference range of -55 meV to 18 meV, indicating that there is a discrepancy regardless of whether the FM or AFM orientation is more energetically favorable. Using the same workflow from Section III A 2, we determined an optimal U value of 2.5 eV and a J value of 1.2(5) meV with DMC (see Fig. 3). The starting geometry for our DMC calculations was obtained from the strongly constrained appropriately normed (SCAN)⁶⁶ meta-GGA functional (due to the fact that the SCAN computed lattice constant is in near-perfect agreement with experiment¹⁸³). Using this optimal U value in subsequent PBE+U calculations, we find monolayer MnO₂ to have out-of-plane magnetic anisotropy. From these

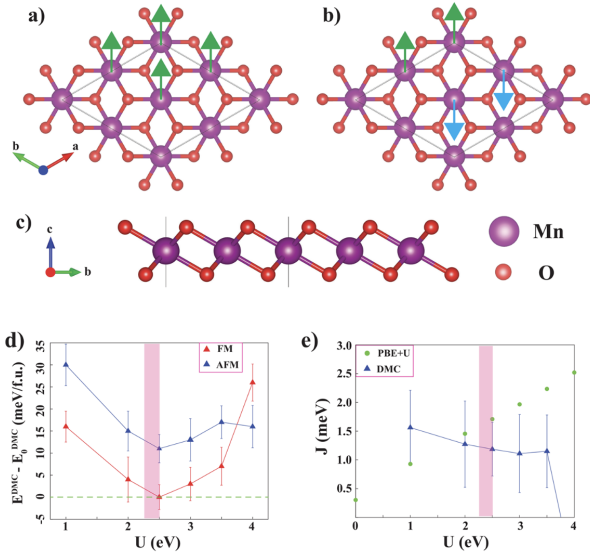


FIG. 3. (a, b) Top and (c) side depictions of monolayer MnO_2 , where ferromagnetic ordering is shown in (a) and antiferromagnetic ordering is shown in (b) by green arrows. (d) Shows the total relative DMC energy as a function of U parameter for the FM and AFM orientations and (e) shows the nearest-neighbor Heisenberg exchange (J) as a function of U calculated with DMC (blue) and PBE+U (green). The magenta rectangle represents the fitted optimal U value of 2.4(1) eV. Adapted from Ref. 182.

magnetic constants, we estimated the maximum value of T_c to be 28.8 K. In addition, we analyzed the spin density obtained from DMC for Mn and O and compared these with those obtained from PBE+U. Specifically, we find that DMC predicts that the spin density of O atoms is polarized antiparallel with respect to the Mn atoms, which is in agreement with PBE+U ($U = 2.5, 3.5$ eV), but the opposite of what is computed with PBE+U ($U = 0, 1$ eV). More details of this work can be found in Ref. 182.

4. Monolayer 2H- and 1T- VSe_2

Monolayer VSe_2 has been a source of controversy throughout the theoretical and experimental literature, with substantial claims of near-room temperature ferromagnetism (from 291 K to 470 K^{149,191–193}). The T (octahedral phase (1T)-centered honeycombs) phase and the H (the trigonal prismatic phase (2H)-hexagonal honeycombs) phase (shown in Fig. 4) of 2D VSe_2 have a close lattice match and similar total energies, which makes it difficult to discern which phase is being observed experimentally^{149,191,194,195}. The difficulty discerning the relative stability of the phases and related structural uncertainty undoubtedly imply that the structural parameters are coupled to the magnetic properties^{149,191–193,196}. Similarly to Ref. 109 and Ref. 175, we used a combination of DMC, DFT, and the surrogate Hessian line-search structural optimization technique¹⁷⁴ to clarify the discrepancies in structural

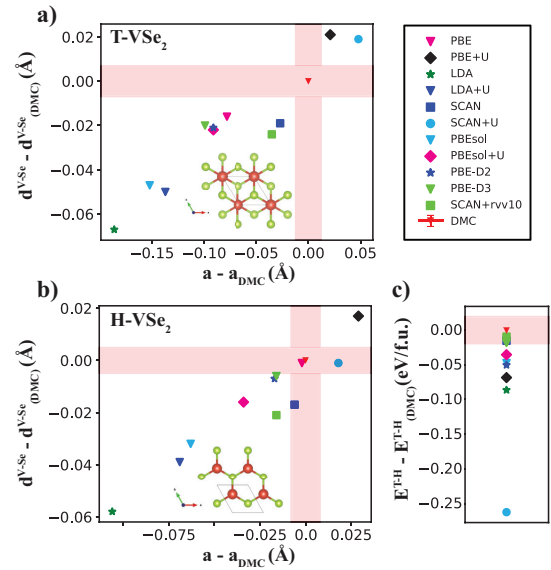


FIG. 4. The deviation of structural parameters (lattice constant (a) and V-Se distance ($d^{\text{V-Se}}$)) compared to the DMC results for (a) T- VSe_2 and (b) H- VSe_2 . (c) The deviation of the T - H energy from several different DFT functionals ($U = 2$ eV) relative to the DMC calculated T - H energy ($E^{\text{T-H}}$). The atomic structures are depicted in the insets. Adapted from Ref. 176.

parameters and relative phase stability of the T and H phases of monolayer VSe_2 .

Fig. 4 depicts a summary of DFT results (multiple functionals with and without U) alongside DMC (red bars) for the lattice constant (a), V-Se bond distance ($d^{\text{V-Se}}$), and the relative phase energy ($E^{\text{T-H}}$). As expected, there is a large disagreement between DFT functionals for a , $d^{\text{V-Se}}$, and $E^{\text{T-H}}$, indicating the need for a theory such as DMC. With DMC and the Hessian line-search method, we computed the lattice constant and V-Se distance to be 3.414(12) Å and 2.505(7) Å, respectively, for T- VSe_2 and 3.335(8) Å and 2.503(5) Å, respectively, for H- VSe_2 . The relative energy between the T and H phases was found to be 0.06(2) eV, with the H phase being lower in energy than the T phase in freestanding form. We then constructed a phase diagram between T and H with DMC accuracy and found that a H-to-T phase transition can be induced by applying small amounts of strain ($\approx 3\%$). More details of this study can be found in Ref. 176. As a follow-up to this work, the authors intend to focus on studying the magnetic properties of 2D T- VSe_2 with DMC methods, specifically running DMC for various magnetic configurations and predicting the transition temperature.

B. Electronic Properties

Electronic structure: It is now established that 2D systems such as graphene, phosphorene, and transition metal dichalcogenides belong to a class of materials that is exceptionally interesting for both fundamental research and for future use in

technology. The electronic structure of 2D systems is astonishingly rich, since it provides an unusual combination of periodicity and free boundaries, the possibility of stacking with new variational freedom (twistronics), significant effects related to the presence of substrates, and further potential modifications with doping, straining (straintronics), and related processing. Due to the presence of unique electronic phases, these systems pose a number of challenges for any theoretical or computational method.

It is useful to specify that, from the point of view of electronic structure theory, the 2D materials in this review are not strictly systems with electrons in a 2D plane, but rather 2D slabs with atomic thickness. Consequently, the electronic structure, one-particle orbitals, and other properties indeed depend on all three spatial coordinates. (Previous theoretical work has shown that the calculations of slabs have their intricacies, as can be seen for the homogeneous electron gas in a slab geometry, see Ref. 197.) This is important since many properties that apply to strictly 2D geometries might not apply or might be significantly modified. Clearly, electrons have a nonzero probability to be on either side of the material in the orthogonal z -direction, and they are not confined within a 2D (x, y) plane. This leads to the possibility of Janus materials¹⁹⁸ in which the opposing surfaces have different properties due to different functionalizations, doping, and symmetry-breaking. An important consequence of this may be seen in the electronic structure, as most clearly revealed by the dependence of the dielectric constant on the inter-electronic distance. In 3D solids, the dielectric constant grows monotonically until it saturates at large distances to the bulk value. In 2D materials, it initially grows, however, at the distance of a few atomic bonds, it exhibits a rather sharp maximum and then rapidly falls off to a small value. This small value corresponds to long-range distance vdW-like behavior where distant regions appear electrically neutral with typical dipole or higher order dispersive fluctuations. This implies that, at short distances, we see the effects of bonds which look like locally 3D material while at large distances the system exhibits dispersive effects resembling effective interactions with non-covalent character.

DFT and GW methods have been widely used to study the electronic structure of 2D systems. The accuracy of the former is determined by the XC-functional, whereas that of the latter by the unperturbed state and the way the perturbation expansion is terminated. This introduces significant biases between the two approaches as well as within each method. Quasiparticle band gaps typically between these methods by up to ≈ 1 eV. As a result, experiments are expected to provide the final answer. However, 2D materials typically need to be supported by substrates (quartz, sapphire, etc.) which compromises their 2D character by providing unintentional dielectric embedding. As shown in Fig. 5, the experimental effect of the tuning by the substrate is also of the order of ≈ 1 eV, complicating the comparison with calculations. In such a situation, QMC may provide the final answers and even challenge the achievable experimental accuracy. The situation is illustrated in Fig. 6 where the quasiparticle gap of monolayer phosphorene calculated by DFT (PBE and B3LYP), GW (G_0W_0 and GW_0 using

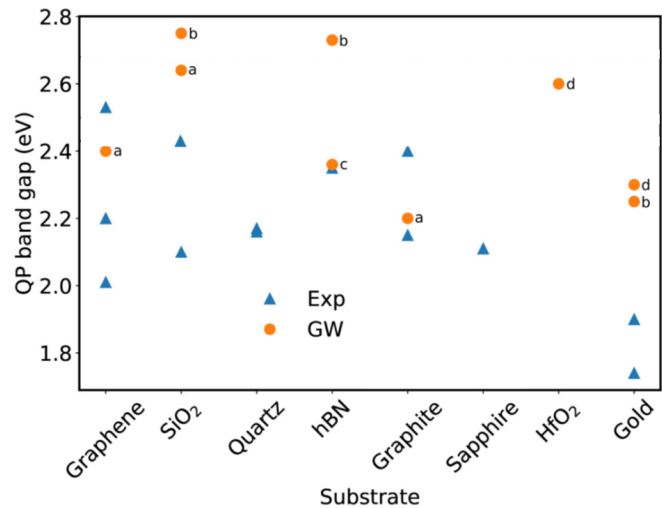


FIG. 5. Quasiparticle band gap of an MoS₂ monolayer on different substrates reported in the literature. The experimental results shown by blue triangles were obtained with scanning tunneling microscopy spectroscopy, absorbance, and angle-resolved (inverse) photoemission spectroscopy. The GW band gaps are shown by the orange disks. Adapted from Ref. 200.

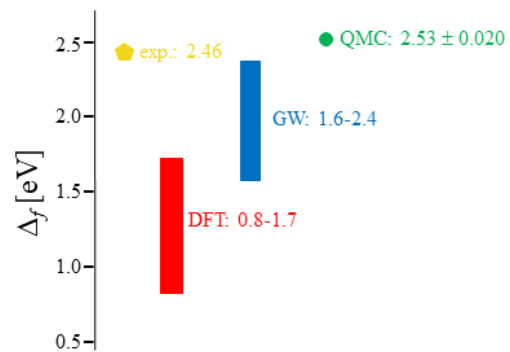


FIG. 6. Comparison of the quasiparticle band gaps of a freestanding phosphorene monolayer as calculated by the DFT, GW, and QMC methods against the experimental value measured on a freestanding sample¹⁹⁹. Adapted from Ref. 201 and 202.

both PBE and B3LYP wavefunctions), and QMC methods is compared to the rare result where the experimental band gap is measured on a freestanding sample¹⁹⁹. The QMC result is seen to agree with the experimental result almost with chemical accuracy, given that no vibronic effects were considered in the QMC calculation, while both the DFT and GW methods tend to underestimate the band gap and can feature a very wide spread in their calculated values.

Excited states: One of the key characteristics that is important for applications is the value of the band gap and its sensitivity to variations that come with the impact of doping, substrates, strain, multilayer stacking, and both internal (e.g., spin-orbit) and external influences. In QMC calculations of band gaps the key complications come from two main sources of error, namely, finite-size and fixed-node biases. The fixed-node error is determined by the quality of the antisymmetric

part of the trial function which is often just single-reference since robust methodologies for multi-reference wavefunctions for periodic systems are under development. In QMC the band gaps can be calculated essentially by two approaches as outlined in the following.

-Fundamental band gap: One way is to use the definition of the fundamental gap which implies charging the system with N electrons by an additional electron ($N + 1$), then by an additional hole ($N - 1$) and calculating the response $\Delta_f = E(N + 1) + E(N - 1) - 2E(N)$ as the difference of total energies for charged and neutral states. This has been routinely applied in 3D and often also to a number of 2D systems^{175,203–205}. Some cases showed a minor (0.1 to 0.2) eV upward bias that can be qualitatively understood by the fact that cation typically relaxes more than the anion since the anionic state with its conduction state occupation should typically involve more than a single-configuration. Hence, the resulting minor bias which is, in fact, surprisingly small considering just a single-reference approximation of the nodal hypersurfaces for both charged and neutral systems.

We note that additional bias could come from finite size scaling since the charged states have to be compensated in order to make the periodic supercell neutral. The commonly used compensation by the opposite sign constant background charge eliminates the leading (monopole) diverging term, however, it does not perfectly compensate the subleading terms and although the impact mostly appears to be small²⁰⁶, this need not be valid. There are also subtleties in using charge compensation and Ewald sums when treating 2D systems and increasing size of box in the orthogonal direction. An example for band gap in hexagonal Boron Nitride (hBN)²⁰⁷ is shown in Fig. 7 where first the in-plane finite-size scaling is shown for various lengths of the simulation cell vector orthogonal to 2D material (L_z) with the inset showing the L_z convergence of the in-plane scaled band gaps. It is seen that as the neutralizing background dilutes with increasing L_z , the band gap appears to diverge with L_z due to artificial charge decompensation. In fact, proper compensation for slab geometries in real systems is still a matter of current studies²⁰⁷. In addition to our own work, Hunt *et al.*²⁰⁵ previously studied the electronic and excitonic properties of 2D hBN with DMC, carefully taking finite-size errors and vibrational renormalization into account.

-Promotion band gap: The second method is closer to experiments that provide optical spectrum, namely, promotion of an electron from valence into the conduction band. This excitation can be direct or indirect (i.e., approximately modelling a phonon-assisted optical excitation). Since the optical spectrum typically involves excitonic states, it is good to distinguish the two possibilities that can occur:

Wannier excitons: In systems with strong covalent bonds and large dielectric constants, one typically encounters Wannier excitons with exciton binding energies from meVs to a few tens of meV and therefore the effect on the electronic bands is very small. This is what is observed in many such calculations²⁰⁶ since any relaxation into the excitonic state provides only very minor effects which are at the level of statistical error bars in DMC.

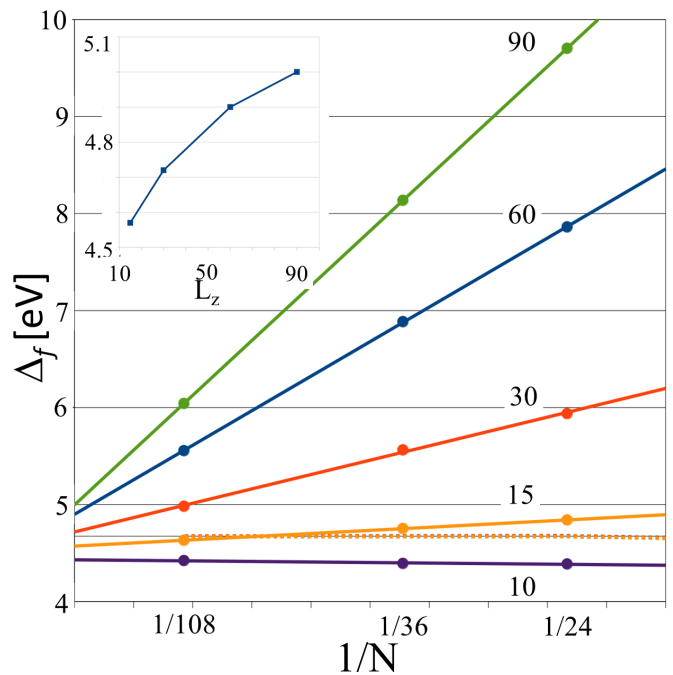


FIG. 7. Behavior of the band gap in a 2D supercell of hBN, computed from charged systems using uniform neutralizing background. In-plane finite-size scaling with box height L_z (simulation cell vector length orthogonal to 2D material) ranging from 10 Å to 90 Å as parameter. The inset shows the L_z convergence for in-plane converged gaps. Example from a DFT-PBE study. The broken horizontal orange line shows the HOMO (Highest occupied molecular orbital) - LUMO (Least unoccupied molecular orbital) gap which is converged at $L_z = 15$ Å.

Frenkel excitons: For systems with possible presence of excitons with binding energies larger than 0.5 eV (Frenkel excitons) the situation is more complicated.

(i) In covalent or mainly covalent materials, the one-particle orbitals from band structure calculations, such as DFT, HF, DFT+U, *etc.*, provide Bloch orbitals that enter the trial wavefunction. This determines the symmetry and periodicity of the resulting trial wavefunction. In most cases, this constraint "locks" the overall band structure picture also in QMC calculations. Typical QMC effects come as band gap shifts, however, the overall structure of the bands remains pretty much the same. Therefore, due to the nodal constraint, the relaxation to more localized, more strongly bonded non-Bloch excitonic state is strongly hindered. This is easy to understand since the localized exciton wavefunction in Bloch state basis necessarily requires large multi-reference expansion. Therefore, any relaxation to an excitonic state is mostly absent^{201,203}, which shows that the overlap of the exciton and Bloch state promotion is negligible or small. Note that in the non-interacting limit the overlap identically vanishes showing thus the dominant one-particle nature of this behavior.

(ii) However, in some cases the nodal constraint might be less restricting. One such possibility could occur if the excitonic state and Bloch excitation share a subgroup of symmetries. Possible mixing of such two states would have to be car-

ried out explicitly. Another possibility could occur in environments with rapidly changing charge densities (such as ionic bonds or 2D layered materials with large space between the layers) since absence of proper tails in the trial function can hinder the needed charge redistribution. Therefore, the charge relaxation and/or localization could be compromised with resulting energy decrease towards the excitonic state. This could be observed in some systems¹⁷⁵, although the signal is comparable to the error bar range due to complications with thermodynamic limit extrapolation. It is clear that this requires a new leap in quality of the trial function in order to quantify the involved effects. There is no fundamental obstacle in carrying out such analysis, the issues are mainly technical due to limited availability of appropriate software tools. Clearly, one would need to rebuild the trial function with localized orbitals, possibly orthogonalize it to the Bloch excited state that corresponds to the fundamental gap excitation, to make the distinction of fundamental vs. excitonic state explicitly. Note that this is routinely done in molecular studies since many quantum chemical codes enable to carry out corresponding calculations. Another such case could occur for vdW molecular crystals, where the localized state(s) on a single molecule could dominate the low-lying excitation spectrum since the periodicity causes only minor energetic shifts and results in very flat low-lying bands. More dispersive bands appear in significantly higher scattering states in the conduction part of the spectrum.

Several QMC works have computed the fundamental and promotion band gap to estimate the exciton binding energy of 2D systems^{175,203–205}. Additionally, there have been studies by Szyniszewski *et al.*²⁰⁸ and Mostaani *et al.*²⁰⁹ that have utilized DMC coupled with other theoretical approaches to successfully estimate biexciton and trion energies in 2D semiconductors.

1. Monolayer phosphorene and MoS₂

Alongside graphene, phosphorene and transition metal dichalcogenides belong to the most studied 2D semiconductors. Their band gap is often direct. In phosphorene the band gap is direct at Γ in a monolayer and few-layers and direct even in bulk black phosphorus albeit at the Z point. In MoS₂ it is direct at the K-point only in the monolayer. In addition, 2D semiconductors usually possess ultrahigh carrier mobility and field-effect switching ratios, which make them ideal materials for field-effect and digital logic transistors. 2D semiconductors with appropriate and tuneable direct band gap have achieved extremely efficient photon absorption, emission, and photoelectric conversion and have been widely used in the field of optoelectronic devices. To meet more demands, various techniques have been exploited to modulate their properties, including doping, alloying, forming vdW heterostructures, and strain engineering or straintronics^{210,211}. Due to their atomic thickness, 2D materials are highly sensitive to external perturbations, such as strain. Their resilience to mechanical deformations allows application of strains well in excess of 10%. By applying strain, the lattice and electronic

structure is modulated as well as their various properties, such as the carrier mobility. MoS₂ has traditionally been considered the quintessential straintronic material for which many straintronic experiments have been performed²¹².

Recently, the straintronic response of two 2D semiconductors, monolayer phosphorene and MoS₂ has been studied using fixed-node QMC methods^{202,213}. In phosphorene the strain was applied in both armchair and zigzag direction by adjusting the a and b lattice parameters, see Fig. 8, considering deformations of up to $\approx 10\%$. Determination of strained properties was treated as a full optimization problem in the space of four structural variables: lattice parameters a , b and two internal parameters x , y ²⁰². Around the minima the ground-state potential energy surface (PES) E_0 was fitted by 4D paraboloid functions used to find the lowest point on the x , y subspace, leaving to further minimize only bivariate functions $E_0 = f(a, b)$. The excited state E_1 was computed only at the minimum for the internal parameters x , y and the quasiparticle band gap for any applied strain was computed as $\Delta_f = E_1 - E_0$, subject to finite-size scaling. In MoS₂ only diagonal strain was considered and a scaled down version to two parameters (one lattice parameter a and one internal parameter x) was used leaving a single function $E_0 = f(a)$ to optimize²¹³. This approach obviously allows to study the 2D materials both in- and out-of equilibrium.

For phosphorene in equilibrium, we obtain ($a = 3.30 \pm 0.003$ Å), ($b = 4.61 \pm 0.006$ Å), and ($\Delta_f = 2.53 \pm 0.020$ eV), see also Fig. 6. This value of the quasiparticle gap is in excellent agreement with the experimental value for freestanding monolayer phosphorene of 2.46 eV¹⁹⁹, see also Fig. 6 (keeping in mind that neglecting adiabatic, vibronic, and zero-point vibrational energy tends to increase the gap value compared to experiments). The QMC optimized structure exhibits noticeable differences with respect to the structure derived from the 3D black phosphorus crystal especially in the b parameter (4.376 Å). This variation of the b parameter in 3D crystal is due to partially chemical interlayer interaction which reduces it by $\approx 5\%$ and is almost completely absent from MoS₂, where the interlayer interaction in the 3D crystal is fully vdW²¹³. These trends are fairly well described by the DFT-PBE functional and not as well by the hybrid functionals²⁰². All gaps in the DFT treatment are appreciably smaller than the QMC value. As expected, the smallest value by about 2 eV is obtained by the DFT-PBE functional. The hybrid functionals yield larger values but fail in predicting the equilibrium geometries.

The calculated band gap phase diagram for phosphorene is shown in Fig. 8. The diagram was constructed by calculating the boundaries between the $\Gamma \rightarrow \Gamma$ and a band gap at Γ formed by interchange of LUMO (Least unoccupied molecular orbital) and LUMO + 1 states ($\Gamma \rightarrow \Gamma'$) and the boundary between the $\Gamma \rightarrow \Gamma$ and $\Gamma \rightarrow X$ due to applied strain from the intersections of the respective PESs. As for the first boundary, while both gaps are direct at Γ , the nature of the excited state is different if the order of unoccupied states is interchanged. The new LUMO state has a differing curvature, hence, the transport properties in the conduction band are expected to be significantly modified which goes in line with

straintronic as a tool for electrom effective mass modification. The QMC boundaries outline a strain tuning area for the direct $\Gamma \rightarrow \Gamma$ band gap more than twice as large as that determined by DFT-PBE (and similarly by hybrid functionals²⁰²). This area extends mostly into the region of tensile strain which is important to prevent the material from wrinkling at higher compressive loads. The DFT results are qualitatively similar, see Fig. 8, irrespective of the DFT functional. All PESs (QMC, DFT) are rather parallel, albeit strongly shifted vertically in energy and their intersections all feature similar curvatures. The primary differences consist of relative band offsets (magnitude of band gaps) and the location of the minima. These two factors play havoc with the form of the phase diagrams. In phosphorene, Fig. 8, the offsets reduced the $\Gamma \rightarrow \Gamma'$ section of the diagram by $\approx 50\%$ in phosphorene²⁰². In MoS₂, where the strain tuning areas are more compressed, the different treatments were predicting qualitatively different tunings in the $K \rightarrow K$ section: QMC mainly in the compressive region, GW and B3LYP exclusively in compressive, whereas HSE mainly into tensile²¹³. Phosphorene was also found to feature high values of the gauge factor of the order of 100 meV per %, which is comparable to MoS₂. Combined with the huge tuning area of several percent leaving the direct nature of the band gap intact, this provides a colossal straintronic tunability of phosphorene with the tuning limit likely determined only by the mechanical breakdown of the material. The range of band-gap tuning by applied strain while maintaining the direct band gap at Γ is truly huge with achievable values of the band gap in the range 2.1 eV to 3.8 eV. Surprisingly, this is at complete variance with the straintronic response of the quintessential straintronic material, monolayer MoS₂, which features similar gauge factor but an order of magnitude smaller tuning area²¹³.

2. Fluorographene

Fluorographene (FG) is a 2D stoichiometric graphene derivative (C₁F₁) material that exhibits a large band gap due to the out of plane carbon orbital saturated by bonding with fluorine. Some of the key properties of interest involve its large band gap, dielectric characteristics as well as potential surface physics and chemistry applications. Interestingly, the fundamental and optical band gaps as well as related derived properties has not been fully settled until recently. In particular, from experiments the onset of FG optical absorption spectrum has been estimated to lie between 3 eV - 5 eV. The fundamental gap from GW for the electron self-energy suggests a range of 7 eV to 8 eV. In addition, their excitonic effects appear to be very strong and the Bethe-Salpeter equation (BSE) confirmed the exciton binding energy of FG close to 2 eV, regardless of technicalities such as orbital sets or related parameters. In our study²⁰³ we have employed both the highly accurate GW-BSE approach as well as DMC to ascertain these excitation characteristics. We found that the fundamental band gap from thoroughly converged GW and consistently extrapolated DMC methods agree within the error bars on value of 7.1(1) eV, establishing the reference for this material from two independent many-body approaches. Careful analysis of the BSE

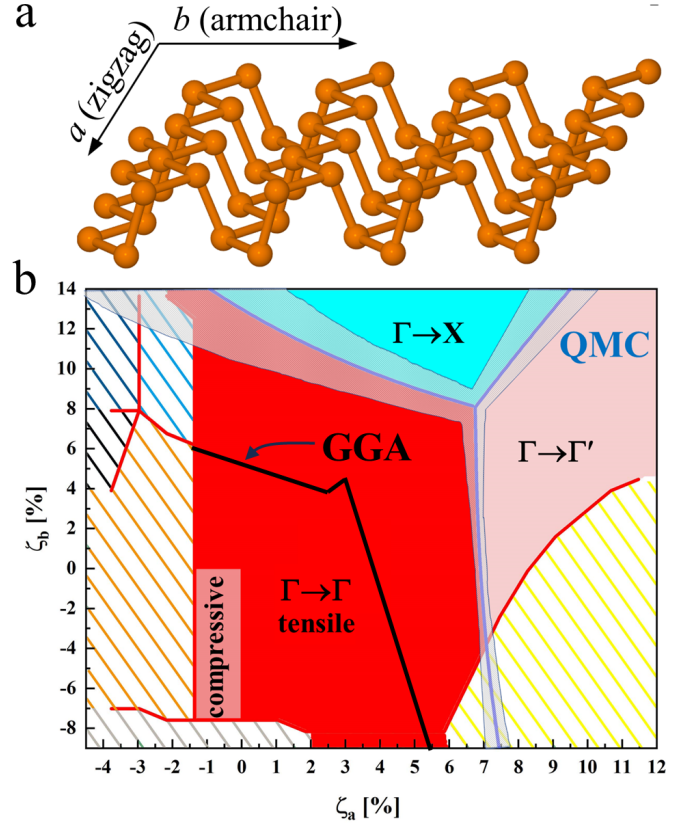


FIG. 8. a) Model of the atomic structure of monolayer phosphorene with the lattice parameters a and b indicated. b) Phase diagram of the various excitations in the ζ_a/ζ_b plane. Blue lines correspond to fixed-node QMC results with the overlays outlining the $\pm 1\sigma$ (standard deviation) error bar, hatched regions and the region outlined by black lines in the $\Gamma \rightarrow \Gamma$ region correspond to PBE results. Adapted from Ref. 202.

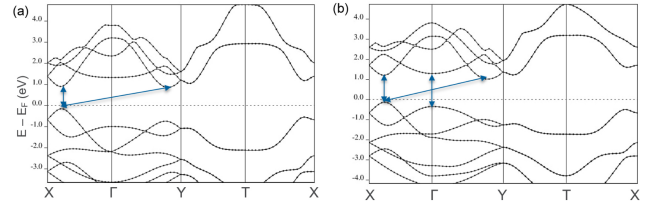


FIG. 9. Monolayer GeSe band structure for (a) PBE and (b) DMC geometry calculated by PBE functional. Blue lines represent candidates for direct and indirect gap. Adapted from Ref. 175.

results confirmed ≈ 1.9 eV exciton binding and provided additional insights into the structure of the excitonic state based on the projection of the BSE exciton on the Bloch states.

3. Monolayer GeSe

GeSe is a p-type semiconductor that has been widely studied because of its unique optical properties. Its bulk structure is generally known to possess a measured indirect gap

of 1.07 eV to 1.29 eV at room temperature^{214–216}. However, it was recently reported that a direct gap minimum of 1.3 eV was measured via optical spectroscopy²¹⁷. This controversy is mainly due to the small difference between the direct and indirect gaps in bulk GeSe, and its high sensitivity in the method used for the measurement. In addition, DFT studies on GeSe showed strongly varied band gap energy and optimized lattice parameters depending on choice of XC functionals^{52,218–220}. These limitations on computing accurate optical and structure properties from DFT leads us to confirm that the use of more accurate method, which can describe exact optical and structural properties at the same time, is highly desired on the GeSe structure.

We estimated the DMC direct gap of bulk GeSe to be 1.62(16) eV, which is in the excellent agreement with the experimental value of 1.53 eV²²¹. Based on this DMC direct gap and our DMC quasiparticle gap result of 1.95(21) eV, bulk GeSe is expected to possess a weak exciton binding energy of ≈ 0.3 eV. Because the exact geometry for the GeSe monolayer is experimentally not known yet, its geometry is fully optimized using a surrogate Hessian-based parallel line search method¹⁷⁴ (similar to Ref. 109 and 176). In the optimization process, the GeSe monolayer shows a shallow PES minimum over a large range of lattice parameters, which explains the high sensitivity of optimized DFT geometries to the choice of XC functional.

In the PBE band structure for the GeSe monolayer, the DMC monolayer geometry shows a small direct gap of 1.50 eV at the Γ point from the PBE result, which is competitive to the direct (1.24 eV) and indirect gaps (1.02 eV) located between the X and Y high symmetry point (see Fig. 9). Large differences in direct gap at the Γ -point between the PBE (2.32 eV) and DMC geometries (1.50 eV) show that the monolayer band structure is very sensitive to its geometry, suggesting that controlling strain on the monolayer can be a route to manipulate the electronic and optical properties of monolayer GeSe. Additional details can be found in Ref. 175.

4. Monolayer GaSe and Ga_xSe_{1-x} Alloys

Post Transition Metal Chalcogenides (PTMCs) are a class of 2D materials that have suitable band gaps for photo-voltaics and transistors^{222–231} and have lower exciton binding energies than TMDs^{222–224}, which make them suitable for water-splitting applications²³². Monolayer GaSe is a PTMC that has been reliably synthesized and measurements of the quasiparticle gap, optical gap, and lattice constant have been performed^{41,43–50}. The experimental lattice constant of monolayer GaSe has a measured value of $a = b = 3.74$ Å⁴⁷. In addition, 2D GaSe has an experimental indirect band gap of 3.5 eV (on a graphene substrate)⁴³, which is much larger than the bulk GaSe band gap of 2.0 eV. The optical band gap has been measured to be 3.3 eV⁴⁵, which implies an exciton binding energy lower than 0.2 eV. Despite these well-characterized measurements, computational results can significantly vary based on which functional is used²⁰⁴.

The most apparent discrepancy is the location of the con-

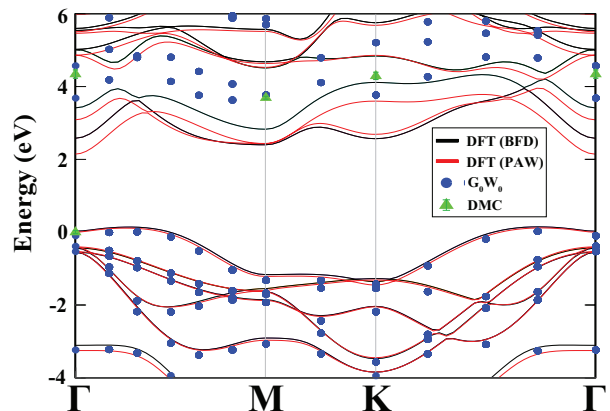


FIG. 10. Monolayer GaSe electronic band structure of computed with PBE using Burkatzki-Filippi-Dolg (BFD)^{233,234} pseudopotentials (black), projector augmented wave (PAW)^{235,236} pseudopotentials (red), and G_0W_0 using PBE wavefunctions and PAW potentials (blue). The DMC excitation energies and error bars (with respect to the Γ point) are given in green at each high symmetry point. Adapted from Ref. 204.

duction band edge at each high symmetry k-point. The energy differences are so small between each high symmetry point (≈ 0.2 eV to 0.3 eV) that different functionals/pseudopotentials can predict the gap value to have different values and some methods even incorrectly predict the gap to be direct. Improvements to the underestimation of the gap can be achieved using methods such as GW or BSE, but these results depend on which functional is used to generate the starting wavefunction and the indirect/direct discrepancy still exists. We used DMC to obtain the optimal lattice constant by isotropically scaling the lattice and finding the energy minima. To demonstrate the weak dependence that DMC has on the starting functional, we created DMC the trial wavefunction with PBE, LDA and SCAN functionals and performed the same calculation. We computed 3.74(2) Å for DMC-PBE, 3.75(1) Å for DMC-LDA, and 3.75(1) Å for DMC-SCAN, which is in close agreement with experiment. With DMC, we confirmed that 2D GaSe is an indirect material (Γ -M) with a quasiparticle gap of 3.69(5) eV, which is in excellent agreement with the experimental value. From our calculation of the optical band gap, we obtained a maximum bound on the exciton binding energy to be 80 meV, which confirms that GaSe is a 2D material with a lower exciton binding energy than most TMDs⁹, making it suitable for water-splitting applications. More details of this work can be found in Ref. 204.

We extended our approach to 2D Ga_xSe_{1-x} alloys²³⁷, since alloying is a promising technique to control the properties of single and few layer structures^{238–245}, which includes PTMCs^{41,246–249}. Studying alloys with accurate computational methods is a difficult endeavor because usually the local atomic ordering and stoichiometry of the different alloyed structures is unknown. In order to tackle this issue, ab-initio methods have been coupled with methods such as Cluster Ex-

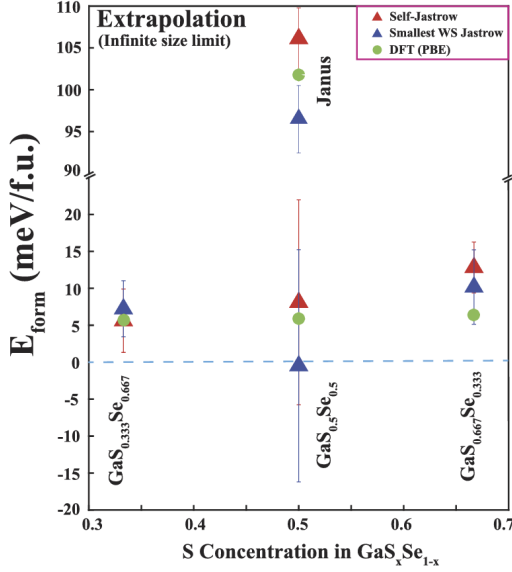


FIG. 11. The constructed energy hull diagram for monolayer $\text{GaS}_x\text{Se}_{1-x}$ obtained with PBE (green) and DMC (red) using the structures own Jastrow functions and green reusing the Jastrow functions from the alloy with the smallest Wigner-Seitz radius), adapted from Ref. 237.

pansion to construct the energy hull diagram of an alloy system, which allows us to determine if a structure is thermodynamically stable and possibly exist in nature²⁵⁰.

In this work, we designed a high-throughput workflow to compute the energy hull diagram of an alloy system with QMC methods, using 2D $\text{GaS}_x\text{Se}_{1-x}$ as a case study. To achieve this, we proposed a method we deem *Jastrow sharing*, which involves recycling the optimized Jastrow parameters between various alloys with different stoichiometries. Specifically, we optimized the Jastrow parameters of the alloy with the smallest Wigner-Seitz radius and used those parameters for other structures of interest in the alloy system. We demonstrated that this eliminates the need for unnecessary VMC Jastrow optimization simulations and can reduce the total computational time by 1/4 (75 % of the original computational time). After testing the validity of this *Jastrow sharing* approach, we went on to compute the alloy formation energies with DMC (extrapolated to the thermodynamic limit) for selected points on the energy hull diagram. This method can easily be implemented for other 2D alloy systems where the Jastrow sensitivities of the pseudopotentials of the atoms in the system are low, which can eventually aid in accurate studies of more complex alloy systems (i.e. alloying 2D transition metal oxide materials). Additional information from this study can be found in Ref. 237.

5. Spin-orbit effects, topological states

Layered RuCl_3 for Kitaev's spin liquid: Recently, the QMC method has been extended to spin-orbit Hamiltonians

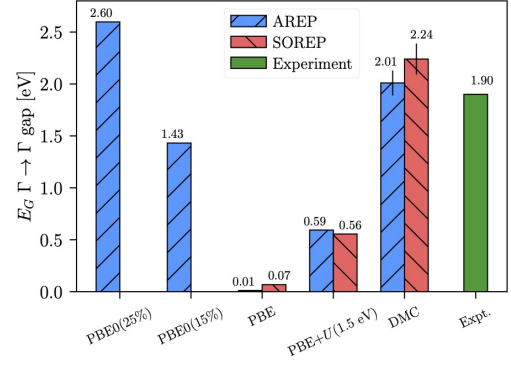


FIG. 12. The band gaps of RuCl_3 system compared with experiment. Calculations were done by several methods such as hybrid $\text{PBE0}(w)$ ^{74,75}, where w denotes percentage of exact exchange in two ways: averaged spin-orbit (AREP) and explicit spin-orbit (SOREP), adapted from Ref. 122.

with trial functions built upon two-component spinors and the spin-space sampled from an overcomplete set of spin configurations^{251,252}. For the first time we have applied this methodology to layered RuCl_3 ¹²², where claims of sizeable contributions of Ru atomic spin-orbit to gap opening have been claimed^{253,254}. Our calculations did not find support for this scenario. We found that the quasi-particle band gap opens due to expected significant Hubbard repulsion on the Ru atom. That proved to be the dominant effect while spin-orbit provides a mild shift of approximately 0.2 eV, as also expected for the intermediate strength of the atomic spin-orbit for the Ru atom (see Fig. 12).

Somewhat larger impact of the spin-orbit was observed in the cohesive energy, however, this is caused almost exclusively by the larger shift in high symmetry isolated Ru atom, not in the solid where the hybridization partially quenches and averages the corresponding splittings. We note that RuCl_3 is considered to be a promising candidate for realization of Kitaev spin liquid with low-lying collective states. However, that these are in the meV range (i.e., much smaller than the difference between ferromagnetic and antiferromagnetic states), hence outside the statistical resolution of current valence electronic structure QMC. Even if such wavefunction could be constructed, the presence of Kitaev physics presence would be hidden in the statistical noise and very extensive calculations would be needed to discern such a signal. Additional information from this work can be found in Ref. 122.

Layered TbMn_6Sn_6 for Chern magnets: A distinct class of materials, RMn_6Sn_6 , where R denotes a rare-earth element, displays rich and intricate physical phenomena such as strong electron-electron correlations, spin-orbit effects as well as possibilities of forming states with topological order. This stems from structural peculiarities with 2D Kagome layers of Mn interlaced by R and Sn layers. In this respect, the rare-earth Tb atom is of particular interest since it is the only R-element that forms an out-of-plane spin order compound. Experiments showed indications that TbMn_6Sn_6 is close to real-

izing a quantum-limit Chern magnet, as predicted by the Haldane model. Indeed, Kagome lattice geometry with an out-of-plane magnetization formed by the Mn atoms and the presence of strong spin-orbit coupling (SOC) originating from the Tb and Sn atoms provide the necessary conditions for opening the Chern gap. In our very recent study Ref. 255, we use DMC and DFT with Hubbard U (DFT+U) calculations to examine the electronic structure of TbMn_6Sn_6 . We find that DFT+U and single-reference QMC calculations exhibit the same over-estimation of the magnetic moments as meta-GGA and hybrid density functional approximations. Our findings point to the need for improved orbitals as well as wavefunctions for this class of materials. We have concluded that significant multi-reference effects have to be included in order to capture the static correlations which are necessary for an accurate prediction of magnetic properties. We have probed for the occurrence of topological order, where we have explored DFT+U with Mn magnetic moments adjusted to experiment. We have observed the Dirac crossing in bulk to be close to the Fermi level, within ≈ 120 meV, in agreement with the experiments. The possibility of crossing the Fermi level has been further enhanced in non-stoichiometric slab calculations, keeping re-actualization of Chern magnetism in this limit within the experimental reach. More information can be found in Ref. 255.

C. Interlayer Interactions

Layering 2D materials offers additional degrees of freedom which allow us to explore the correlation between interlayer coupling and physical properties. This exploration can lead to the emergence of novel electronic states in 2D materials. Interlayer coupling in these layered 2D materials varies widely, ranging from purely dispersive interactions, such as those seen in bilayer graphene^{256,257}, to complex interactions involving weak interlayer chemical bonding and even metallic bonding, in addition to vdW interactions. This complexity in interlayer interaction has been verified through X-ray density investigations for a 2D transition metal dichalcogenide material²⁵⁸. It is important to note that vdW interactions among these interactions are a many-body phenomenon stemming from non-local electronic correlations induced by the instantaneous fluctuation of electron density. These interactions may not be adequately captured by standard DFT frameworks, highlighting the need for a more sophisticated theoretical framework that can address these interactions equally. Such a framework is essential for capturing the diverse interlayer coupling which could vary depending on different stacking modes or twisting degrees of freedom. To illustrate this point, we present examples of DMC calculations aimed at investigating the nature of interlayer binding in 2D layered systems, providing a comprehensive understanding of interlayer coupling beyond what DFT offers.

1. Bilayer Phosphorene

Layered phosphorene allotropes have garnered a great deal of interest because of its layer dependent properties exemplified with band gaps of black phosphorenes varying from 2.26 eV at the monolayer limit to 0.3 eV for the bulk^{260–262}. This is understood to be driven by hybridization of valance p_z orbitals between the adjacent layers, which leads interlayer interactions of layered phosphorenes to be not purely dispersive as compared to those of bilayer graphene interpreted as a typical vdW system.

The distinct interlayer interaction of phosphorenes from the work of Shulenburger *et al.*²⁵⁹ is revealed through Fig. 13 presenting DMC interlayer binding energy curves for AA- and AB-stacked bilayer black phosphorenes. There is a significant energy difference of interlayer interactions (≈ 18 meV per atom) and interlayer separations (≈ 0.6 Å) for AA- and AB-stacked bilayer black phosphorenes, not consistent with the vdW interaction between two homogeneous slabs. This is contrast to the case of bilayer graphene showing difference of 6 meV/atom and ≈ 0.1 Å for interlayer binding energies and separations, respectively^{256,257}. Furthermore, the charge density redistributions computed with DMC for the two stacking modes shows a delicate difference in the interlayer region where AB and AA yield the charge depletion and accumulation, respectively. This feature demonstrates the nature of interlayer interactions in black phosphorenes to be complicated, not characterized by purely dispersive interactions.

Additionally, blue phosphorene, a 2D phosphorus allotrope with a puckered honeycomb structure, shows interlayer binding properties analogous to those of black phosphorene, according to our DMC study reported in Ref. 264. Furthermore, as the interlayer distance decreases, a blue phosphorene bilayer could exhibit a semiconductor-to-metal transition with the metallic state being manifested at short interlayer distances comparable to the intralayer bond length²⁶³, which is observed for the A_1B_{-1} stacking mode, one of five possible bilayer stacking modes of a puckered honeycomb structure²⁶⁵. A successful capture of this feature requires a well-balanced description of long-range dispersive forces and short-range chemical bondings with DMC because DFT calculations based on different exchange-correlation functionals show large inconsistency in predicting equilibrium interlayer binding energies and interlayer separations (as displayed in Fig. 14.)

Figure 14(b) presents the DMC interlayer binding curve as a function of the interlayer distance, along with the corresponding DFT ones, for which the lattice constant optimized at a given interlayer distance was used (see Fig. 14(a)). The DMC binding curve is seen to possess two minima with their energy difference being 76(1) meV per atom. Among the DFT functionals considered here, the SCAN+rVV10 (SCAN plus vdW correction)⁸⁰ is found to produce the results in the best agreement with DMC in terms of the two-minima feature and the relative energetics between them. The local minimum at a short interlayer distance and the global minimum at a longer distance turn out to have a metallic and a semiconducting band structure, respectively. The metastable metallic minimum at a

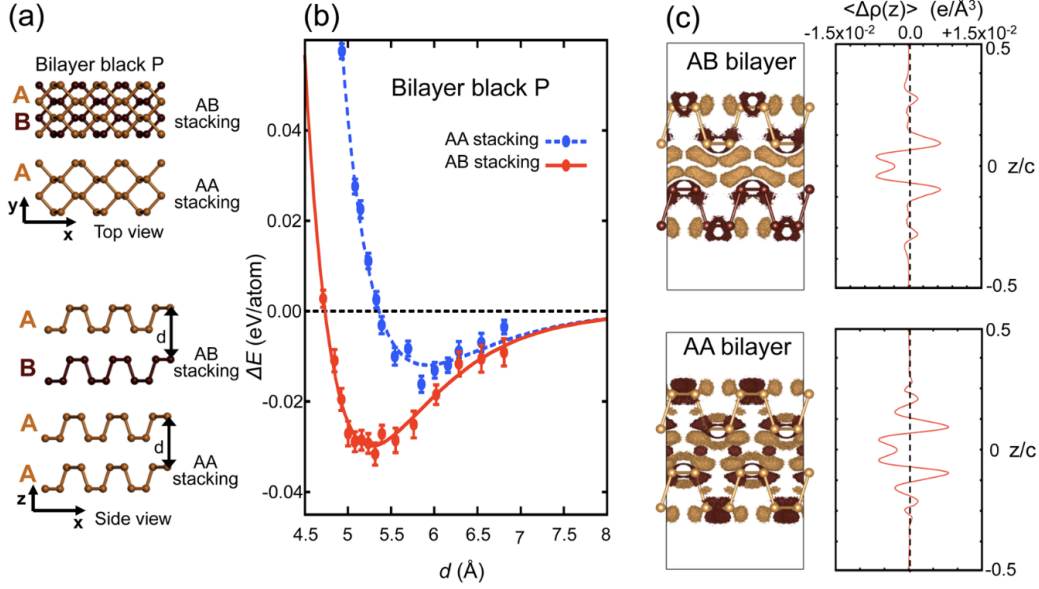


FIG. 13. DMC calculations for bonding in AA and AB stacked bilayer phosphorene. (a) AA and AB stacked bilayer geometries, (b) The relative total energy per atom ΔE as a function of the interlayer spacing d calculated with DMC. Lines that connect the data points are Morse fits that extrapolate to $\Delta E = 0$ as $d \rightarrow \infty$, (c) The difference in electron density for the AB and AA bilayers (isosurfaces and planar averages). Adapted from Ref. 259.

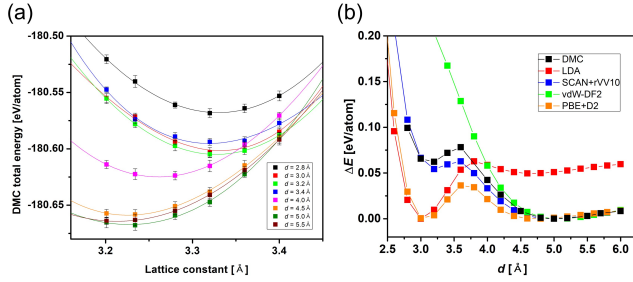


FIG. 14. (a) DMC total energy E_{bi} of a $4 \times 4 \times 1$ bilayer supercell as a function of the lattice constant for a given interlayer distance d where the solid lines represent Murnaghan fits for each d . (b) DMC relative energy $\Delta E = E_{bi} - E_{min}$, along with the corresponding DFT results computed with LDA, SCAN+rVV10, vdW-DF2, and PBE+D2 exchange-correlation functionals, as a function of the interlayer distance d where E_{min} is the minimum total energy in the respective computation. Statistical errors of DMC data in (b) are smaller than the symbol sizes (less than 0.002 eV/atom). Adapted from Ref. 263.

short interlayer distance is understood to arise from the interlayer hybridization between p_z orbitals of the highest occupied valance bands of the two monolayers as well as intralayer charge redistribution. Random phase approximation (RPA) calculations of Arcudia *et al.*²⁶⁵ also revealed two energy minima in the interlayer binding energy curve with different electronic phases for an A_1B_{-1} -stacked blue phosphorene bilayer. Contrary to the DMC results, however, the RPA study predicted that the metallic minimum at a short distance was energetically favored over the semiconducting one at a

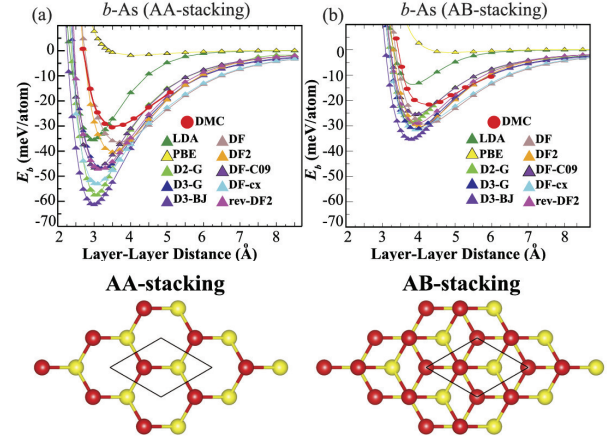


FIG. 15. The interlayer binding energy per atom calculated with DFT and DMC as a function of interlayer distance of bilayer buckled arsenene for (a) AA-stacking and (b) AB-stacking. Atomic structures of each are shown below. Adapted from Ref. 266.

longer distance. This discrepancy is understood to be due to a well-known RPA limitation in describing short-range interactions which play crucial roles in stabilizing the metallic phase. Additional information regarding this work can be found in Ref. 264.

2. Bilayer Arsenene

Similar to phosphorene, arsenene (As) is another monoelemental 2D material that displays promising electronic properties^{267–270}. Monolayer arsenene can exist in the washboard (w-As) honeycomb structure (similar to black phosphorene) and the buckled (b-As) honeycomb structure (similar to blue phosphorene). For bilayer arsenene, the ordering of energetic stability and the electronic properties have not been clearly established and various local, semilocal, vdW corrected, and hybrid functionals have been used to study bilayer arsenene^{27,271–274}. Due to the fact that this system is weakly bonded, vdW functionals are a viable method to describe the complex physics of bilayer arsenene. In order to benchmark these vdW functionals and obtain an accurate benchmark of the stability order of possible stacking configurations of bilayer arsenene, we performed DMC calculations²⁶⁶.

In this work, we performed DMC and DFT (using local, semilocal and vdW density functionals and functionals with semi-empirical vdW corrections) calculations of the binding energy and interlayer distance of w-As and b-As in AA- and AB- stacking configurations (see example in Fig. 15). Our DMC results revealed the AA-stacking to be lower in energy than the AB-stacking for b-As. We also find that the layer-layer interactions are dispersive since the energy changes by 22 % and the interlayer distance changes by 0.1 Å when going from AA- to AB-stacking. We find that for b-As, the interlayer distance changes by 0.65 Å when going from the AB- to AA-stacking, which most likely signifies a complex layer-layer interaction. When benchmarking our DMC results along with DFT, we find that vdW density functionals (i.e., DF⁷⁸) can reproduce DMC energetics, but structural parameters are better described by semi-empirically corrected functionals such as the D3-G method of Grimme⁸³. Additional information regarding this work can be found in Ref. 266.

3. Bilayer Graphene and Graphyne

Low-dimensional carbon allotropes, α -graphyne was predicted to possess weaker DFT binding energy for the bilayer structure than bilayer graphene, but has attracted a great deal of attention due to its larger honeycombs structure than graphene²⁵⁷. However, DFT studies of the bindings of graphynes failed to confirm the most stable stacking mode because of the strong dependence of vdW-corrected XC functional on computed DFT binding energy. Those uncertainties on choice of XC functional for DFT and the weak binding energy of graphynes leads to conclude that a more precise method is imperative for accurate prediction of stable stacking mode of graphynes and their binding energies.

Figure 16 shows our DMC binding energies of AB and Ab stacking mode of bilayer α -graphyne as a function of the layer spacing. Negligible difference in equilibrium binding energy between AB and Ab mode from DMC indicates the difficulty of synthesizing a pristine AB or Ab stacking α -graphyne structure. It is interesting to see both AB (23.2(2) meV per atom) and Ab modes (22.3(3) meV per atom) of graphyne

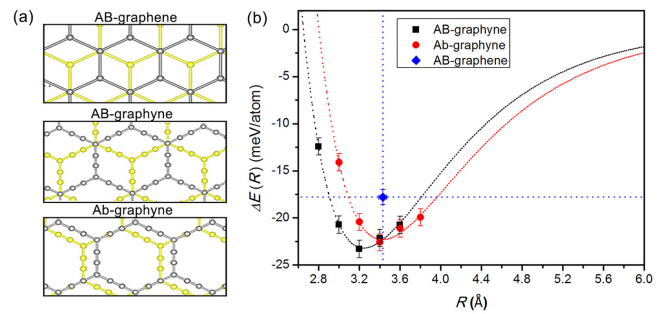


FIG. 16. (a) Stacking configurations of AB-stacked bilayer graphene and two stable modes (AB and Ab) of a bilayer α -graphyne. The yellow and gray structures represent the low and upper layer of a bilayer, respectively. (b) DMC interlayer binding energies of AB- and Ab-stacked bilayer α -graphynes as functions of an interlayer distance. The blue diamond symbol represents a DMC interlayer binding energy for an AB-bilayer graphene at an equilibrium interlayer distance reported in Ref. 256. Adapted from Ref. 257.

show larger equilibrium binding energies than AB stacking bilayer graphene (17.8(3) meV per atom), which can be understood by the existence of other interlayer binding nature than the weak vdW interaction in a sp-sp² hybridized graphyne form. Due to this difference of interlayer binding nature between sp²-bonded and sp-sp² hybridized carbon networks, it is found that vdW-corrected DFT functionals including DFT-D2⁸², vdW-DF, and rVV10 significantly underestimate the binding energy of bilayer α -graphynes while an overestimation of the binding energy was shown on the pristine sp²-bonded graphene. Among the vdW-corrected DFT functionals, binding energies computed by rVV10 functional show the closest result to corresponding DMC result, while vdW-DF provides the closest charge density distributions. This inconsistent trend indicates the importance of an accurate description for both of dispersion and density correction in vdW corrected DFT functionals, which can provide guidelines to improve vdW descriptions for the future Kohn-Sham scheme. More information can be found in Ref. 257.

In addition to our work presented in this section, Mostaani *et al.*²⁵⁶ computed the DMC binding energy of bilayer graphene to be 11.5(9) meV/atom and 17.7(9) meV/atom for AA and AB-stacking respectively and Krongchon *et al.*²⁷⁵ utilized DMC and tight binding models to accurately describe the registry-dependent potential energy and lattice corrugation of twisted bilayer graphene, a highly correlated system.

4. Bilayer and Bulk TiS₂

The family of vdW density functionals has been largely successful for a wide variety of systems, including 2D materials. Due to the success of this approach, there have been numerous improvements to the original vdW-DF functionals, where an emphasis has been placed on incorporating semi-local exchange²⁷⁷. Despite these improvements, highly accurate benchmarking calculations, such as those performed with

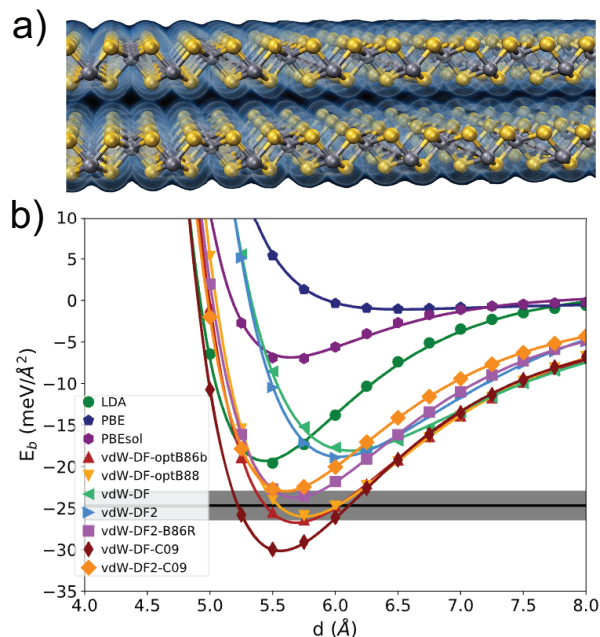


FIG. 17. (a) Atomic structure and charge density isosurfaces and (b) interlayer binding energy curve for bilayer TiS₂ calculated with a variety of DFT functionals alongside the DMC results (black line with gray region indicating the uncertainty). Adapted from Ref. 276.

DMC, are crucial in paving the way to developing a general purpose vdW density functional that can accurately reproduce fundamental properties such as the total energy and the electron density. In this specific work, we chose to benchmark the properties of bulk and bilayer TiS₂ with a variety of local, semilocal, and vdW DFT functionals against DMC²⁷⁶. TiS₂ (part of the dichalcogenide family) is a system of interest due to its potential applications as a cathode material for Li-ion batteries²⁷⁸ and because it lies within a phase transition from a narrow gap semiconductor to a semimetal, adding complexity and novelty to the noncovalent interactions²⁷⁹.

After performing these benchmarking calculations (depicted in Fig. 17), we found a close relationship between the accuracy of the interlayer distance and binding energy. We find that more recently developed vdW functionals such as vdW-DF-optB88 perform well for both properties. In terms of the response of the electron density to binding, we find that functionals such as LDA and PBEsol²⁸⁰ outperform the vdW functionals and can correctly describe the interlayer charge accumulation. vdW functionals such as vdW-DF-C09²⁷⁷, which was developed on purely theoretical grounds, performs the best in terms of simultaneously reproducing the DMC energy and electron density. This highlights the need for a theory-driven path forward to develop a fully predictive and consistent vdW functional, with highly accurate benchmarks from methods such as DMC paving the way. Additional information can be found in Ref. 276.

5. Bulk CrI₃

In this section, we revisit the CrI₃ system (discussed extensively in Section III A 2) from a different perspective. As previously mentioned, CrI₃ exhibits long-range magnetic ordering from few-layer to monolayer¹⁶. Bulk and few-layer CrI₃ possess long-range interlayer and short-range intralayer interactions. The long-range vdW interlayer (noncovalent) interactions, which are due to strongly correlated electrons occupying d orbitals of Cr, and the competing intralayer correlations make this an extremely challenging system to model with approaches such as local or semilocal DFT. Certain vdW corrections in DFT can improve the accuracy of these interlayer forces, but the results can vary drastically depending on which vdW correction is employed.

In this work, we studied the binding properties of bulk CrI₃ with DMC, with the goal of simultaneously describing the short- and long-range correlations and overcoming the shortcomings of DFT²⁸¹. For the monoclinic bulk CrI₃ structure, we calculated the interlayer separation distance to be 6.749(73) Å with DMC, which is in excellent agreement with the experimental value of 6.623 Å²⁸². We also estimated the interlayer binding energy to be between 14.3 to 17.9 meV/Å². We benchmarked several DFT functionals with and without vdW corrections against our DMC results for interlayer separation distance and binding energy (See Fig. 18) and we found that vdW-DF-optB88⁷⁹ and vdW-DF-optB86b²⁸³ are closest at reproducing our DMC values. In addition, we studied the bulk rhombohedral structure of CrI₃ and found that the rhombohedral and monoclinic are within thermal energy differences of each other, which is in agreement with experiment²⁸². We believe our DMC benchmark calculations can be useful for testing other promising current and future vdW corrected functionals. Further information of this work can be found in Ref 281.

6. Graphene-supported Pt layers

Recent experimental realization of 2D layered structures of Pt atoms above a graphene surface^{285–287} has opened an interesting avenue for exploration of their various morphologies, as well as the bonding nature of Pt-graphene complexes. In the sense that the layer formation is a consequence of a competition between non-directional metallic bondings among Pt atoms and their covalent and vdW bondings to graphene, DMC benchmarking is critical for accurate theoretical investigation of these layered systems with large degrees of freedom (including different Pt/C atomic ratios). As far as their geometries and relative energetics between different layered structures of Pt atoms are concerned, DFT results based on the SCAN+rVV10 functional are found to best agree with the corresponding DMC results.

Our DMC-benchmarked DFT calculations show that a (111)-packing structure, where each of the Pt atoms is adsorbed at a hollow site of graphene (see Fig. 19(c)), is more stable than the (100)-packing ones when forming the commensurate Pt-graphene complex at a Pt/C atomic ratio of

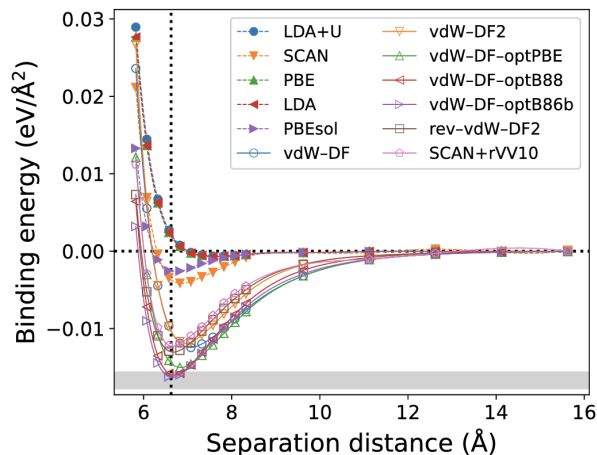


FIG. 18. The interlayer binding energy as a function of separation distance for monoclinic CrI_3 for various DFT functionals alongside DMC (gray shaded region indicates uncertainty). The vertical line indicates the experimental separation distance. Adapted from Ref. 281.

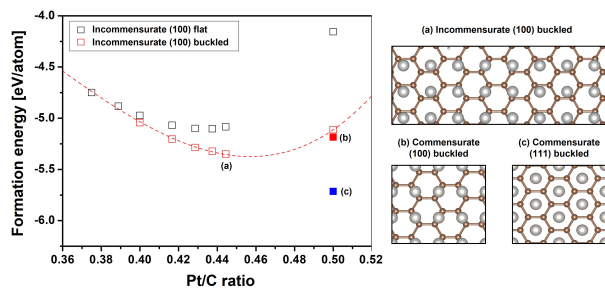


FIG. 19. DFT-SCAN+rVV10 equilibrium formation energies of various Pt monolayer on graphene, as functions of the Pt/C atomic ratio, where open black and red squares represent the formation energies of (100)-packing flat and buckled structures on pristine graphene, respectively. The solid symbols denote the equilibrium formation energies of the respective Pt layers on graphene whose lattice is allowed to relax. The red dotted lines represent third-order polynomial fits of the lower formation energies between flat and buckled structures at the respective Pt/C atomic ratio. Spin-orbit coupling was not included in these calculations. Adapted from Ref. 284.

1/2. This can be understood by a significant lattice mismatch ($>10\%$) between pristine graphene and a freestanding (100)-packing Pt layer. Energetic stability of incommensurate Pt layers with different Pt/C atomic ratios were also investigated. Figure 19 displays DFT-SCAN+rVV10 formation energies of both flat and buckled incommensurate (100)-packing Pt monolayers (see Fig. 19(a)) as functions of the Pt/C atomic ratio. The lowest energy configuration is found at the ratio of 0.457 and its formation energy is lower than the corresponding energies for buckled (100)-packing monolayer with the atomic ratio of 1/2, which is in line with recent experimental findings²⁸⁷. However, the formation energy of this optimal incommensurate structure is still higher than that of the

(111)-packing commensurate structure. Through its systematic investigation for various possible morphologies of layered Pt-on-graphene systems, this DMC-benchmarked study contributes to the expansion of a family of available metallic Pt layers. Additional information can be found in Ref. 284.

D. Cohesion and adsorption energetics

Since the successful isolation of the graphene sheet, numerous types of 2D materials have been theoretically proposed, each exhibiting intriguing electronic properties. A handful of these materials have also been synthesized. In light of this, obtaining accurate assessments of their ground-state properties, including cohesive energies and their relative differences, is of paramount importance. These assessments not only guide experimental synthesis efforts but also aid in the development of sophisticated DFT exchange-correlation functionals to deal with 2D materials. Quantitative agreement between DMC calculations and experimental results for some existing 2D materials has solidified DMC as the optimal approach for fulfilling this role among current available first-principles calculations for periodic solid systems. DMC calculations have effectively established the ground-state energetics for many proposed 2D materials whose DFT energy differences are sensitive to the choice of density functionals. It is worth noting that, in many instances, DFT tends to overestimate their cohesive energies compared to those derived from DMC calculations^{264,288–290}. This discrepancy has been attributed to various factors, including dimensional effects and the types of bondings involved. Below, we provide several examples illustrating the application of DMC calculations in investigating the cohesion and adsorption energetics of 2D materials.

1. Carbon allotropes

Graphyne is one of the proposed sp-sp² hybridized 2D carbon allotropes expected to have exotic electronic properties, such as possessing a Dirac cone, high carrier mobilities, and a larger surface area than graphene²⁸⁸. Since the successful synthesis of graphene, various sp- or sp-sp² hybridized low-dimensional carbon allotropes have been proposed via various first-principle studies. However, only γ -graphyne has been experimentally synthesized so far^{291–293}, while DFT predicted the possible existence of other stable graphyne structures. To investigate the accurate structural stability of carbon allotropes, QMC is employed on various carbon allotropes, including sp³ diamond, sp² graphene, sp-sp² hybridized graphyne, and sp-bonded carbyne chain.

In the results obtained from our DMC calculations for the cohesive energy of carbon allotropes, it is found that the estimated DMC cohesive energies for diamond and graphite are in the excellent agreement with corresponding experimental results²⁹⁴. On the other hands, the computed cohesive energy of graphynes from DMC demonstrates a monotonically decreasing trend with the increase of the ratio of sp-bonded atoms on their system. Based on the linear increase of cohe-

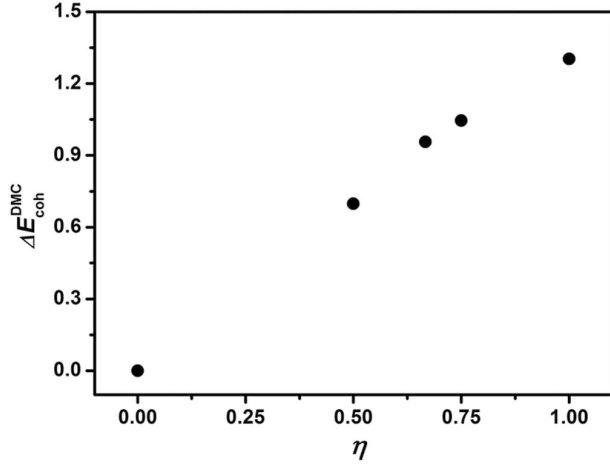


FIG. 20. The DMC cohesive energy difference between a low-dimensional carbon allotrope and graphene, $\Delta E_{coh}^{DMC} = E_{coh}^{DMC}(graphene) - E_{coh}^{DMC}(allotropes)$, as a function of the ratio of sp-bonded carbon atoms, η . The energies are in units of eV/atom. Adapted from Ref. 288.

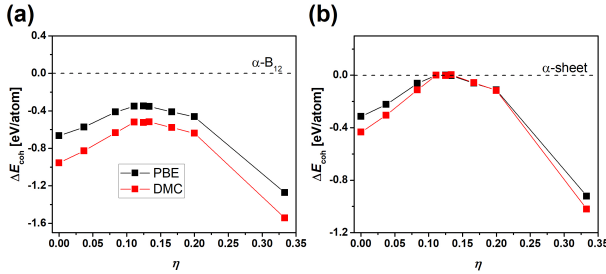


FIG. 21. DMC and PBE cohesive energies of freestanding boron sheets relative to those of (a) the α -B₁₂ solid and (b) the $\eta = \frac{1}{9}$ α -sheet, as a function of η . Statistical errors are smaller than the symbol sizes. Adapted from Ref. 290.

sive energy difference between graphene and graphynes with increasing the ratio of sp-bond η as shown in Figure 20, we expect that prediction of cohesive energy for other newly proposed graphyne structures can be achieved by utilizing computed DMC bond energies of sp-, sp²-, and sp³- bond as $N_{atom}E_{coh} = \epsilon_s N_s + \epsilon_d N_d + \epsilon_t N_t$. E_{coh} , and ϵ represent cohesive energy, and bond energies for the single bond (ϵ_s), double bond (ϵ_d), and triple bond (ϵ_t), respectively. Note that N indicates total number of the carbon atoms (N_{atoms}), the single bonds (N_s), the double bonds (N_d), and the triple bonds (N_t) per unit cell, respectively. More information regarding this work can be found in Ref. 288.

2. Boron allotropes

Although no freestanding boron monolayer has been found in nature, a 2D sheet of boron, named borophene, was reported to be synthesized on a metal surface^{22,295–298}. The

structure of borophene is characterized by a hexagonal hole density η , the ratio of the number of single-atom vacancies to the total number of atomic sites of the triangular boron sheet. With different η values, borophene structures show various combinations of triangular and hexagonal orderings from a complete triangular lattice ($\eta = 0$) to a honeycomb structure ($\eta = 1/3$). On the theoretical side, a series of DFT calculations predicted the polymorphism of energetically degenerate borophene structures in the range of $\eta = \frac{1}{9}$ and $\frac{2}{15}$ ^{299,300}. On the other hand, subsequent experiments have reported the synthesis of borophene phases only outside the polymorphic range predicted by DFT calculations^{22,295–298}, calling for more accurate and systematic investigation of borophene energetics.

Our DMC calculation for bulk α -B₁₂ yielded a cohesive energy in very good agreement with its experimental value³⁰¹, confirming its accuracy for cohesion energetics of boron allotropes. Subsequent DMC calculations for freestanding borophene structures showed the same polymorphism as predicted by DFT studies (see Fig. 21). Figure 21(a) and (b) present DMC cohesive energies of freestanding borophenes relative to those of α -B₁₂ and α -sheet borophene ($\eta = 1/9$), respectively, along with the corresponding DFT-PBE results. While PBE overestimates energetic stability of borophene against α -B₁₂ solid (see Fig. 21(a)), PBE relative energetics between different borophene structures are in quantitative agreement with the DMC results, as seen in Fig. 21(b). This justifies the use of PBE energies to investigate the relative energetics among various borophene structures formed on metal surfaces. The DMC-benchmarked PBE calculations show that as a result of the charge transfer between a metal surface and borophene, the polymorphic range can be expanded to the η values of experimentally-synthesized borophenes on top of the Ag(111) and the Au(111) surfaces. Furthermore, the PBE calculations also predicts a possible formation of bilayer borophene with $\eta = \frac{1}{12}$ on the Au(111) surface to extend a borophene family. This not only offers further insight into a mechanism of stabilizing 2D borophene structures, but also opens a possibility of borophene-based electronic devices. Additional details of this work can be found in Ref. 290.

3. Atomic/Molecular adsorption

O₂ adsorption on graphene: Capture of oxygen molecules (O₂) is important for various industrial applications since O₂ can be used to control the rate of combustion, and its rate in the atmosphere should be controlled to avoid corrosion. Graphene has been considered as a suitable substrate for efficient O₂ capture, and its adsorption energy was successfully measured experimentally using temperature-programmed terahertz emission microscopy³⁰³. However, the stable O₂ adsorption site and its preferred orientation mode on the surface of graphene has not been confirmed experimentally yet.

Our DMC study of O₂ adsorption on graphene found that the O₂ orientation mode parallel to the graphene surface is more favorable than the vertical mode. The DMC adsorption energy for two different parallel modes of A and B (see

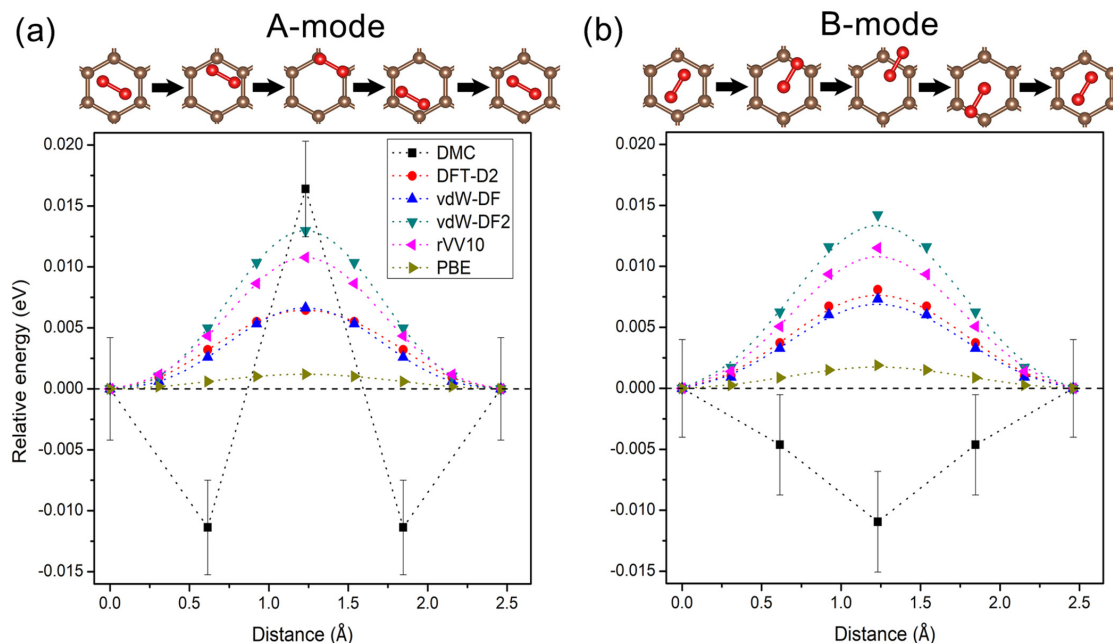


FIG. 22. DMC and DFT in-plane diffusion barrier for the hollow-bridge-hollow path for O_2 aligned in the (a) A and (b) B orientation modes. Note that the adsorption energies at a hollow site are set to be zero, and the dotted lines are guides for the eye. Adapted from Ref. 302

Fig. 22) on the hollow site of the graphene surface is estimated as $-0.130(4)$ eV and $-0.126(4)$ eV, respectively. This similar adsorption energy between A and B indicates possible free planar rotation of O_2 at the hollow site. On the other hand, the DMC in-plane diffusion barrier shows that a hollow site is not the most stable adsorption site while vdW-corrected DFT functionals show the lowest adsorption energies at the hollow sites, as seen in Fig. 22. These stable O_2 adsorptions at the bridge site of graphene can be understood by the interplay between repulsive interaction and vdW interaction. Our DMC results confirmed that the B orientation mode at the bridge site is the most stable orientation mode for O_2 adsorption, and the this mode at the bridge site is hard to accurately describe within the Kohn-Sham framework, even with vdW correction.

Pt clusters on graphene: A graphene-supported Pt cluster has received a great deal of attention because of its enhanced catalytic properties and long-term stability compared to a conventional Pt catalyst^{305–307}. Especially, a single Pt atom catalysis anchored on the graphene surface is considered highly desirable in terms of its reaction efficiency as well as the amount of Pt metal^{308,309}. Nevertheless, its experimental realization has not yet been achieved, and thus it is imperative to understand this system theoretically with thorough investigation of the interaction between graphene and a single Pt atom.

Figure 23 shows our DMC results for the singlet and triplet adsorption energy curves of a single Pt atom adsorbed on three symmetric adsorption sites (a bridge, an on-top, and a hollow site), as a function of the vertical distance from a graphene surface³⁰⁴. The bridge-site adsorption with the spin-singlet state turns out to be the most stable, which is consistent with the DFT results. However, it is found that the triplet state becomes energetically preferred over the singlet state for all

adsorption sites as the Pt-graphene distance increases, which corresponds to the spin crossing from the chemisorbed singlet state to the physisorbed triplet state. The DMC calculations also predict the presence of local minima in the triplet region. Comparison of the DMC results for the Pt-benzene, the Pt-coronene, and the Pt-graphene system revealed that additive long-range dispersion forces (induced by carbon atoms outside a carbon ring surrounding the Pt atom) are responsible for the formation of the local minima in the adsorption curves. DFT calculations do not capture this local-minimum feature, indicating the significance of many-body correlations at long distances beyond the spin crossing points. This DMC study provides a comprehensive understanding of the Pt adsorption process on a graphene surface.

H_2 adsorption on graphenylene: Using hydrogen as a renewable energy resource is a promising route for future technology. Graphenylene, a newly-proposed 2D network of sp^2 -bonded carbon atoms with large near-circular pores, is a promising membrane for separation of H_2 from gas mixtures. Its DMC cohesive energy is estimated to be $6.755(3)$ eV per atom³¹⁰, which is smaller only by ≈ 10 meV per atom than the corresponding energy of γ -graphyne, the most stable structure in a graphyne family. An experimental report of its successful synthesis is understood to reflect this DMC result. DMC calculations are also performed to estimate the adsorption energies of different gas molecules, including H_2 , on graphenylene, from which the H_2 separation capability of a graphenylene membrane against other gas molecules are estimated.

Figure 24(a) presents our DMC adsorption energy of a H_2 molecule as a function of the adsorption distance (the vertical distance from a pore center), which was computed for a $3 \times 3 \times 1$ supercell. The equilibrium adsorption distance is

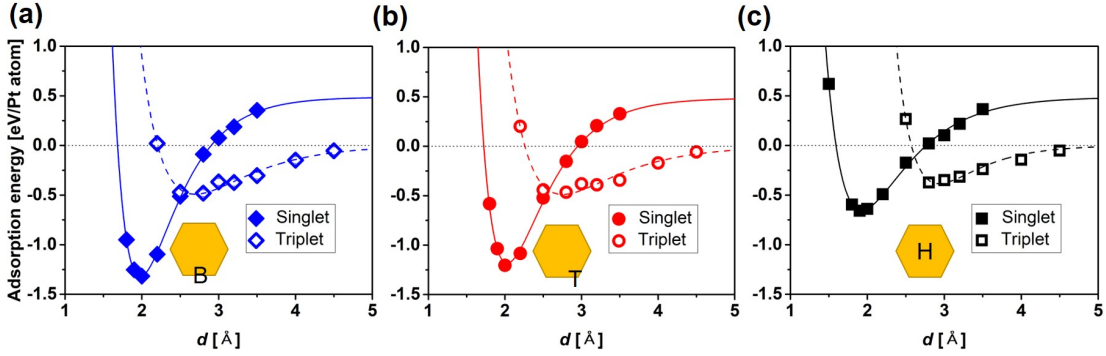


FIG. 23. DMC adsorption energy curves of a single Pt atom adsorbed at three different sites of (a) a bridge, (b) an on-top and (c) a hollow site, as a function of the vertical distance from a graphene surface. Here, B, T and H in the insets denote a bridge, an on-top and a hollow adsorption site, respectively. The singlet data is represented by solid symbols while the triplet ones are denoted by open symbols. The solid and the dotted lines represent the Morse potential fits of spin singlet and triplet adsorption energies, respectively. Adapted from Ref. 304.

determined through the Morse potential fit of the DMC adsorption energies (see the red dotted line in the figure), which produced the equilibrium distances of 1.97(4) Å for H_2 . The same procedure results in the DMC equilibrium distances of 2.73(3) Å and 2.73(4) Å for N_2 and CO molecules, respectively. After establishing the equilibrium adsorption distances for these molecules, DMC calculations are performed to compute their adsorption energies at both in-plane and equilibrium adsorption distances. Figure 24(b) shows the DMC total energies of the H_2 -graphenylene complex computed for three different supercell sizes, where the horizontal axis represents the inverse of the number of electrons in a supercell. The adsorption energies of H_2 are estimated from the total energies extrapolated to the thermodynamic limit ($N \rightarrow \infty$). The difference between in-plane and equilibrium adsorption energies determines the diffusion barrier of a gas molecule passing through a graphenylene membrane, whose DMC values are estimated to 0.19(2) eV, 0.87(5) eV, and 0.79(2) eV for H_2 , N_2 , and CO, respectively. The large difference in diffusion barrier between H_2 and other molecules results in extremely high values for hydrogen selectivity against a gas of N_2 ($\approx 10^{11}$) or CO ($\approx 10^{10}$)³¹⁰. This suggests that an application of graphenylene as a high performing hydrogen separator is promising.

Atomic H adsorption on graphene: The chemisorption of atomic hydrogen on graphene is another system of interest, due to the tunability of electronic (opening up of the band gap³¹¹) and magnetic (inducing an extended magnetic moment in a graphene sheet^{312,313}) properties when hydrogen atoms are chemisorbed. In addition, graphene and graphitic surfaces can be utilized for hydrogen storage and energy applications³¹⁴. In addition to the interesting applications, the lack of experimental benchmarks (i.e., binding energy) for H chemisorbed on graphene and the variability of standard DFT approaches for atomic adsorption on 2D surfaces makes this an excellent system to apply DMC techniques.

In this work, we performed DFT and DMC calculations to obtain the binding energy of a single H atom chemisorbed on the surface of a graphene sheet³¹⁵. With DMC, we find this binding energy to be $-691 \text{ meV} \pm 19 \text{ meV}$. We find that

PBE (plane-wave) overestimates the binding energy by approximately 20 % compared to DMC. We also find that PBE0 results in a binding energy close to PBE but HSE yields a binding energy in closer agreement to DMC (-743 meV). We also find significant differences between the DMC and PBE charge densities of graphene and H chemisorbed on graphene (see Fig. 25). More details of this work can be found in Ref. 315. In addition to our work reported in this section that focuses on atomic and molecular adsorption on monolayer surfaces, there have been efforts to utilize DMC to accurately calculate the point defect formation energy in 2D materials³¹⁶. Thomas *et al.*³¹⁶ performed DMC calculations for monovacancies, Stone-Wales defects, and silicon substitutions in monolayer graphene and found substantial disagreements with DFT for defect formation energy (up to 1 eV).

IV. CONCLUSION

We have demonstrated the successes of applying the many-body DMC approach to a wide variety of 2D material systems. This review article provides detailed summaries of several instances where DMC can improve the prediction of magnetic, electronic (including excitonic and topological) properties and accurately capture the interlayer interactions and the energetics of cohesion and adsorption. The results reported in this review demonstrate how accuracy beyond standard DFT can realistically be achieved using many-body electronic structure methods such as DMC. We hope that by showcasing the recent advancements in the field of Quantum Monte Carlo methods being applied to 2D materials, other researchers will be motivated to employ these highly accurate techniques for future work.

V. COMPETING INTERESTS

The authors have no conflicts to disclose.

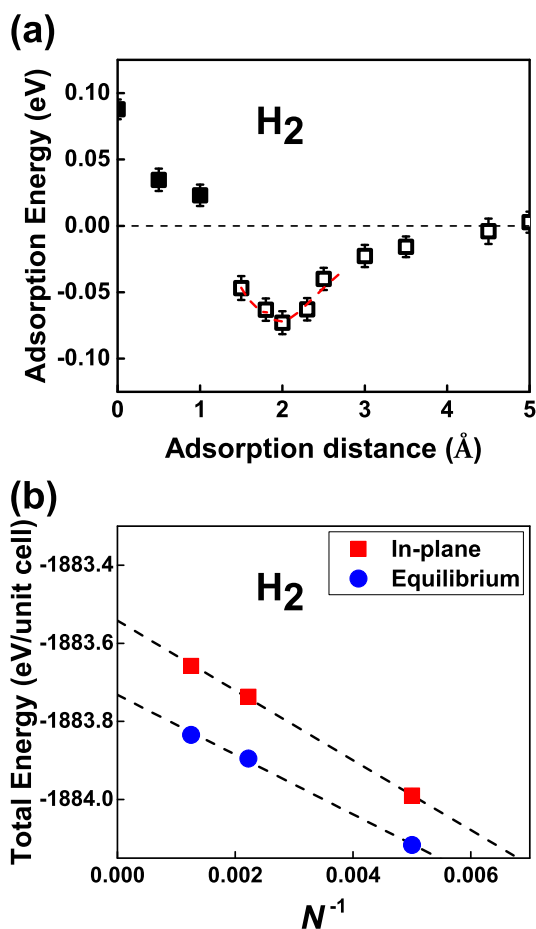


FIG. 24. (a) DMC adsorption energies of a H_2 molecule on graphenylene (GPNL) as a function of the adsorption distance, computed for the $3 \times 3 \times 1$ supercell. Here, the adsorption energies for the H_2 orientation modes favored at specific adsorption distances are presented with solid and open symbols corresponding to the V- (vertical to the membrane) and P-modes (parallel to the membrane). The red dashed line represents a Morse potential fit. (b) Twist-averaged DMC supercell energies of a H_2 -GPNL complex, with the molecule adsorbed at the in-plane or the equilibrium adsorption site, as a function of N^{-1} where N is the number of electrons in a supercell. Statistical errors of the DMC data are smaller than their symbol sizes. The dashed lines represent linear regression fits. Adapted from Ref. 310.

VI. DATA AVAILABILITY

Data sharing is not applicable to this article as no new data were created or analyzed in this study.

VII. NOTES

Please note certain equipment, instruments, software, or materials are identified in this paper in order to specify the experimental procedure adequately. Such identification is not intended to imply the recommendation or endorsement of any product or service by NIST, nor is it intended to imply that

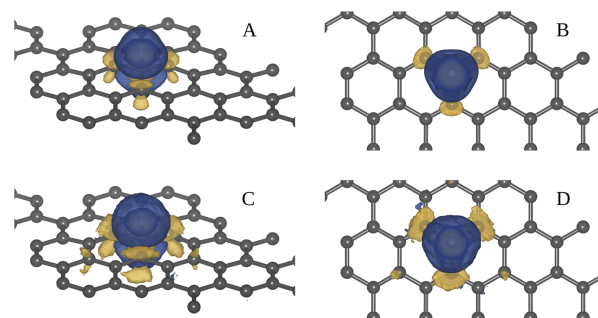


FIG. 25. The change in electron density associated with the adsorption of H on a distorted graphene sheet. (a) and (b) display the PBE density from different perspectives and (c) and (d) display the DMC density from different perspectives. Gold indicates a gain of electron density while blue indicates a loss. Adapted from Ref. 315.

the materials or equipment identified are necessarily the best available for the purpose.

VIII. ACKNOWLEDGMENTS

D.W. acknowledges the National Institute of Standards and Technology for funding and support. J.A., A.B., P.R.C.K., J.T.K., L.M., B.R. and H.S. were supported by the U.S. Department of Energy, Office of Science, Basic Energy Sciences, Materials Sciences and Engineering Division, as part of the Computational Materials Sciences Program and the Center for Predictive Simulation of Functional Materials. L.M. also received support (excitonic effects in 2D) from U.S. National Science Foundation grant DMR-2316007. Y.K. was supported by the Basic Science Research Program (2018R1D1A1B07042443) through the National Research Foundation of Korea funded by the Ministry of Education. I.S. acknowledges support by APVV-21-0272, VEGA-2/0131/23 and by the H2020 TREX GA 952165 projects. K.S. and F.A.R. was supported by the U.S. Department of Energy, Office of Science, Basic Energy Sciences, Materials Sciences and Engineering Division. C.A. acknowledges funding from the National Science Foundation (NSF) under grant number NSF DMR-2213398 and U.S. Department of Energy (DOE) under grant number DE-SC0024236.

REFERENCES

- ¹K. S. Novoselov, D. Jiang, F. Schedin, T. J. Booth, V. V. Khotkevich, S. V. Morozov, and A. K. Geim, "Two-dimensional atomic crystals," *Proceedings of the National Academy of Sciences* **102**, 10451–10453 (2005), <https://www.pnas.org/doi/pdf/10.1073/pnas.0502848102>.
- ²K. S. Novoselov, A. K. Geim, S. V. Morozov, D. Jiang, Y. Zhang, S. V. Dubonos, I. V. Grigorieva, and A. A. Firsov, "Electric field effect in atomically thin carbon films," *Science* **306**, 666–669 (2004), <https://www.science.org/doi/pdf/10.1126/science.1102896>.
- ³A. K. Geim and K. S. Novoselov, "The rise of graphene," *Nature Materials* **6**, 183–191 (2007).

- ⁴K. F. Mak, C. Lee, J. Hone, J. Shan, and T. F. Heinz, "Atomically thin mos_2 : A new direct-gap semiconductor," *Phys. Rev. Lett.* **105**, 136805 (2010).
- ⁵B. Radisavljevic, A. Radenovic, J. Brivio, V. Giacometti, and A. Kis, "Single-layer mos_2 transistors," *Nature Nanotechnology* **6**, 147–150 (2011).
- ⁶A. Splendiani, L. Sun, Y. Zhang, T. Li, J. Kim, C.-Y. Chim, G. Galli, and F. Wang, "Emerging photoluminescence in monolayer mos_2 ," *Nano Letters* **10**, 1271–1275 (2010).
- ⁷M. Bernardi, M. Palummo, and J. C. Grossman, "Extraordinary sunlight absorption and one nanometer thick photovoltaics using two-dimensional monolayer materials," *Nano Letters* **13**, 3664–3670 (2013).
- ⁸M. Bernardi, C. Ataca, M. Palummo, and J. C. Grossman, *Nanophotonics* **6**, 479–493 (2017).
- ⁹T. Mueller and E. Malic, "Exciton physics and device application of two-dimensional transition metal dichalcogenide semiconductors," *npj 2D Materials and Applications* **2**, 29 (2018).
- ¹⁰D. G. Papageorgiou, I. A. Kinloch, and R. J. Young, "Mechanical properties of graphene and graphene-based nanocomposites," *Progress in Materials Science* **90**, 75–127 (2017).
- ¹¹J.-H. Lee, Y. Choi, S.-H. Do, B. H. Kim, M.-J. Seong, and K.-Y. Choi, "Multiple spin-orbit excitons in α - rucl_3 from bulk to atomically thin layers," *npj Quantum Materials* **6**, 43 (2021).
- ¹²K. Choudhary, K. F. Garrity, J. Jiang, R. Pachter, and F. Tavazza, "Computational search for magnetic and non-magnetic 2d topological materials using unified spin-orbit spillage screening," *npj Computational Materials* **6**, 49 (2020).
- ¹³S. Tang, C. Zhang, D. Wong, Z. Pedramrazi, H.-Z. Tsai, C. Jia, B. Moritz, M. Claassen, H. Ryu, S. Kahn, J. Jiang, H. Yan, M. Hashimoto, D. Lu, R. G. Moore, C.-C. Hwang, C. Hwang, Z. Hussain, Y. Chen, M. M. Ugeda, Z. Liu, X. Xie, T. P. Devereaux, M. F. Crommie, S.-K. Mo, and Z.-X. Shen, "Quantum spin hall state in monolayer $1\text{t}'\text{-wte}_2$," *Nature Physics* **13**, 683–687 (2017).
- ¹⁴Y. Saito, T. Nojima, and Y. Iwasa, "Highly crystalline 2d superconductors," *Nature Reviews Materials* **2**, 16094 (2016).
- ¹⁵D. Wines, K. Choudhary, A. J. Biacchi, K. F. Garrity, and F. Tavazza, "High-throughput dft-based discovery of next generation two-dimensional (2d) superconductors," *Nano Letters* **23**, 969–978 (2023).
- ¹⁶B. Huang, G. Clark, E. Navarro-Moratalla, D. R. Klein, R. Cheng, K. L. Seyler, D. Zhong, E. Schmidgall, M. A. McGuire, D. H. Cobden, W. Yao, D. Xiao, P. Jarillo-Herrero, and X. Xu, "Layer-dependent ferromagnetism in a van der waals crystal down to the monolayer limit," *Nature* **546**, 270–273 (2017).
- ¹⁷M. C. Lemme, D. Akinwande, C. Huyghebaert, and C. Stampfer, "2d materials for future heterogeneous electronics," *Nature Communications* **13**, 1392 (2022).
- ¹⁸N. R. Glavin, R. Rao, V. Varshney, E. Bianco, A. Apte, A. Roy, E. Ringe, and P. M. Ajayan, "Emerging applications of elemental 2d materials," *Advanced Materials* **32**, 1904302 (2020), <https://onlinelibrary.wiley.com/doi/pdf/10.1002/adma.201904302>.
- ¹⁹M. E. Dávila, L. Xian, S. Cahangirov, A. Rubio, and G. L. Lay, "Germanene: a novel two-dimensional germanium allotrope akin to graphene and silicene," *New Journal of Physics* **16**, 095002 (2014).
- ²⁰A. Acun, L. Zhang, P. Bampoulis, M. Farmanbar, A. van Houselt, A. N. Rudenko, M. Lingenfelder, G. Brocks, B. Poelsema, M. I. Katsnelson, and H. J. W. Zandvliet, "Germanene: the germanium analogue of graphene," *Journal of Physics: Condensed Matter* **27**, 443002 (2015).
- ²¹I. Boustani, "New quasi-planar surfaces of bare boron," *Surface Science* **370**, 355–363 (1997).
- ²²B. Feng, J. Zhang, Q. Zhong, W. Li, S. Li, H. Li, P. Cheng, S. Meng, L. Chen, and K. Wu, "Experimental realization of two-dimensional boron sheets," *Nature Chemistry* **8**, 563–568 (2016).
- ²³Z. Zhang, Y. Yang, G. Gao, and B. I. Yakobson, "Two-dimensional boron monolayers mediated by metal substrates," *Angewandte Chemie International Edition* **54**, 13022–13026 (2015), <https://onlinelibrary.wiley.com/doi/pdf/10.1002/anie.201505425>.
- ²⁴A. J. Mannix, X.-F. Zhou, B. Kiraly, J. D. Wood, D. Alducin, B. D. Myers, X. Liu, B. L. Fisher, U. Santiago, J. R. Guest, M. J. Yacaman, A. Ponce, A. R. Oganov, M. C. Hersam, and N. P. Guisinger, "Synthesis of borophenes: Anisotropic, two-dimensional boron polymorphs," *Science* **350**, 1513–1516 (2015), <https://www.science.org/doi/pdf/10.1126/science.aad1080>.
- ²⁵M. Xu, T. Liang, M. Shi, and H. Chen, "Graphene-like two-dimensional materials," *Chemical Reviews* **113**, 3766–3798 (2013).
- ²⁶S. Cahangirov, M. Topsakal, E. Aktürk, H. Şahin, and S. Ciraci, "Two- and one-dimensional honeycomb structures of silicon and germanium," *Phys. Rev. Lett.* **102**, 236804 (2009).
- ²⁷S. Zhang, Z. Yan, Y. Li, Z. Chen, and H. Zeng, "Atomically thin arsenene and antimonene: Semimetal–semiconductor and indirect–direct band-gap transitions," *Angewandte Chemie International Edition* **54**, 3112–3115 (2015), <https://onlinelibrary.wiley.com/doi/pdf/10.1002/anie.201411246>.
- ²⁸J. Ji, X. Song, J. Liu, Z. Yan, C. Huo, S. Zhang, M. Su, L. Liao, W. Wang, Z. Ni, Y. Hao, and H. Zeng, "Two-dimensional antimonene single crystals grown by van der waals epitaxy," *Nature Communications* **7**, 13352 (2016).
- ²⁹P. Ares, F. Aguilar-Galindo, D. Rodríguez-San-Miguel, D. A. Aldave, S. Díaz-Tendero, M. Alcamí, F. Martín, J. Gómez-Herrero, and F. Zamora, "Mechanical isolation of highly stable antimonene under ambient conditions," *Advanced Materials* **28**, 6332–6336 (2016), <https://onlinelibrary.wiley.com/doi/pdf/10.1002/adma.201602128>.
- ³⁰L. Li, Y. Yu, G. J. Ye, Q. Ge, X. Ou, H. Wu, D. Feng, X. H. Chen, and Y. Zhang, "Black phosphorus field-effect transistors," *Nature Nanotechnology* **9**, 372–377 (2014).
- ³¹H. Liu, A. T. Neal, Z. Zhu, Z. Luo, X. Xu, D. Tománek, and P. D. Ye, "Phosphorene: An unexplored 2d semiconductor with a high hole mobility," *ACS Nano* **8**, 4033–4041 (2014).
- ³²S. P. Koenig, R. A. Doganov, H. Schmidt, A. H. Castro Neto, and B. Özyilmaz, "Electric field effect in ultrathin black phosphorus," *Applied Physics Letters* **104**, 103106 (2014), https://pubs.aip.org/aip/apl/article-pdf/doi/10.1063/1.4868132/14292271/103106_1_online.pdf.
- ³³Z. Zhu, X. Cai, S. Yi, J. Chen, Y. Dai, C. Niu, Z. Guo, M. Xie, F. Liu, J.-H. Cho, Y. Jia, and Z. Zhang, "Multivalency-driven formation of te-based monolayer materials: A combined first-principles and experimental study," *Phys. Rev. Lett.* **119**, 106101 (2017).
- ³⁴Y. Wang, G. Qiu, R. Wang, S. Huang, Q. Wang, Y. Liu, Y. Du, W. A. Goddard, M. J. Kim, X. Xu, P. D. Ye, and W. Wu, "Field-effect transistors made from solution-grown two-dimensional tellurene," *Nature Electronics* **1**, 228–236 (2018).
- ³⁵C. Ataca, H. Şahin, and S. Ciraci, "Stable, single-layer MX_2 transition-metal oxides and dichalcogenides in a honeycomb-like structure," *The Journal of Physical Chemistry C* **116**, 8983–8999 (2012).
- ³⁶Y.-H. Chang, W. Zhang, Y. Zhu, Y. Han, J. Pu, J.-K. Chang, W.-T. Hsu, J.-K. Huang, C.-L. Hsu, M.-H. Chiu, T. Takenobu, H. Li, C.-I. Wu, W.-H. Chang, A. T. S. Wee, and L.-J. Li, "Monolayer mose_2 grown by chemical vapor deposition for fast photodetection," *ACS Nano* **8**, 8582–8590 (2014).
- ³⁷P. Rivera, J. R. Schaibley, A. M. Jones, J. S. Ross, S. Wu, G. Aivazian, P. Klement, K. Seyler, G. Clark, N. J. Ghimire, J. Yan, D. G. Mandrus, W. Yao, and X. Xu, "Observation of long-lived interlayer excitons in monolayer mose_2 - wse_2 heterostructures," *Nature Communications* **6**, 6242 (2015).
- ³⁸W.-T. Hsu, L.-S. Lu, D. Wang, J.-K. Huang, M.-Y. Li, T.-R. Chang, Y.-C. Chou, Z.-Y. Juang, H.-T. Jeng, L.-J. Li, and W.-H. Chang, "Evidence of indirect gap in monolayer wse_2 ," *Nature Communications* **8**, 929 (2017).
- ³⁹B. Liu, M. Fathi, L. Chen, A. Abbas, Y. Ma, and C. Zhou, "Chemical vapor deposition growth of monolayer wse_2 with tunable device characteristics and growth mechanism study," *ACS Nano* **9**, 6119–6127 (2015).
- ⁴⁰Z. Fei, T. Palomaki, S. Wu, W. Zhao, X. Cai, B. Sun, P. Nguyen, J. Finney, X. Xu, and D. H. Cobden, "Edge conduction in monolayer wte_2 ," *Nature Physics* **13**, 677–682 (2017).
- ⁴¹H. Cai, E. Soignard, C. Ataca, B. Chen, C. Ko, T. Aoki, A. Pant, X. Meng, S. Yang, J. Grossman, F. D. Ogletree, and S. Tongay, "Band engineering by controlling vdW epitaxy growth mode in 2D gallium chalcogenides," *Advanced Materials* **28**, 7375–7382 (2016), <https://onlinelibrary.wiley.com/doi/pdf/10.1002/adma.201601184>.
- ⁴²C. Wang, S. Yang, H. Cai, C. Ataca, H. Chen, X. Zhang, J. Xu, B. Chen, K. Wu, H. Zhang, L. Liu, J. Li, J. C. Grossman, S. Tongay, and Q. Liu, "Enhancing light emission efficiency without color change in post-transition metal chalcogenides," *Nanoscale* **8**, 5820–5825 (2016).
- ⁴³Z. Ben Aziza, D. Pierucci, H. Henck, M. G. Silly, C. David, M. Yoon, F. Sirotti, K. Xiao, M. Eddrief, J.-C. Girard, and A. Ouerghi, "Tunable

- quasiparticle band gap in few-layer GaSe/graphene van der waals heterostructures,” *Phys. Rev. B* **96**, 035407 (2017).
- ⁴⁴J. Susoma, J. Lahtinen, M. Kim, J. Riikonen, and H. Lipsanen, “Crystal quality of two-dimensional gallium telluride and gallium selenide using raman fingerprint,” *AIP Advances* **7**, 015014 (2017).
- ⁴⁵C. S. Jung, F. Shojaei, K. Park, J. Y. Oh, H. S. Im, D. M. Jang, J. Park, and H. S. Kang, “Red-to-ultraviolet emission tuning of two-dimensional gallium sulfide/selenide,” *ACS Nano* **9**, 9585–9593 (2015).
- ⁴⁶B. Chitara and A. Ya’akobovitz, “Elastic properties and breaking strengths of GaS, GaSe and GaTe nanosheets,” *Nanoscale* **10**, 13022–13027 (2018).
- ⁴⁷X. Li, M.-W. Lin, A. A. Puzdov, J. C. Idrobo, C. Ma, M. Chi, M. Yoon, C. M. Rouleau, I. I. Kravchenko, D. B. Geohegan, and K. Xiao, “Controlled vapor phase growth of single crystalline, two-dimensional GaSe crystals with high photoresponse,” *Scientific Reports* **4**, 5497 (2014).
- ⁴⁸M. Rahaman, M. Bejani, G. Salvan, S. A. Lopez-Rivera, O. Pulci, F. Bechstedt, and D. R. T. Zahn, “Vibrational properties of GaSe: a layer dependent study from experiments to theory,” *Semiconductor Science and Technology* **33**, 125008 (2018).
- ⁴⁹M. Rahaman, R. D. Rodriguez, M. Monecke, S. A. Lopez-Rivera, and D. R. T. Zahn, “GaSe oxidation in air: from bulk to monolayers,” *Semiconductor Science and Technology* **32**, 105004 (2017).
- ⁵⁰H. Wang, G. Qin, J. Yang, Z. Qin, Y. Yao, Q. Wang, and M. Hu, “First-principles study of electronic, optical and thermal transport properties of group III-VI monolayer MX (M=Ga, In; X=S, Se),” *Journal of Applied Physics* **125**, 245104 (2019).
- ⁵¹H. Zhao, Y. Mao, X. Mao, X. Shi, C. Xu, C. Wang, S. Zhang, and D. Zhou, “Band structure and photoelectric characterization of gese monolayers,” *Advanced Functional Materials* **28**, 1704855 (2018), <https://onlinelibrary.wiley.com/doi/pdf/10.1002/adfm.201704855>.
- ⁵²Y. Hu, S. Zhang, S. Sun, M. Xie, B. Cai, and H. Zeng, “GeSe monolayer semiconductor with tunable direct band gap and small carrier effective mass,” *Applied Physics Letters* **107**, 122107 (2015), https://pubs.aip.org/aip/apl/article-pdf/doi/10.1063/1.4931459/13144120/122107_1_online.pdf.
- ⁵³A. Politano, D. Campi, M. Cattelan, I. Ben Amara, S. Jaziri, A. Mazzotti, A. Barinov, B. Gürbulak, S. Duman, S. Agnoli, L. S. Caputi, G. Granozzi, and A. Cupolillo, “Indium selenide: an insight into electronic band structure and surface excitations,” *Scientific Reports* **7**, 3445 (2017).
- ⁵⁴J. Zhou, J. Shi, Q. Zeng, Y. Chen, L. Niu, F. Liu, T. Yu, K. Suenaga, X. Liu, J. Lin, and Z. Liu, “Inse monolayer: synthesis, structure and ultrahigh second-harmonic generation,” *2D Materials* **5**, 025019 (2018).
- ⁵⁵B. Anasori, Y. Xie, M. Beidaghi, J. Lu, B. C. Hosler, L. Hultman, P. R. C. Kent, Y. Gogotsi, and M. W. Barsoum, “Two-dimensional, ordered, double transition metals carbides (mxenes),” *ACS Nano* **9**, 9507–9516 (2015).
- ⁵⁶Y. Xie, M. Naguib, V. N. Mochalin, M. W. Barsoum, Y. Gogotsi, X. Yu, K.-W. Nam, X.-Q. Yang, A. I. Kolesnikov, and P. R. C. Kent, “Role of surface structure on li-ion energy storage capacity of two-dimensional transition-metal carbides,” *Journal of the American Chemical Society* **136**, 6385–6394 (2014).
- ⁵⁷G. Gao, G. Ding, J. Li, K. Yao, M. Wu, and M. Qian, “Monolayer mxenes: promising half-metals and spin gapless semiconductors,” *Nanoscale* **8**, 8986–8994 (2016).
- ⁵⁸Z. Zhang, J. Shang, C. Jiang, A. Rasmitha, W. Gao, and T. Yu, “Direct photoluminescence probing of ferromagnetism in monolayer two-dimensional crbr₃,” *Nano Letters*, *Nano Letters* **19**, 3138–3142 (2019).
- ⁵⁹Q. Song, C. A. Occhialini, E. Ergeçen, B. Ilyas, D. Amoroso, P. Barone, J. Kapeghian, K. Watanabe, T. Taniguchi, A. S. Botana, S. Picozzi, N. Gedik, and R. Comin, “Evidence for a single-layer van der waals multiferroic,” *Nature* **602**, 601–605 (2022).
- ⁶⁰P. Hohenberg and W. Kohn, “Inhomogeneous electron gas,” *Phys. Rev.* **136**, B864–B871 (1964).
- ⁶¹W. Kohn and L. J. Sham, “Self-consistent equations including exchange and correlation effects,” *Phys. Rev.* **140**, A1133–A1138 (1965).
- ⁶²J. P. Perdew and A. Zunger, “Self-interaction correction to density-functional approximations for many-electron systems,” *Phys. Rev. B* **23**, 5048–5079 (1981).
- ⁶³D. M. Ceperley and B. J. Alder, “Ground state of the electron gas by a stochastic method,” *Phys. Rev. Lett.* **45**, 566–569 (1980).
- ⁶⁴J. P. Perdew, K. Burke, and M. Ernzerhof, “Generalized gradient approximation made simple,” *Phys. Rev. Lett.* **77**, 3865–3868 (1996).
- ⁶⁵J. P. Perdew, J. A. Chevary, S. H. Vosko, K. A. Jackson, M. R. Pederson, D. J. Singh, and C. Fiolhais, “Atoms, molecules, solids, and surfaces: Applications of the generalized gradient approximation for exchange and correlation,” *Phys. Rev. B* **46**, 6671–6687 (1992).
- ⁶⁶J. Sun, A. Ruzsinszky, and J. P. Perdew, “Strongly constrained and appropriately normed semilocal density functional,” *Phys. Rev. Lett.* **115**, 036402 (2015).
- ⁶⁷J. W. Furness, A. D. Kaplan, J. Ning, J. P. Perdew, and J. Sun, “Accurate and numerically efficient r2scan meta-generalized gradient approximation,” *The Journal of Physical Chemistry Letters* **11**, 8208–8215 (2020).
- ⁶⁸J. Sun, M. Marsman, G. I. Csonka, A. Ruzsinszky, P. Hao, Y.-S. Kim, G. Kresse, and J. P. Perdew, “Self-consistent meta-generalized gradient approximation within the projector-augmented-wave method,” *Phys. Rev. B* **84**, 035117 (2011).
- ⁶⁹A. D. Becke and E. R. Johnson, “A simple effective potential for exchange,” *The Journal of Chemical Physics* **124**, 221101 (2006), https://pubs.aip.org/aip/jcp/article-pdf/doi/10.1063/1.2213970/15385734/221101_1_online.pdf.
- ⁷⁰F. Tran and P. Blaha, “Accurate band gaps of semiconductors and insulators with a semilocal exchange-correlation potential,” *Phys. Rev. Lett.* **102**, 226401 (2009).
- ⁷¹A. V. Kruckau, O. A. Vydrov, A. F. Izmaylov, and G. E. Scuseria, “Influence of the exchange screening parameter on the performance of screened hybrid functionals,” *The Journal of Chemical Physics* **125**, 224106 (2006), https://pubs.aip.org/aip/jcp/article-pdf/doi/10.1063/1.2404663/13263224/224106_1_online.pdf.
- ⁷²P. J. Stephens, F. J. Devlin, C. F. Chabalowski, and M. J. Frisch, “Ab initio calculation of vibrational absorption and circular dichroism spectra using density functional force fields,” *The Journal of Physical Chemistry* **98**, 11623–11627 (1994).
- ⁷³A. D. Becke, “Density-functional thermochemistry. III. The role of exact exchange,” *The Journal of Chemical Physics* **98**, 5648–5652 (1993), https://pubs.aip.org/aip/jcp/article-pdf/98/7/5648/11091662/5648_1_online.pdf.
- ⁷⁴J. P. Perdew, M. Ernzerhof, and K. Burke, “Rationale for mixing exact exchange with density functional approximations,” *The Journal of Chemical Physics* **105**, 9982–9985 (1996), https://pubs.aip.org/aip/jcp/article-pdf/105/22/9982/9439202/9982_1_online.pdf.
- ⁷⁵C. Adamo and V. Barone, “Toward reliable density functional methods without adjustable parameters: The PBE0 model,” *The Journal of Chemical Physics* **110**, 6158–6170 (1999), https://pubs.aip.org/aip/jcp/article-pdf/110/13/6158/10797469/6158_1_online.pdf.
- ⁷⁶C. Lee, W. Yang, and R. G. Parr, “Development of the colle-salvetti correlation-energy formula into a functional of the electron density,” *Phys. Rev. B* **37**, 785–789 (1988).
- ⁷⁷S. H. Vosko, L. Wilk, and M. Nusair, “Accurate spin-dependent electron liquid correlation energies for local spin density calculations: a critical analysis,” *Canadian Journal of Physics* **58**, 1200–1211 (1980).
- ⁷⁸M. Dion, H. Rydberg, E. Schröder, D. C. Langreth, and B. I. Lundqvist, “Van der waals density functional for general geometries,” *Phys. Rev. Lett.* **92**, 246401 (2004).
- ⁷⁹J. Klimeš, D. R. Bowler, and A. Michaelides, “Chemical accuracy for the van der waals density functional,” *Journal of Physics: Condensed Matter* **22**, 022201 (2009).
- ⁸⁰H. Peng, Z.-H. Yang, J. P. Perdew, and J. Sun, “Versatile van der waals density functional based on a meta-generalized gradient approximation,” *Phys. Rev. X* **6**, 041005 (2016).
- ⁸¹K. Lee, E. D. Murray, L. Kong, B. I. Lundqvist, and D. C. Langreth, “Higher-accuracy van der waals density functional,” *Phys. Rev. B* **82**, 081101 (2010).
- ⁸²S. Grimme, “Semiempirical gga-type density functional constructed with a long-range dispersion correction,” *Journal of Computational Chemistry* **27**, 1787–1799 (2006), <https://onlinelibrary.wiley.com/doi/pdf/10.1002/jcc.20495>.
- ⁸³S. Grimme, J. Antony, S. Ehrlich, and H. Krieg, “A consistent and accurate ab initio parametrization of density functional dispersion correction (DFT-D) for the 94 elements H-Pu,” *The Journal of Chemical Physics* **132**, 154104 (2010), https://pubs.aip.org/aip/jcp/article-pdf/doi/10.1063/1.3382344/15684000/154104_1_online.pdf.

- ⁸⁴S. Grimme, S. Ehrlich, and L. Goerigk, "Effect of the damping function in dispersion corrected density functional theory," *Journal of Computational Chemistry* **32**, 1456–1465 (2011), <https://onlinelibrary.wiley.com/doi/pdf/10.1002/jcc.21759>.
- ⁸⁵A. Tkatchenko and M. Scheffler, "Accurate molecular van der waals interactions from ground-state electron density and free-atom reference data," *Phys. Rev. Lett.* **102**, 073005 (2009).
- ⁸⁶K. Choudhary, G. Cheon, E. Reed, and F. Tavazza, "Elastic properties of bulk and low-dimensional materials using van der waals density functional," *Phys. Rev. B* **98**, 014107 (2018).
- ⁸⁷K. Choudhary, I. Kalish, R. Beams, and F. Tavazza, "High-throughput identification and characterization of two-dimensional materials using density functional theory," *Scientific Reports* **7**, 5179 (2017).
- ⁸⁸B. Himmetoglu, A. Floris, S. de Gironcoli, and M. Cococcioni, "Hubbard-corrected dft energy functionals: The lda+u description of correlated systems," *International Journal of Quantum Chemistry* **114**, 14–49 (2014), <https://onlinelibrary.wiley.com/doi/pdf/10.1002/qua.24521>.
- ⁸⁹S. L. Dudarev, G. A. Botton, S. Y. Savrasov, C. J. Humphreys, and A. P. Sutton, "Electron-energy-loss spectra and the structural stability of nickel oxide: An LSDA+U study," *Phys. Rev. B* **57**, 1505–1509 (1998).
- ⁹⁰I. Timrov, N. Marzari, and M. Cococcioni, "Self-consistent hubbard parameters from density-functional perturbation theory in the ultrasoft and projector-augmented wave formulations," *Phys. Rev. B* **103**, 045141 (2021).
- ⁹¹H. J. Kulik and N. Marzari, "A self-consistent Hubbard U density-functional theory approach to the addition-elimination reactions of hydrocarbons on bare FeO+," *The Journal of Chemical Physics* **129**, 134314 (2008), https://pubs.aip.org/aip/jcp/article-pdf/doi/10.1063/1.2987444/15421335/134314_1_online.pdf.
- ⁹²S. A. Tolba, K. M. Gameel, B. A. Ali, H. A. Almossalami, and N. K. Allam, "The dft+u: Approaches, accuracy, and applications," in *Density Functional Calculations*, edited by G. Yang (IntechOpen, Rijeka, 2018) Chap. 1.
- ⁹³J. Huang, S.-H. Lee, Y.-W. Son, A. Supka, and S. Liu, "First-principles study of two-dimensional ferroelectrics using self-consistent hubbard parameters," *Phys. Rev. B* **102**, 165157 (2020).
- ⁹⁴D. Torelli, K. S. Thygesen, and T. Olsen, "High throughput computational screening for 2d ferromagnetic materials: the critical role of anisotropy and local correlations," *2D Materials* **6**, 045018 (2019).
- ⁹⁵J. P. Perdew, "Density functional theory and the band gap problem," *International Journal of Quantum Chemistry* **28**, 497–523 (1985), <https://onlinelibrary.wiley.com/doi/pdf/10.1002/qua.560280846>.
- ⁹⁶P. Borlido, J. Schmidt, A. W. Huran, F. Tran, M. A. L. Marques, and S. Botti, "Exchange-correlation functionals for band gaps of solids: benchmark, reparametrization and machine learning," *npj Computational Materials* **6**, 96 (2020).
- ⁹⁷J. M. Crowley, J. Tahir-Kheli, and W. A. I. Goddard, "Resolution of the band gap prediction problem for materials design," *The Journal of Physical Chemistry Letters* **7**, 1198–1203 (2016).
- ⁹⁸J. P. Perdew, W. Yang, K. Burke, Z. Yang, E. K. U. Gross, M. Scheffler, G. E. Scuseria, T. M. Henderson, I. Y. Zhang, A. Ruzsinszky, H. Peng, J. Sun, E. Trushin, and A. Görling, "Understanding band gaps of solids in generalized kohn–sham theory," *Proceedings of the National Academy of Sciences* **114**, 2801–2806 (2017), <https://www.pnas.org/doi/pdf/10.1073/pnas.1621352114>.
- ⁹⁹G. Onida, L. Reining, and A. Rubio, "Electronic excitations: density-functional versus many-body green's-function approaches," *Rev. Mod. Phys.* **74**, 601–659 (2002).
- ¹⁰⁰L. Hedin, "New method for calculating the one-particle green's function with application to the electron-gas problem," *Phys. Rev.* **139**, A796–A823 (1965).
- ¹⁰¹M. S. Hybertsen and S. G. Louie, "Electron correlation in semiconductors and insulators: Band gaps and quasiparticle energies," *Phys. Rev. B* **34**, 5390–5413 (1986).
- ¹⁰²S. M. Dancoff, "Non-adiabatic meson theory of nuclear forces," *Phys. Rev.* **78**, 382–385 (1950).
- ¹⁰³W. M. C. Foulkes, L. Mitás, R. J. Needs, and G. Rajagopal, "Quantum monte carlo simulations of solids," *Rev. Mod. Phys.* **73**, 33–83 (2001).
- ¹⁰⁴E. C. Ahn, "2d materials for spintronic devices," *npj 2D Materials and Applications* **4**, 17 (2020).
- ¹⁰⁵M. Kurpas, P. E. Faria Junior, M. Gmitra, and J. Fabian, "Spin-orbit coupling in elemental two-dimensional materials," *Phys. Rev. B* **100**, 125422 (2019).
- ¹⁰⁶K. Premasiri and X. P. A. Gao, "Tuning spin–orbit coupling in 2d materials for spintronics: a topical review," *Journal of Physics: Condensed Matter* **31**, 193001 (2019).
- ¹⁰⁷J. R. Schaibley, H. Yu, G. Clark, P. Rivera, J. S. Ross, K. L. Seyler, W. Yao, and X. Xu, "Valleytronics in 2d materials," *Nature Reviews Materials* **1**, 16055 (2016).
- ¹⁰⁸R. Rodrigues Pela, C. Vona, S. Lubeck, B. Alex, I. Gonzalez Oliva, and C. Draxl, "Critical assessment of g0w0 calculations for 2d materials: the example of monolayer mos₂," *npj Computational Materials* **10**, 77 (2024).
- ¹⁰⁹D. Staros, G. Hu, J. Tiihonen, R. Nanguneri, J. Krogel, M. C. Bennett, O. Heinonen, P. Ganesh, and B. Rubenstein, "A combined first principles study of the structural, magnetic, and phonon properties of monolayer CrI₃," *The Journal of Chemical Physics* **156**, 014707 (2022), https://pubs.aip.org/aip/jcp/article-pdf/doi/10.1063/5.0074848/16535185/014707_1_online.pdf.
- ¹¹⁰D. Wines, K. Choudhary, and F. Tavazza, "Systematic dft+u and quantum monte carlo benchmark of magnetic two-dimensional (2d) crx3 (x = i, br, cl, f)," *The Journal of Physical Chemistry C* **127**, 1176–1188 (2023).
- ¹¹¹J. A. Reyes-Retana and F. Cervantes-Sodi, "Spin-orbital effects in metal-dichalcogenide semiconducting monolayers," *Scientific Reports* **6**, 24093 (2016).
- ¹¹²H. T. T. Nguyen, V. T. T. Vi, T. V. Vu, N. V. Hieu, D. V. Lu, D. P. Rai, and N. T. T. Binh, "Spin–orbit coupling effect on electronic, optical, and thermoelectric properties of janus ga₂ss₂," *RSC Adv.* **10**, 44785–44792 (2020).
- ¹¹³M. Pazoki, R. Imani, A. Röckert, and T. Edvinsson, "Electronic structure of 2d hybrid perovskites: Rashba spin–orbit coupling and impact of inter-layer spacing," *J. Mater. Chem. A* **10**, 20896–20904 (2022).
- ¹¹⁴R. Jastrow, "Many-body problem with strong forces," *Phys. Rev.* **98**, 1479–1484 (1955).
- ¹¹⁵A. Benali, K. Gasperich, K. D. Jordan, T. Applencourt, Y. Luo, M. C. Bennett, J. T. Krogel, L. Shulenburg, P. R. C. Kent, P.-F. Loos, A. Scemama, and M. Caffarel, "Toward a systematic improvement of the fixed-node approximation in diffusion Monte Carlo for solids—A case study in diamond," *Journal of Chemical Physics* **153**, 184111 (2020).
- ¹¹⁶F. D. Malone, A. Benali, M. A. Morales, M. Caffarel, P. R. C. Kent, and L. Shulenburg, "Systematic comparison and cross-validation of fixed-node diffusion Monte Carlo and phaseless auxiliary-field quantum Monte Carlo in solids," *Physical Review B* **102**, 161104 (2020).
- ¹¹⁷C. J. Umrigar and C. Filippi, "Energy and variance optimization of many-body wave functions," *Phys. Rev. Lett.* **94**, 150201 (2005).
- ¹¹⁸C. J. Umrigar, J. Toulouse, C. Filippi, S. Sorella, and R. G. Hennig, "Alleviation of the fermion-sign problem by optimization of many-body wave functions," *Phys. Rev. Lett.* **98**, 110201 (2007).
- ¹¹⁹D. M. Ceperley and B. J. Alder, "Quantum Monte Carlo for molecules: Green's function and nodal release," *The Journal of Chemical Physics* **81**, 5833–5844 (1984), https://pubs.aip.org/aip/jcp/article-pdf/81/12/5833/14120713/5833_1_online.pdf.
- ¹²⁰P. J. Reynolds, D. M. Ceperley, B. J. Alder, and J. Lester, William A., "Fixed-node quantum Monte Carlo for molecules(a) b)," *The Journal of Chemical Physics* **77**, 5593–5603 (1982), https://pubs.aip.org/aip/jcp/article-pdf/77/11/5593/11300510/5593_1_online.pdf.
- ¹²¹C. A. Melton and L. Mitás, "Many-body electronic structure of lasco₃ by real-space quantum monte carlo," *Phys. Rev. B* **102**, 045103 (2020).
- ¹²²A. Annaberdiev, C. A. Melton, G. Wang, and L. Mitás, "Electronic structure of α -rucl₃ by fixed-node and fixed-phase diffusion monte carlo methods," *Phys. Rev. B* **106**, 075127 (2022).
- ¹²³K. Saritas, J. T. Krogel, S. Okamoto, H. N. Lee, and F. A. Reboredo, "Structural, electronic, and magnetic properties of bulk and epitaxial laco₃ through diffusion monte carlo," *Phys. Rev. Mater.* **3**, 124414 (2019).
- ¹²⁴K. Saritas, J. T. Krogel, P. R. C. Kent, and F. A. Reboredo, "Diffusion monte carlo: A pathway towards an accurate theoretical description of manganese oxides," *Phys. Rev. Mater.* **2**, 085801 (2018).
- ¹²⁵K. Foyevtsova, J. T. Krogel, J. Kim, P. R. C. Kent, E. Dagotto, and F. A. Reboredo, "Ab initio quantum monte carlo calculations of spin superexchange in cuprates: The benchmarking case of ca₂cuo₃," *Phys. Rev. X* **4**,

- 031003 (2014).
- ¹²⁶M. A. Morales, J. McMinis, B. K. Clark, J. Kim, and G. E. Scuseria, "Multideterminant wave functions in quantum monte carlo," *Journal of Chemical Theory and Computation* **8**, 2181–2188 (2012).
 - ¹²⁷P. López Ríos, A. Ma, N. D. Drummond, M. D. Towler, and R. J. Needs, "Inhomogeneous backflow transformations in quantum monte carlo calculations," *Phys. Rev. E* **74**, 066701 (2006).
 - ¹²⁸N. Devaux, M. Casula, F. Decremps, and S. Sorella, "Electronic origin of the volume collapse in cerium," *Physical Review B* **91**, 081101 (2015).
 - ¹²⁹M. Casula and S. Sorella, "Improper s -wave symmetry of the electronic pairing in iron-based superconductors by first-principles calculations," *Physical Review B* **88**, 155125 (2013).
 - ¹³⁰J. R. Trail and R. J. Needs, "Correlated electron pseudopotentials for 3d-transition metals," *The Journal of Chemical Physics* **142**, 064110 (2015), https://pubs.aip.org/aip/jcp/article-pdf/doi/10.1063/1.4907589/14030343/064110_1_online.pdf.
 - ¹³¹J. T. Krogel, J. A. Santana, and F. A. Reboredo, "Pseudopotentials for quantum monte carlo studies of transition metal oxides," *Phys. Rev. B* **93**, 075143 (2016).
 - ¹³²J. R. Trail and R. J. Needs, "Shape and energy consistent pseudopotentials for correlated electron systems," *The Journal of Chemical Physics* **146**, 204107 (2017), https://pubs.aip.org/aip/jcp/article-pdf/doi/10.1063/1.4984046/13610682/204107_1_online.pdf.
 - ¹³³M. C. Bennett, C. A. Melton, A. Annaberdiyev, G. Wang, L. Shulenburger, and L. Mitás, "A new generation of effective core potentials for correlated calculations," *The Journal of Chemical Physics* **147**, 224106 (2017), https://pubs.aip.org/aip/jcp/article-pdf/doi/10.1063/1.4995643/13471130/224106_1_online.pdf.
 - ¹³⁴M. C. Bennett, G. Wang, A. Annaberdiyev, C. A. Melton, L. Shulenburger, and L. Mitás, "A new generation of effective core potentials from correlated calculations: 2nd row elements," *The Journal of Chemical Physics* **149**, 104108 (2018), https://pubs.aip.org/aip/jcp/article-pdf/doi/10.1063/1.5038135/15547024/104108_1_online.pdf.
 - ¹³⁵A. Annaberdiyev, G. Wang, C. A. Melton, M. C. Bennett, L. Shulenburger, and L. Mitás, "A new generation of effective core potentials from correlated calculations: 3d transition metal series," *The Journal of Chemical Physics* **149**, 134108 (2018), https://pubs.aip.org/aip/jcp/article-pdf/doi/10.1063/1.5040472/15546971/134108_1_online.pdf.
 - ¹³⁶G. Wang, A. Annaberdiyev, C. A. Melton, M. C. Bennett, L. Shulenburger, and L. Mitás, "A new generation of effective core potentials from correlated calculations: 4s and 4p main group elements and first row additions," *The Journal of Chemical Physics* **151**, 144110 (2019), https://pubs.aip.org/aip/jcp/article-pdf/doi/10.1063/1.5121006/15565392/144110_1_online.pdf.
 - ¹³⁷G. Wang, B. Kincaid, H. Zhou, A. Annaberdiyev, M. C. Bennett, J. T. Krogel, and L. Mitás, "A new generation of effective core potentials from correlated and spin-orbit calculations: Selected heavy elements," *The Journal of Chemical Physics* **157**, 054101 (2022), https://pubs.aip.org/aip/jcp/article-pdf/doi/10.1063/5.0087300/16547409/054101_1_online.pdf.
 - ¹³⁸B. Kincaid, G. Wang, H. Zhou, and L. Mitás, "Correlation consistent effective core potentials for late 3d transition metals adapted for plane wave calculations," *The Journal of Chemical Physics* **157**, 174307 (2022), https://pubs.aip.org/aip/jcp/article-pdf/doi/10.1063/5.0109098/16554726/174307_1_online.pdf.
 - ¹³⁹H. Zhou, B. Kincaid, G. Wang, A. Annaberdiyev, P. Ganesh, and L. Mitás, "A new generation of effective core potentials: selected lanthanides and heavy elements," (2023), [arXiv:2309.12145 \[cond-mat.mtrl-sci\]](https://arxiv.org/abs/2309.12145).
 - ¹⁴⁰M. Casula, S. Moroni, S. Sorella, and C. Filippi, "Size-consistent variational approaches to nonlocal pseudopotentials: Standard and lattice regularized diffusion Monte Carlo methods revisited," *The Journal of Chemical Physics* **132**, 154113 (2010), https://pubs.aip.org/aip/jcp/article-pdf/doi/10.1063/1.3380831/15682830/154113_1_online.pdf.
 - ¹⁴¹L. Mitás, E. L. Shirley, and D. M. Ceperley, "Nonlocal pseudopotentials and diffusion monte carlo," *The Journal of Chemical Physics* **95**, 3467–3475 (1991).
 - ¹⁴²R. J. Needs, M. D. Towler, N. D. Drummond, and P. L. Ríos, "Continuum variational and diffusion quantum monte carlo calculations," *Journal of Physics: Condensed Matter* **22**, 023201 (2009).
 - ¹⁴³W. A. Wheeler, S. Pathak, K. G. Kleiner, S. Yuan, J. N. B. Rodrigues, C. Lorusso, K. Krongchon, Y. Chang, Y. Zhou, B. Busemeyer, K. T. Williams, A. Muñoz, C. Y. Chow, and L. K. Wagner, "PyQMC: An all-Python real-space quantum Monte Carlo module in PySCF," *The Journal of Chemical Physics* **158**, 114801 (2023), https://pubs.aip.org/aip/jcp/article-pdf/doi/10.1063/5.0139024/16794896/114801_1_online.pdf.
 - ¹⁴⁴L. K. Wagner, M. Bajdich, and L. Mitás, "Qwalk: A quantum monte carlo program for electronic structure," *Journal of Computational Physics* **228**, 3390–3404 (2009).
 - ¹⁴⁵J. Kim, A. D. Baczewski, T. D. Beaudet, A. Benali, M. C. Bennett, M. A. Berrill, N. S. Blunt, E. J. L. Borda, M. Casula, D. M. Ceperley, S. Chiesa, B. K. Clark, R. C. Clay, K. T. Delaney, M. Dewing, K. P. Esler, H. Hao, O. Heinonen, P. R. C. Kent, J. T. Krogel, I. Kylänpää, Y. W. Li, M. G. Lopez, Y. Luo, F. D. Malone, R. M. Martin, A. Mathuriya, J. McMinis, C. A. Melton, L. Mitás, M. A. Morales, E. Neuscamman, W. D. Parker, S. D. P. Flores, N. A. Romero, B. M. Rubenstein, J. A. R. Shea, H. Shin, L. Shulenburger, A. F. Tillack, J. P. Townsend, N. M. Tubman, B. V. D. Goetz, J. E. Vincent, D. C. Yang, Y. Yang, S. Zhang, and L. Zhao, "Qmcpack: an open source ab initio quantum monte carlo package for the electronic structure of atoms, molecules and solids," *Journal of Physics: Condensed Matter* **30**, 195901 (2018).
 - ¹⁴⁶P. R. C. Kent, A. Annaberdiyev, A. Benali, M. C. Bennett, E. J. Landinez Borda, P. Doak, H. Hao, K. D. Jordan, J. T. Krogel, I. Kylänpää, J. Lee, Y. Luo, F. D. Malone, C. A. Melton, L. Mitás, M. A. Morales, E. Neuscamman, F. A. Reboredo, B. Rubenstein, K. Saritas, S. Upadhyay, G. Wang, S. Zhang, and L. Zhao, "QMCPACK: Advances in the development, efficiency, and application of auxiliary field and real-space variational and diffusion quantum Monte Carlo," *The Journal of Chemical Physics* **152**, 174105 (2020), https://pubs.aip.org/aip/jcp/article-pdf/doi/10.1063/5.0004860/16740875/174105_1_online.pdf.
 - ¹⁴⁷J. T. Krogel, "Nexus: A modular workflow management system for quantum simulation codes," *Computer Physics Communications* **198**, 154–168 (2016).
 - ¹⁴⁸K. Nakano, O. Kohulák, A. Raghav, M. Casula, and S. Sorella, "TurboGenius: Python suite for high-throughput calculations of ab initio quantum Monte Carlo methods," *The Journal of Chemical Physics* **159**, 224801 (2023).
 - ¹⁴⁹M. Bonilla, S. Kolekar, Y. Ma, H. C. Diaz, V. Kalappattil, R. Das, T. Eggers, H. R. Gutierrez, M.-H. Phan, and M. Batzill, "Strong room-temperature ferromagnetism in VSe₂ monolayers on van der Waals substrates," *Nature Nanotechnology* **13**, 289–293 (2018).
 - ¹⁵⁰C. Gong, L. Li, Z. Li, H. Ji, A. Stern, Y. Xia, T. Cao, W. Bao, C. Wang, Y. Wang, Z. Q. Qiu, R. J. Cava, S. G. Louie, J. Xie, and X. Zhang, "Discovery of intrinsic ferromagnetism in two-dimensional van der Waals crystals," *Nature* **546**, 265–269 (2017).
 - ¹⁵¹J.-U. Lee, S. Lee, J. H. Ryoo, S. Kang, T. Y. Kim, P. Kim, C.-H. Park, J.-G. Park, and H. Cheong, "Ising-type magnetic ordering in atomically thin fe₃," *Nano Letters* **16**, 7433–7438 (2016).
 - ¹⁵²K. Kim, S. Y. Lim, J.-U. Lee, S. Lee, T. Y. Kim, K. Park, G. S. Jeon, C.-H. Park, J.-G. Park, and H. Cheong, "Suppression of magnetic ordering in xxz-type antiferromagnetic monolayer nips₃," *Nature Communications* **10**, 345 (2019).
 - ¹⁵³H. Chu, C. J. Roh, J. O. Island, C. Li, S. Lee, J. Chen, J.-G. Park, A. F. Young, J. S. Lee, and D. Hsieh, "Linear magnetoelectric phase in ultrathin mnps₃ probed by optical second harmonic generation," *Phys. Rev. Lett.* **124**, 027601 (2020).
 - ¹⁵⁴Z. Fei, B. Huang, P. Malinowski, W. Wang, T. Song, J. Sanchez, W. Yao, D. Xiao, X. Zhu, A. F. May, W. Wu, D. H. Cobden, J.-H. Chu, and X. Xu, "Two-dimensional itinerant ferromagnetism in atomically thin fe₃gete₂," *Nature Materials* **17**, 778–782 (2018).
 - ¹⁵⁵B. Sachs, T. O. Wehling, K. S. Novoselov, A. I. Lichtenstein, and M. I. Katsnelson, "Ferromagnetic two-dimensional crystals: Single layers of K₂CuF₄," *Phys. Rev. B* **88**, 201402 (2013).
 - ¹⁵⁶B. L. Chittari, Y. Park, D. Lee, M. Han, A. H. MacDonald, E. Hwang, and J. Jung, "Electronic and magnetic properties of single-layer mPX₃ metal phosphorus trichalcogenides," *Phys. Rev. B* **94**, 184428 (2016).
 - ¹⁵⁷S. Sarikurt, Y. Kadioglu, F. Ersan, E. Vatansver, O. U. Akturk, Y. Yuksel, U. Akinci, and E. Akturk, "Electronic and magnetic properties of monolayer α -RuCl₃: a first-principles and Monte Carlo study," *Phys. Chem.*

- Chem. Phys.* **20**, 997–1004 (2018).
- ¹⁵⁸F. Ersan, E. Vatanserver, S. Sarikurt, Y. Yuksel, Y. Kadioglu, H. D. Ozaydin, O. U. Akturk, U. Akinci, and E. Akturk, “Exploring the electronic and magnetic properties of new metal halides from bulk to two-dimensional monolayer: RuX_3 ($X = Br, I$),” *Journal of Magnetism and Magnetic Materials* **476**, 111–119 (2019).
- ¹⁵⁹N. D. Mermin and H. Wagner, “Absence of ferromagnetism or antiferromagnetism in one- or two-dimensional isotropic heisenberg models,” *Phys. Rev. Lett.* **17**, 1133–1136 (1966).
- ¹⁶⁰D. Torelli and T. Olsen, “Calculating critical temperatures for ferromagnetic order in two-dimensional materials,” *2D Materials* **6**, 015028 (2018).
- ¹⁶¹T. Yu, R. Liu, H. Mao, X. Ma, G. Wang, Z. Yuan, P. Zheng, Y. Peng, and Z. Yin, “Electronic structure and magnetism of the hund’s insulator cr_3 ,” *Phys. Rev. B* **105**, 165127 (2022).
- ¹⁶²J. L. Lado and J. Fernández-Rossier, “On the origin of magnetic anisotropy in two dimensional CrI_3 ,” *2D Materials* **4**, 035002 (2017).
- ¹⁶³I. Lee, F. G. Utermohlen, D. Weber, K. Hwang, C. Zhang, J. van Tol, J. E. Goldberger, N. Trivedi, and P. C. Hammel, “Fundamental spin interactions underlying the magnetic anisotropy in the kitaev ferromagnet cr_3 ,” *Phys. Rev. Lett.* **124**, 017201 (2020).
- ¹⁶⁴M. Gibertini, M. Koperski, A. F. Morpurgo, and K. S. Novoselov, “Magnetic 2d materials and heterostructures,” *Nature Nanotechnology* **14** (2019).
- ¹⁶⁵N. Sivasdas, S. Okamoto, X. Xu, C. J. Fennie, and D. Xiao, “Stacking-dependent magnetism in bilayer cr_3 ,” *Nano Letters* **18** (2018).
- ¹⁶⁶T. Li, S. Jiang, N. Sivasdas, Z. Wang, Y. Xu, D. Weber, J. E. Goldberger, K. Watanabe, T. Taniguchi, C. J. Fennie, K. Fai Mak, and J. Shan, “Pressure-controlled interlayer magnetism in atomically thin CrI_3 ,” *Nature Materials* **18**, 1303–1308 (2019).
- ¹⁶⁷T. Song, Z. Fei, M. Yankowitz, Z. Lin, Q. Jiang, K. Hwangbo, Q. Zhang, B. Sun, T. Taniguchi, K. Watanabe, M. A. McGuire, D. Graf, T. Cao, J.-H. Chu, D. H. Cobden, C. R. Dean, D. Xiao, and X. Xu, “Switching 2D magnetic states via pressure tuning of layer stacking,” *Nature Materials* **18**, 1298–1302 (2019).
- ¹⁶⁸P. Li, C. Wang, J. Zhang, S. Chen, D. Guo, W. Ji, and D. Zhong, “Single-layer CrI_3 grown by molecular beam epitaxy,” *Science Bulletin* **65**, 1064–1071 (2020).
- ¹⁶⁹B. Yang, X. Zhang, H. Yang, X. Han, and Y. Yan, “Nonmetallic atoms induced magnetic anisotropy in monolayer chromium trihalides,” *Journal of Physical Chemistry C* **123** (2019).
- ¹⁷⁰Z. Wu, J. Yu, and S. Yuan, “Strain-tunable magnetic and electronic properties of monolayer cr_3 ,” *Physical Chemistry Chemical Physics* **21** (2019).
- ¹⁷¹W. Zhang, Q. Qu, P. Zhu, and C. Lam, “Robust intrinsic ferromagnetism and half semiconductivity in stable two-dimensional single-layer chromium trihalides,” *Journal of Materials Chemistry C* **3** (2015).
- ¹⁷²L. Webster and J. Yan, “Strain-tunable magnetic anisotropy in monolayer cr_3 , $crbr$, and cr_3 ,” *Physical Review B* **98** (2018).
- ¹⁷³L. Webster, L. Liang, and J. Yan, “Distinct spin-lattice and spin-phonon interactions in monolayer magnetic cr_3 ,” *Physical Review B* **20** (2018).
- ¹⁷⁴J. Tiihonen, P. R. C. Kent, and J. T. Krogel, “Surrogate hessian accelerated structural optimization for stochastic electronic structure theories,” *J. Chem. Phys.* **156**, 054104 (2022), <https://doi.org/10.1063/5.0079046>.
- ¹⁷⁵H. Shin, J. T. Krogel, K. Gasperich, P. R. C. Kent, A. Benali, and O. Heinonen, “Optimized structure and electronic band gap of monolayer $gese$ from quantum monte carlo methods,” *Phys. Rev. Mater.* **5**, 024002 (2021).
- ¹⁷⁶D. Wines, J. Tiihonen, K. Saritas, J. T. Krogel, and C. Ataca, “A quantum monte carlo study of the structural, energetic, and magnetic properties of two-dimensional h and t phase vse_2 ,” *The Journal of Physical Chemistry Letters* **14**, 3553–3560 (2023).
- ¹⁷⁷D. Staros, B. Rubenstein, and P. Ganesh, “A first-principles study of bilayer $1t'-wte_2/cr_3$: a candidate topological spin filter,” *npj Spintronics* **2**, 4 (2024).
- ¹⁷⁸D. Torelli, H. Moustafa, K. W. Jacobsen, and T. Olsen, “High-throughput computational screening for two-dimensional magnetic materials based on experimental databases of three-dimensional compounds,” *npj Computational Materials* **6**, 158 (2020).
- ¹⁷⁹D. S. Lambert and D. D. O’Regan, “Use of DFT + U + J with linear response parameters to predict non-magnetic oxide band gaps with hybrid-functional accuracy,” *Phys. Rev. Res.* **5**, 013160 (2023).
- ¹⁸⁰H. H. Kim, B. Yang, S. Li, S. Jiang, C. Jin, Z. Tao, G. Nichols, F. Sfigakis, S. Zhong, C. Li, S. Tian, D. G. Cory, G.-X. Miao, J. Shan, K. F. Mak, H. Lei, K. Sun, L. Zhao, and A. W. Tsen, “Evolution of interlayer and intralayer magnetism in three atomically thin chromium trihalides,” *Proceedings of the National Academy of Sciences* **116**, 11131–11136 (2019), <https://www.pnas.org/doi/pdf/10.1073/pnas.1902100116>.
- ¹⁸¹M. Kim, P. Kumaravadivel, J. Birkbeck, W. Kuang, S. G. Xu, D. G. Hopkinson, J. Knolle, P. A. McClarty, A. I. Berdyugin, M. Ben Shalom, R. V. Gorbachev, S. J. Haigh, S. Liu, J. H. Edgar, K. S. Novoselov, I. V. Grigorieva, and A. K. Geim, “Micromagnetometry of two-dimensional ferromagnets,” *Nature Electronics* **2**, 457–463 (2019).
- ¹⁸²D. Wines, K. Saritas, and C. Ataca, “Intrinsic ferromagnetism of two-dimensional (2d) mno_2 revisited: A many-body quantum monte carlo and dft+u study,” *The Journal of Physical Chemistry C, The Journal of Physical Chemistry C* **126**, 5813–5821 (2022).
- ¹⁸³Y. Omomo, T. Sasaki, Wang, and M. Watanabe, “Redoxable nanosheet crystallites of MnO_2 derived via delamination of a layered manganese oxide,” *Journal of the American Chemical Society, Journal of the American Chemical Society* **125**, 3568–3575 (2003).
- ¹⁸⁴D. A. Kitchaev, H. Peng, Y. Liu, J. Sun, J. P. Perdew, and G. Ceder, “Energetics of MnO_2 polymorphs in density functional theory,” *Phys. Rev. B* **93**, 045132 (2016).
- ¹⁸⁵S. Rong, P. Zhang, and F. Liu, “Scalable synthesis of water-dispersible 2D manganese dioxide monosheets,” *Journal of Physics: Condensed Matter* **32**, 015301 (2019).
- ¹⁸⁶N. Sakai, Y. Ebina, K. Takada, and T. Sasaki, “Photocurrent generation from semiconducting manganese oxide nanosheets in response to visible light,” *The Journal of Physical Chemistry B* **109**, 9651–9655 (2005).
- ¹⁸⁷C. Sun, Y. Wang, J. Zou, and S. C. Smith, “A formation mechanism of oxygen vacancies in a MnO_2 monolayer: a DFT + U study,” *Phys. Chem. Chem. Phys.* **13**, 11325–11328 (2011).
- ¹⁸⁸H.-J. Liu, J.-C. Lin, Y.-W. Fang, J.-C. Wang, B.-C. Huang, X. Gao, R. Huang, P. R. Dean, P. D. Hatton, Y.-Y. Chin, H.-J. Lin, C.-T. Chen, Y. Ikuhara, Y.-P. Chiu, C.-S. Chang, C.-G. Duan, Q. He, and Y.-H. Chu, “A metal-insulator transition of the buried MnO_2 monolayer in complex oxide heterostructure,” *Advanced Materials* **28**, 9142–9151 (2016).
- ¹⁸⁹M. Kan, J. Zhou, Q. Sun, Y. Kawazoe, and P. Jena, “The intrinsic ferromagnetism in a MnO_2 monolayer,” *The Journal of Physical Chemistry Letters* **4**, 3382–3386 (2013).
- ¹⁹⁰L. Wang, T. Maxisch, and G. Ceder, “Oxidation energies of transition metal oxides within the GGA + U framework,” *Phys. Rev. B* **73**, 195107 (2006).
- ¹⁹¹W. Yu, J. Li, T. S. Herg, Z. Wang, X. Zhao, X. Chi, W. Fu, I. Abdelwahab, J. Zhou, J. Dan, Z. Chen, Z. Chen, Z. Li, J. Lu, S. J. Pennycook, Y. P. Feng, J. Ding, and K. P. Loh, “Chemically exfoliated vse_2 monolayers with room-temperature ferromagnetism,” *Advanced Materials* **31**, 1903779 (2019), <https://onlinelibrary.wiley.com/doi/pdf/10.1002/adma.201903779>.
- ¹⁹²X. Wang, D. Li, Z. Li, C. Wu, C.-M. Che, G. Chen, and X. Cui, “Ferromagnetism in 2d vanadium diselenide,” *ACS Nano, ACS Nano* **15**, 16236–16241 (2021).
- ¹⁹³H.-R. Fuh, C.-R. Chang, Y.-K. Wang, R. F. L. Evans, R. W. Chantrell, and H.-T. Jeng, “Newtype single-layer magnetic semiconductor in transition-metal dichalcogenides v_x_2 ($x = s, se$ and te),” *Scientific Reports* **6**, 32625 (2016).
- ¹⁹⁴D. Li, X. Wang, C.-m. Kan, D. He, Z. Li, Q. Hao, H. Zhao, C. Wu, C. Jin, and X. Cui, “Structural phase transition of multilayer vse_2 ,” *ACS Applied Materials & Interfaces* **12**, 25143–25149 (2020).
- ¹⁹⁵G. V. Pushkarev, V. G. Mazurenko, V. V. Mazurenko, and D. W. Boukhvalov, “Structural phase transitions in vse_2 : Energetics, electronic structure and magnetism,” *Phys. Chem. Chem. Phys.* **21**, 22647–22653 (2019).
- ¹⁹⁶G. Duvjir, B. K. Choi, I. Jang, S. Ulstrup, S. Kang, T. Thi Ly, S. Kim, Y. H. Choi, C. Jozwiak, A. Bostwick, E. Rotenberg, J.-G. Park, R. Sankar, K.-S. Kim, J. Kim, and Y. J. Chang, “Emergence of a metal–insulator transition and high-temperature charge-density waves in vse_2 at the monolayer limit,” *Nano Lett., Nano Lett.* **18**, 5432–5438 (2018).
- ¹⁹⁷B. Wood, N. D. M. Hine, W. M. C. Foulkes, and P. García-González, “Quantum monte carlo calculations of the surface energy of an electron gas,” *Phys. Rev. B* **76**, 035403 (2007).

- ¹⁹⁸A.-Y. Lu, H. Zhu, J. Xiao, C.-P. Chuu, Y. Han, M.-H. Chiu, C.-C. Cheng, C.-W. Yang, K.-H. Wei, Y. Yang, Y. Wang, D. Sokaras, D. Nordlund, P. Yang, D. A. Muller, M.-Y. Chou, X. Zhang, and L.-J. Li, “Janus monolayers of transition metal dichalcogenides,” *Nature Nanotechnology* **12**, 744–749 (2017).
- ¹⁹⁹E. Gaufrès, F. Fossard, V. Gosselin, L. Sponza, F. Ducastelle, Z. Li, S. G. Louie, R. Martel, M. Côté, and A. Loiseau, “Momentum-Resolved Dielectric Response of Free-Standing Mono-, Bi-, and Trilayer Black Phosphorus,” *Nano Lett.* **19**, 8303–8310 (2019).
- ²⁰⁰N. Zibouche, M. Schlipf, and F. Giustino, “Gw band structure of monolayer MoS_2 using the sternheimer method and effect of dielectric environment,” *Phys. Rev. B* **103**, 125401 (2021).
- ²⁰¹T. Frank, R. Derian, K. Tokár, L. Mitas, J. Fabian, and I. Štich, “Many-Body Quantum Monte Carlo Study of 2D Materials: Cohesion and Band Gap in Single-Layer Phosphorene,” *Phys. Rev. X* **9**, 011018 (2019).
- ²⁰²Y. Huang, A. Faizan, M. Manzoor, J. Brndiar, L. Mitas, J. Fabian, and I. Štich, “Colossal band gap response of single-layer phosphorene to strain predicted by quantum monte carlo,” *Phys. Rev. Res.* **5**, 033223 (2023).
- ²⁰³M. Dubecký, F. Karlický, S. Minárik, and L. Mitas, “Fundamental gap of fluorographene by many-body GW and fixed-node diffusion Monte Carlo methods,” *The Journal of Chemical Physics* **153**, 184706 (2020), https://pubs.aip.org/aip/jcp/article-pdf/doi/10.1063/5.0030952/15583281/184706_1_online.pdf.
- ²⁰⁴D. Wines, K. Saritas, and C. Ataca, “A first-principles Quantum Monte Carlo study of two-dimensional (2D) GaSe,” *The Journal of Chemical Physics* **153**, 154704 (2020), https://pubs.aip.org/aip/jcp/article-pdf/doi/10.1063/5.0023223/14698229/154704_1_online.pdf.
- ²⁰⁵R. J. Hunt, B. Monserrat, V. Zólyomi, and N. D. Drummond, “Diffusion quantum monte carlo and gw study of the electronic properties of monolayer and bulk hexagonal boron nitride,” *Phys. Rev. B* **101**, 205115 (2020).
- ²⁰⁶A. Annaberdiyev, G. Wang, C. A. Melton, M. C. Bennett, and L. Mitas, “Cohesion and excitations of diamond-structure silicon by quantum monte carlo: Benchmarks and control of systematic biases,” *Phys. Rev. B* **103**, 205206 (2021).
- ²⁰⁷J. Brndiar and I. Stich, (2023), unpublished.
- ²⁰⁸E. Mostaani, M. Szyniszewski, C. H. Price, R. Maezono, M. Danovich, R. J. Hunt, N. D. Drummond, and V. I. Fal’ko, “Diffusion quantum monte carlo study of excitonic complexes in two-dimensional transition-metal dichalcogenides,” *Phys. Rev. B* **96**, 075431 (2017).
- ²⁰⁹M. Szyniszewski, E. Mostaani, N. D. Drummond, and V. I. Fal’ko, “Binding energies of trions and biexcitons in two-dimensional semiconductors from diffusion quantum monte carlo calculations,” *Phys. Rev. B* **95**, 081301 (2017).
- ²¹⁰R. Roldán, A. Castellanos-Gomez, E. Capelluti, and F. Guinea, F. Guinea, “Strain engineering in semiconducting two-dimensional crystals,” *J. Phys.: Condens. Matter* **27**, 313201 (2015).
- ²¹¹Y. S., Y. Chen, and C. Jiang, “Strain engineering of two-dimensional materials: Methods, properties, and applications,” *InfoMat.* **3**, 397–420 (2021).
- ²¹²R. Ganatra and Q. Zhang, “Few-Layer MoS_2 : A Promising Layered Semiconductor,” *ACS Nano* **8**, 4074–4099 (2014).
- ²¹³Y. Huang, M. Manzoor, J. Brndiar, M. Milivojevic, and I. Štich, “Straintronics with single-layer MoS_2 : A quantum Monte Carlo study,” *Phys. Rev. Res.* **6**, 013007 (2024).
- ²¹⁴R. Eymard and A. Otto, “Optical and electron-energy-loss spectroscopy of gese, gese, sns, and snse single crystals,” *Phys. Rev. B* **16**, 1616–1623 (1977).
- ²¹⁵D. D. I. Vaughn, R. J. Patel, M. A. Hickner, and R. E. Schaak, “Single-crystal colloidal nanosheets of gese and gese,” *Journal of the American Chemical Society* **132**, 15170–15172 (2010).
- ²¹⁶P. Mishra, H. Lohani, A. K. Kundu, R. Patel, G. K. Solanki, K. S. R. Menon, and B. R. Sekhar, “Electronic structure of germanium selenide investigated using ultra-violet photo-electron spectroscopy,” *Semiconductor Science and Technology* **30**, 075001 (2015).
- ²¹⁷P. A. E. Murgatroyd, M. J. Smiles, C. N. Savory, T. P. Shalvey, J. E. N. Swallow, N. Fleck, C. M. Robertson, F. Jäckel, J. Alaria, J. D. Major, D. O. Scanlon, and T. D. Veal, “Gese: Optical spectroscopy and theoretical study of a van der waals solar absorber,” *Chemistry of Materials* **32**, 3245–3253 (2020).
- ²¹⁸T. Wang, Q. Zhang, J. Li, and C. Xia, “2d gese/sns(snse^2) broken-gap heterostructures for tunnel field-effect transistors applications,” *Journal of Physics D: Applied Physics* **52**, 455103 (2019).
- ²¹⁹C. Xia, J. Du, W. Xiong, Y. Jia, Z. Wei, and J. Li, “A type-ii gese/sns heterobilayer with a suitable direct gap, superior optical absorption and broad spectrum for photovoltaic applications,” *J. Mater. Chem. A* **5**, 13400–13410 (2017).
- ²²⁰A. K. Singh and R. G. Hennig, “Computational prediction of two-dimensional group-IV mono-chalcogenides,” *Applied Physics Letters* **105**, 042103 (2014), https://pubs.aip.org/aip/apl/article-pdf/doi/10.1063/1.4891230/14309133/042103_1_online.pdf.
- ²²¹E. P. O. O’Reilly, “The electronic structure of ge-se and ge-te compounds,” *Journal of Physics C: Solid State Physics* **15**, 1449 (1982).
- ²²²Y. Ni, H. Wu, C. Huang, M. Mao, Z. Wang, and X. Cheng, “Growth and quality of gallium selenide (GaSe) crystals,” *Journal of Crystal Growth* **381**, 10–14 (2013).
- ²²³D. V. Rybkovskiy, N. R. Arutyunyan, A. S. Orekhov, I. A. Gromchenko, I. V. Vorobiev, A. V. Osadchy, E. Y. Salaev, T. K. Baykara, K. R. Al-lakhverdiev, and E. D. Obraztsova, “Size-induced effects in gallium selenide electronic structure: The influence of interlayer interactions,” *Phys. Rev. B* **84**, 085314 (2011).
- ²²⁴V. Zólyomi, N. D. Drummond, and V. I. Fal’ko, “Band structure and optical transitions in atomic layers of hexagonal gallium chalcogenides,” *Phys. Rev. B* **87**, 195403 (2013).
- ²²⁵O. D. Pozo-Zamudio, S. Schwarz, M. Sich, I. A. Akimov, M. Bayer, R. C. Schofield, E. A. Chekhovich, B. J. Robinson, N. D. Kay, O. V. Kolosov, A. I. Dmitriev, G. V. Lashkarev, D. N. Borisenko, N. N. Kolesnikov, and A. I. Tartakovskii, “Photoluminescence of two-dimensional GaTe and GaSe films,” *2D Materials* **2**, 035010 (2015).
- ²²⁶S. Lei, L. Ge, Z. Liu, S. Najmaei, G. Shi, G. You, J. Lou, R. Vajtai, and P. M. Ajayan, “Synthesis and photoresponse of large GaSe atomic layers,” *Nano Letters* **13**, 2777–2781 (2013).
- ²²⁷Y. Ma, Y. Dai, M. Guo, L. Yu, and B. Huang, “Tunable electronic and dielectric behavior of GaS and GaSe monolayers,” *Phys. Chem. Chem. Phys.* **15**, 7098–7105 (2013).
- ²²⁸D. J. Late, B. Liu, J. Luo, A. Yan, H. S. S. R. Matte, M. Grayson, C. N. R. Rao, and V. P. Dravid, “GaS and GaSe ultrathin layer transistors,” *Advanced Materials* **24**, 3549–3554 (2012).
- ²²⁹Y. Depeursinge, “Electronic band structure for the polytypes of GaSe,” *Il Nuovo Cimento B (1971-1996)* **38**, 153–158 (1977).
- ²³⁰B. P. Bahuguna, L. K. Saini, R. O. Sharma, and B. Tiwari, “Hybrid functional calculations of electronic and thermoelectric properties of GaS, GaSe, and GaTe monolayers,” *Phys. Chem. Chem. Phys.* **20**, 28575–28582 (2018).
- ²³¹H. R. Jappor and M. A. Habeeb, “Optical properties of two-dimensional GaS and GaSe monolayers,” *Physica E: Low-dimensional Systems and Nanostructures* **101**, 251–255 (2018).
- ²³²H. L. Zhuang and R. G. Hennig, “Single-Layer Group-III Monochalcogenide Photocatalysts for Water Splitting,” *Chemistry of Materials* **25**, 3232–3238 (2013).
- ²³³M. Burkatzki, C. Filippi, and M. Dolg, “Energy-consistent pseudopotentials for Quantum Monte Carlo calculations,” *The Journal of Chemical Physics* **126**, 234105 (2007).
- ²³⁴M. Burkatzki, C. Filippi, and M. Dolg, “Energy-consistent small-core pseudopotentials for 3d-transition metals adapted to Quantum Monte Carlo calculations,” *The Journal of Chemical Physics* **129**, 164115 (2008).
- ²³⁵P. E. Blöchl, “Projector augmented-wave method,” *Phys. Rev. B* **50**, 17953–17979 (1994).
- ²³⁶G. Kresse and D. Joubert, “From ultrasoft pseudopotentials to the projector augmented-wave method,” *Phys. Rev. B* **59**, 1758–1775 (1999).
- ²³⁷D. Wines, K. Saritas, and C. Ataca, “A pathway toward high-throughput quantum Monte Carlo simulations for alloys: A case study of two-dimensional (2D) $\text{GaS}_x\text{Se}_{1-x}$,” *The Journal of Chemical Physics* **155**, 194112 (2021), https://pubs.aip.org/aip/jcp/article-pdf/doi/10.1063/5.0070423/15810748/194112_1_online.pdf.
- ²³⁸V. Wang, Z. Q. Wu, Y. Kawazoe, and W. T. Geng, “Tunable band gaps of $\text{In}_x\text{Ga}_{1-x}\text{N}$ alloys: From bulk to two-dimensional limit,” *The Journal of Physical Chemistry C* **122**, 6930–6942 (2018).
- ²³⁹M. Kanli, A. Onen, A. Mogulkoc, and E. Durgun, “Characterization of two-dimensional $\text{Ga}_{1-x}\text{Al}_x\text{N}$ ordered alloys with varying chemical composition,” *Computational Materials Science* **167**, 13–18 (2019).

- ²⁴⁰S. Yang, M. Wu, W. Shen, L. Huang, S. Tongay, K. Wu, B. Wei, Y. Qin, Z. Wang, C. Jiang, and C. Hu, "Highly sensitive polarization photodetection using a pseudo-one-dimensional Nb_{1-x}Ti_xS₃ alloy," *ACS Applied Materials & Interfaces* **11**, 3342–3350 (2019).
- ²⁴¹F. Ersan, H. D. Ozaydin, and E. Aktürk, "Influence of chalcogen composition on the structural transition and on the electronic and optical properties of the monolayer titanium trichalcogenide ordered alloys," *Phys. Chem. Chem. Phys.* **20**, 1431–1439 (2018).
- ²⁴²F. Ersan, G. Gökoğlu, and E. Aktürk, "Adsorption and diffusion of lithium on monolayer transition metal dichalcogenides (MoS₂(1-x)Se_{2x}) alloys," *The Journal of Physical Chemistry C* **119**, 28648–28653 (2015).
- ²⁴³H. Mo, X. Zhang, Y. Liu, P. Kang, H. Nan, X. Gu, K. K. Ostrikov, and S. Xiao, "Two-dimensional alloying molybdenum tin disulfide monolayers with fast photoresponse," *ACS Applied Materials & Interfaces* **11**, 39077–39087 (2019).
- ²⁴⁴I. Miyazato, S. Sarikurt, K. Takahashi, and F. Ersan, "Controlling electronic structure of single-layered HfX₃ (X = S, Se) trichalcogenides through systematic zr doping," *Journal of Materials Science* **55**, 660–669 (2020).
- ²⁴⁵F. Raffone, C. Ataca, J. C. Grossman, and G. Cicero, "MoS₂ enhanced T-phase stabilization and tunability through alloying," *The Journal of Physical Chemistry Letters* **7**, 2304–2309 (2016).
- ²⁴⁶R. H. Almadvari, M. Nayeri, and S. Fotoohi, "Engineering of electronic and optical properties of monolayer gallium sulfide/selenide in presence of intrinsic atomic defects," *Materials Research Express* **7**, 015915 (2020).
- ²⁴⁷D. Wines, F. Ersan, and C. Ataca, "Engineering the electronic, thermoelectric, and excitonic properties of two-dimensional group-III nitrides through alloying for optoelectronic devices (B_{1-x}Al_xN, Al_{1-x}Ga_xN, and Ga_{1-x}In_xN)," *ACS Applied Materials & Interfaces* **12**, 46416–46428 (2020).
- ²⁴⁸H. T. T. Nguyen, M. M. Obeid, A. Bafekry, M. Idrees, T. V. Vu, H. V. Phuc, N. N. Hieu, L. T. Hoa, B. Amin, and C. V. Nguyen, "Interfacial characteristics, schottky contact, and optical performance of a graphene/Ga₂Sse van der waals heterostructure: Strain engineering and electric field tunability," *Phys. Rev. B* **102**, 075414 (2020).
- ²⁴⁹H. Cai, B. Chen, M. Blei, S. L. Y. Chang, K. Wu, H. Zhuang, and S. Tongay, "Abnormal band bowing effects in phase instability crossover region of GaSe_{1-x}Te_x nanomaterials," *Nature Communications* **9**, 1927 (2018).
- ²⁵⁰A. van de Walle and G. Ceder, "Automating first-principles phase diagram calculations," *Journal of Phase Equilibria* **23**, 348 (2002).
- ²⁵¹C. A. Melton, M. Zhu, S. Guo, A. Ambrosetti, F. Pederiva, and L. Mitas, "Spin-orbit interactions in electronic structure quantum monte carlo methods," *Phys. Rev. A* **93**, 042502 (2016).
- ²⁵²C. A. Melton, M. C. Bennett, and L. Mitas, "Quantum Monte Carlo with variable spins," *The Journal of Chemical Physics* **144**, 244113 (2016), https://pubs.aip.org/aip/jcp/article-pdf/doi/10.1063/1.4954726/14715692/244113_1_online.pdf.
- ²⁵³K. W. Plumb, J. P. Clancy, L. J. Sandilands, V. V. Shankar, Y. F. Hu, K. S. Burch, H.-Y. Kee, and Y.-J. Kim, "α-rucl₃: A spin-orbit assisted mott insulator on a honeycomb lattice," *Phys. Rev. B* **90**, 041112 (2014).
- ²⁵⁴S. Sinn, C. H. Kim, B. H. Kim, K. D. Lee, C. J. Won, J. S. Oh, M. Han, Y. J. Chang, N. Hur, H. Sato, B.-G. Park, C. Kim, H.-D. Kim, and T. W. Noh, "Electronic structure of the kitaev material α-rucl₃ probed by photoemission and inverse photoemission spectroscopies," *Scientific Reports* **6**, 39544 (2016).
- ²⁵⁵A. Annaberdiev, S. Mandal, L. Mitas, J. T. Krogel, and P. Ganesh, "The role of electron correlations in the electronic structure of putative chern magnet tbmn6sn6," *npj Quantum Materials* **8**, 50 (2023).
- ²⁵⁶E. Mostaani, N. D. Drummond, and V. I. Fal'ko, "Quantum monte carlo calculation of the binding energy of bilayer graphene," *Phys. Rev. Lett.* **115**, 115501 (2015).
- ²⁵⁷H. Shin, J. Kim, H. Lee, O. Heinonen, A. Benali, and Y. Kwon, "Nature of interlayer binding and stacking of sp-sp² hybridized carbon layers: A quantum monte carlo study," *Journal of Chemical Theory and Computation* **13**, 5639–5646 (2017).
- ²⁵⁸H. Kasai, K. Tolborg, M. Sist, J. Zhang, V. R. Hathwar, M. Ø. Filsø, S. Cenedese, K. Sugimoto, J. Overgaard, E. Nishibori, et al., "X-ray electron density investigation of chemical bonding in van der waals materials," *Nat. Mater.* **17**, 249–252 (2018).
- ²⁵⁹L. Shulenburg, A. D. Baczewski, Z. Zhu, J. Guan, and D. Tománek, "The nature of the interlayer interaction in bulk and few-layer phosphorus," *Nano Letters* **15**, 8170–8175 (2015).
- ²⁶⁰V. Tran, R. Soklaski, Y. Liang, and L. Yang, "Layer-controlled band gap and anisotropic excitons in few-layer black phosphorus," *Phys. Rev. B* **89**, 235319 (2014).
- ²⁶¹J.-H. Choi, P. Cui, H. Lan, and Z. Zhang, "Linear scaling of the exciton binding energy versus the band gap of two-dimensional materials," *Phys. Rev. Lett.* **115**, 066403 (2015).
- ²⁶²L. Li, J. Kim, C. Jin, G. J. Ye, D. Y. Qiu, F. H. Da Jornada, Z. Shi, L. Chen, Z. Zhang, F. Yang, et al., "Direct observation of the layer-dependent electronic structure in phosphorene," *Nat. Nanotech.* **12**, 21–25 (2017).
- ²⁶³J. Ahn, I. Hong, G. Lee, H. Shin, A. Benali, and Y. Kwon, "Metastable metallic phase of a bilayer blue phosphorene induced by interlayer bonding and intralayer charge redistributions," *The Journal of Physical Chemistry Letters* **12**, 10981–10986 (2021).
- ²⁶⁴J. Ahn, I. Hong, Y. Kwon, R. C. Clay, L. Shulenburg, H. Shin, and A. Benali, "Phase stability and interlayer interaction of blue phosphorene," *Phys. Rev. B* **98**, 085429 (2018).
- ²⁶⁵J. Arcudia, R. Kempt, M. E. Cifuentes-Quintal, T. Heine, and G. Merino, "Blue phosphorene bilayer is a two-dimensional metal and an unambiguous classification scheme for buckled hexagonal bilayers," *Phys. Rev. Lett.* **125**, 196401 (2020).
- ²⁶⁶Y. Kadioglu, J. A. Santana, H. D. Özaydin, F. Ersan, O. U. Aktürk, E. Aktürk, and F. A. Reboredo, "Diffusion quantum Monte Carlo and density functional calculations of the structural stability of bilayer arsenene," *The Journal of Chemical Physics* **148**, 214706 (2018), https://pubs.aip.org/aip/jcp/article-pdf/doi/10.1063/1.5026120/15543815/214706_1_online.pdf.
- ²⁶⁷C. Kamal and M. Ezawa, "Arsenene: Two-dimensional buckled and puckered honeycomb arsenic systems," *Phys. Rev. B* **91**, 085423 (2015).
- ²⁶⁸Z. Zhang, J. Xie, D. Yang, Y. Wang, M. Si, and D. Xue, "Manifestation of unexpected semiconducting properties in few-layer orthorhombic arsenene," *Applied Physics Express* **8**, 055201 (2015).
- ²⁶⁹S. Zhang, M. Xie, F. Li, Z. Yan, Y. Li, E. Kan, W. Liu, Z. Chen, and H. Zeng, "Semiconducting group 15 monolayers: A broad range of band gaps and high carrier mobilities," *Angewandte Chemie International Edition* **55**, 1666–1669 (2016), <https://onlinelibrary.wiley.com/doi/pdf/10.1002/anie.201507568>.
- ²⁷⁰H.-S. Tsai, S.-W. Wang, C.-H. Hsiao, C.-W. Chen, H. Ouyang, Y.-L. Chueh, H.-C. Kuo, and J.-H. Liang, "Direct synthesis and practical bandgap estimation of multilayer arsenene nanoribbons," *Chemistry of Materials* **28**, 425–429 (2016).
- ²⁷¹H. Cao, Z. Yu, and P. Lu, "Electronic properties of monolayer and bilayer arsenene under in-plane biaxial strains," *Superlattices and Microstructures* **86**, 501–507 (2015).
- ²⁷²K. Luo, S. Chen, and C. Duan, "Indirect-direct band gap transition of two-dimensional arsenic layered semiconductors—cousins of black phosphorus," *Science China Physics, Mechanics & Astronomy* **58**, 87301 (2015).
- ²⁷³K. Mi, J. Xie, M. S. Si, and C. X. Gao, "Layer-stacking effect on electronic structures of bilayer arsenene," *Europhysics Letters* **117**, 27002 (2017).
- ²⁷⁴D. Kecik, E. Durgun, and S. Ciraci, "Stability of single-layer and multilayer arsenene and their mechanical and electronic properties," *Phys. Rev. B* **94**, 205409 (2016).
- ²⁷⁵K. Krongchon, T. Rakib, S. Pathak, E. Ertekin, H. T. Johnson, and L. K. Wagner, "Registry-dependent potential energy and lattice corrugation of twisted bilayer graphene from quantum monte carlo," *Phys. Rev. B* **108**, 235403 (2023).
- ²⁷⁶J. T. Krogel, S. F. Yuk, P. R. C. Kent, and V. R. Cooper, "Perspectives on van der waals density functionals: The case of tis₂," *The Journal of Physical Chemistry A* **124**, 9867–9876 (2020).
- ²⁷⁷V. R. Cooper, "Van der waals density functional: An appropriate exchange functional," *Phys. Rev. B* **81**, 161104 (2010).
- ²⁷⁸M. S. Whittingham, "Electrical energy storage and intercalation chemistry," *Science* **192**, 1126–1127 (1976), <https://www.science.org/doi/pdf/10.1126/science.192.4244.1126>.
- ²⁷⁹C. H. Chen, W. Fabian, F. C. Brown, K. C. Woo, B. Davies, B. DeLong, and A. H. Thompson, "Angle-resolved photoemission studies of the band structure of tise₂ and tis₂," *Phys. Rev. B* **21**, 615–624 (1980).

- ²⁸⁰J. P. Perdew, A. Ruzsinszky, G. I. Csonka, O. A. Vydrov, G. E. Scuseria, L. A. Constantin, X. Zhou, and K. Burke, "Restoring the density-gradient expansion for exchange in solids and surfaces," *Phys. Rev. Lett.* **100**, 136406 (2008).
- ²⁸¹T. Ichihba, A. L. Dzabak, J. T. Krogel, V. R. Cooper, and F. A. Reboredo, "crl₃ revisited with a many-body ab initio theoretical approach," *Phys. Rev. Mater.* **5**, 064006 (2021).
- ²⁸²M. A. McGuire, H. Dixit, V. R. Cooper, and B. C. Sales, "Coupling of crystal structure and magnetism in the layered, ferromagnetic insulator crl₃," *Chemistry of Materials* **27**, 612–620 (2015).
- ²⁸³J. c. v. Klimeš, D. R. Bowler, and A. Michaelides, "Van der waals density functionals applied to solids," *Phys. Rev. B* **83**, 195131 (2011).
- ²⁸⁴J. Ahn, I. Hong, G. Lee, H. Shin, A. Benali, J. T. Krogel, and Y. Kwon, "Structural stability of graphene-supported pt layers: Diffusion monte carlo and density functional theory calculations," *J. Phys. Chem. C* **127**, 18630–18640 (2023).
- ²⁸⁵A. Abdelhafiz, A. Vitale, P. Buntin, B. deGlee, C. Joiner, A. Robertson, E. M. Vogel, J. Warner, and F. M. Alamgir, "Epitaxial and atomically thin graphene–metal hybrid catalyst films: the dual role of graphene as the support and the chemically-transparent protective cap," *Energy & Environmental Science* **11**, 1610–1616 (2018).
- ²⁸⁶J. I. Choi, A. Abdelhafiz, P. Buntin, A. Vitale, A. W. Robertson, J. Warner, S. S. Jang, and F. M. Alamgir, "Contiguous and atomically thin pt film with supra-bulk behavior through graphene-imposed epitaxy," *Adv. Funct. Mater.* **29**, 1902274 (2019).
- ²⁸⁷A. W. Robertson, G.-D. Lee, S. Lee, P. Buntin, M. Drexler, A. A. Abdelhafiz, E. Yoon, J. H. Warner, and F. M. Alamgir, "Atomic structure and dynamics of epitaxial platinum bilayers on graphene," *ACS nano* **13**, 12162–12170 (2019).
- ²⁸⁸H. Shin, S. Kang, J. Koo, H. Lee, J. Kim, and Y. Kwon, *J. Chem. Phys.* **140**, 114702 (2014).
- ²⁸⁹I. Hong, J. Ahn, H. Shin, H. Bae, H. Lee, A. Benali, and Y. Kwon, "Competition between huckel's rule and jahn–teller distortion in small carbon rings: A quantum monte carlo study," *J. Phys. Chem. A* **124**, 3636–3640 (2020).
- ²⁹⁰J. Ahn, I. Hong, G. Lee, H. Shin, A. Benali, and Y. Kwon, "Energetic stability of free-standing and metal-supported borophenes: Quantum monte carlo and density functional theory calculations," *The Journal of Physical Chemistry C* **124**, 24420–24428 (2020).
- ²⁹¹Y. Tobe, I. Ohki, M. Sonoda, H. Niino, T. Sato, and T. Wakabayashi, "Generation and characterization of highly strained dibenzotetrakisdehydro[12]annulene," *Journal of the American Chemical Society* **125**, 5614–5615 (2003).
- ²⁹²M. M. Haley, *Pure and Applied Chemistry* **80**, 519–532 (2008).
- ²⁹³F. Diederich and M. Kivala, "All-carbon scaffolds by rational design," *Advanced Materials* **22**, 803–812 (2010), <https://onlinelibrary.wiley.com/doi/pdf/10.1002/adma.200902623>.
- ²⁹⁴L. Brewer, "THE COHESIVE ENERGIES OF THE ELEMENTS," LBNL Report LBL-3720 Rev (Lawrence Berkeley National Laboratory, 1977).
- ²⁹⁵A. J. Mannix, X.-F. Zhou, B. Kiraly, J. D. Wood, D. Alducin, B. D. Myers, X. Liu, B. L. Fisher, U. Santiago, J. R. Guest, et al., "Synthesis of borophenes: Anisotropic, two-dimensional boron polymorphs," *Science* **350**, 1513–1516 (2015).
- ²⁹⁶Z. Zhang, A. J. Mannix, Z. Hu, B. Kiraly, N. P. Guisinger, M. C. Hersam, and B. I. Yakobson, "Substrate-induced nanoscale undulations of borophene on silver," *Nano Lett.* **16**, 6622–6627 (2016).
- ²⁹⁷B. Kiraly, X. Liu, L. Wang, Z. Zhang, A. J. Mannix, B. L. Fisher, B. I. Yakobson, M. C. Hersam, and N. P. Guisinger, "Borophene synthesis on au (111)," *ACS nano* **13**, 3816–3822 (2019).
- ²⁹⁸W. Li, L. Kong, C. Chen, J. Gou, S. Sheng, W. Zhang, H. Li, L. Chen, P. Cheng, and K. Wu, "Experimental realization of honeycomb borophene," *Sci. Bull.* **63**, 282–286 (2018).
- ²⁹⁹E. S. Penev, S. Bhowmick, A. Sadrzadeh, and B. I. Yakobson, "Polymorphism of two-dimensional boron," *Nano Lett.* **12**, 2441–2445 (2012).
- ³⁰⁰X. Wu, J. Dai, Y. Zhao, Z. Zhuo, J. Yang, and X. C. Zeng, "Two-dimensional boron monolayer sheets," *ACS nano* **6**, 7443–7453 (2012).
- ³⁰¹C. Kittel and P. McEuen, *Introduction to Solid State Physics*, 8th ed. (Wiley, New York, 2004).
- ³⁰²H. Shin, Y. Luo, A. Benali, and Y. Kwon, *Phys. Rev. B* **100**, 075430 (2019).
- ³⁰³F. R. Bagsican, A. Winchester, S. Ghosh, X. Zhang, L. Ma, M. Wang, H. Murakami, S. Talapatra, R. Vajtai, P. M. Ajayan, J. Kono, M. Tonouchi, and I. Kawayama, "Adsorption energy of oxygen molecules on graphene and two-dimensional tungsten disulfide," *Scientific Reports* **7**, 1774 (2017).
- ³⁰⁴J. Ahn, I. Hong, G. Lee, H. Shin, A. Benali, and Y. Kwon, "Adsorption of a single pt atom on graphene: spin crossing between physisorbed triplet and chemisorbed singlet states," *Phys. Chem. Chem. Phys.* **23**, 22147–22154 (2021).
- ³⁰⁵E. Yoo, T. Okata, T. Akita, M. Kohyama, J. Nakamura, and I. Honma, "Enhanced electrocatalytic activity of pt subnanoclusters on graphene nanosheet surface," *Nano Lett.* **9**, 2255–2259 (2009).
- ³⁰⁶Y. Li, W. Gao, L. Ci, C. Wang, and P. M. Ajayan, "Catalytic performance of pt nanoparticles on reduced graphene oxide for methanol electro-oxidation," *Carbon* **48**, 1124–1130 (2010).
- ³⁰⁷H. Wu, D. Wexler, and H. Liu, "Durability investigation of graphene-supported pt nanocatalysts for pem fuel cells," *Solid State Electrochem.* **15**, 1057–1062 (2011).
- ³⁰⁸S. Sun, G. Zhang, N. Gauquelin, N. Chen, J. Zhou, S. Yang, W. Chen, X. Meng, D. Geng, M. N. Banis, et al., "Single-atom catalysis using pt/graphene achieved through atomic layer deposition," *Sci. Rep.* **3**, 1–9 (2013).
- ³⁰⁹N. Cheng, L. Zhang, K. Doyle-Davis, and X. Sun, "Single-atom catalysts: from design to application," *Electrochemical Energy Reviews* **2**, 539–573 (2019).
- ³¹⁰G. Lee, I. Hong, J. Ahn, H. Shin, A. Benali, and Y. Kwon, "Hydrogen separation with a graphenylene monolayer: Diffusion monte carlo study," *J. Chem. Phys.* **157**, 144703 (2022).
- ³¹¹S. Sahu and G. C. Rout, "Band gap opening in graphene: a short theoretical study," *International Nano Letters* **7**, 81–89 (2017).
- ³¹²H. González-Herrero, J. M. Gómez-Rodríguez, P. Mallet, M. Moaied, J. J. Palacios, C. Salgado, M. M. Ugeda, J.-Y. Veuillen, F. Yndurain, and I. Brihuega, "Atomic-scale control of graphene magnetism by using hydrogen atoms," *Science* **352**, 437–441 (2016), <https://www.science.org/doi/pdf/10.1126/science.aad8038>.
- ³¹³A. I. Ismail and A. A. Mubarak, "Ab initio study of the effect of hydrogen adsorption on the electronic, magnetic and optical behavior of m-graphene (m = o, f) sheet," *International Journal of Modern Physics C* **29**, 1850092 (2018), <https://doi.org/10.1142/S0129183118500924>.
- ³¹⁴O. K. Alekseeva, I. V. Pushkareva, A. S. Pushkarev, and V. N. Fateev, "Graphene and graphene-like materials for hydrogen energy," *Nanotechnologies in Russia* **15**, 273–300 (2020).
- ³¹⁵A. Dumi, S. Upadhyay, L. Bernasconi, H. Shin, A. Benali, and K. D. Jordan, "The binding of atomic hydrogen on graphene from density functional theory and diffusion Monte Carlo calculations," *The Journal of Chemical Physics* **156**, 144702 (2022), https://pubs.aip.org/aip/jcp/article-pdf/doi/10.1063/5.0085982/16540767/144702_1_online.pdf.
- ³¹⁶D. M. Thomas, Y. Asiri, and N. D. Drummond, "Point defect formation energies in graphene from diffusion quantum monte carlo and density functional theory," *Phys. Rev. B* **105**, 184114 (2022).